Experimental and Theoretical Studies of Cloud Condensation Nuclei

Thesis by

Patrick Yung-Shie Chuang

In Partial Fulfillment of the Requirements
for the Degree of
Doctor of Philosophy

California Institute of Technology
Pasadena, California

1999
(Submitted May 17, 1999)

Acknowledgements

The road to graduation is a long one, and it is the people along the way who make the experience special.

I'd like to thank John Seinfeld for his scientific and monetary support of my work, for the advice he provided over the years, and for the trust he showed in me and my project. Rick Flagan was invaluable on the experimental side of my work, for his endless supply of ideas, and for his ready advice. Bob Charlson served in many ways as a third advisor, and our dialogue over the years is greatly appreciated. His enthusiasm for the subject is infectious, and it was his ideas that began the work that became Chapter 4.

I would like to thank the Environmental Engineering Science department for providing a friendly, fun, and stimulating environment. Jim Morgan was particularly helpful, especially for philosophical maintenance during times of need. His insight and willingness to make time to discuss a variety of topics (including, of course, basketball) are very much appreciated.

Graduation would not have been possible without the help of numerous people in the Aerosols/Air Pollution group. Paul taught me the ropes in lab; Donald did likewise on the computers. Greg's design lessons and discussions were essential to the project. Jim's design help and optical experience were equally invaluable. Special thanks to Jim for providing calm, rational solutions during those nights of bleak crisis. Don has been an ideal fieldwork partner and coworker to bounce ideas off of. Thanos provided modelling experience that perfectly complemented my work. Many thanks are also due to Matt, Mike K, Jamie, Mike H, Missy, Hali, Lynn, Cecilia, Jay O, and Tim for useful discussions. Sherwood and Mark Stolzenberg were also great sources of advice.

Uncountable thanks are extended to the incredible staff at Caltech. Fran Matzen, Linda Scott, Elizabeth Hinojos, Shirley Anderson were always friendly and helpful.

as were Rayma Harrison, Susan Leising, and Rich Eastvedt. I can't thank Jennifer Packman, Maria Koeper, and Patti Croke enough for dealing with the inexhaustable demands for purchases needed yesterday, and the mounds of confused paperwork generated by my projects. Russ Green and Rodney Rojas, along with a number of other machinists, provided the experience and practical knowledge that turned ideas into working realities.

Thanks to the Pelican crew, especially Paul Finn, Randy Goken, Haf Jonsson, and Phil Durkee for their help and support. They made being in the field a much more enjoyable and productive experience.

The most treasured part of my tenure at Caltech is the array of friends I made. I thank all of them for shared adventures, experiences, discussions, concern, and advice. Dan is thanked for putting up with me for the entire duration as a roommate and friend, and for electronic music, raves, computer help, and reference books. I'd like to thank: the Abu-Mostafa group (Joe, Zander, Zehra, and Malik) for perpetually entertaining conversation (no topic too trivial!), trips to TLS, and the critically important drinks key; Amy for being a wonderful person to talk to and hang out with; Andria for mutual complaining and support; Anne for (what else?) Ath trips; Courtney for hitting me, attempting to reduce my self-esteem to rubble, haircuts, and being so caring; Don for theories, thought experiments, loud music, and waking me up on time; Don and Courtney together for unmeasurable amounts of pizza, Mexican food, TV, beer, sitting in traffic and just sitting around, and the resulting adventures or, more commonly, non-adventures; Denis for catching bad passes, and his unique brand of humor, especially his impressions of the world around us; Jim for endless conversations about all things big (but no detail too small), and jamming that cam in at an impossible angle, and, with Cathy, for sharing Anna-P with me (and trusting me to babysit!); Matt for Matt-isms, freeway party tricks, beach trips, putting up with everything, changing the subject, and always being up for the next adventure; Mike H for homebrews, bbqs, and his infectious positive vibe; Mike K for teaching me intensity, blocking my layups, being a good rabbit, and action movies; Lisa for great cooking and culinary adventures; to Mike and Lisa together for sharing meals and hanging out; Paul for cleaning up (dishes, beds, errant jumpshots, the lab) and, with Yvette, Red Door trips and providing fantastic food and service, and relaxing shelter; Neil for being a good sport, great roasts, hanging out, and good times; Roberto for tequila, late night drinks, and cool films; and to Jay, for our long journey to friendship, and for lessons and perspectives that I will never forget. Linda is specially thanked for countless lessons learned, unending advice, shared good and bad times, and generally being a great friend. Xubo is also specially thanked for her tremendous friendship and support, and for always being there. I'd like to particularly thank Linda, Dan, and Andria for their support and sharing their own experiences during the most difficult days.

My brother Yen has been a good friend (as well as a ready consumer of all things Mexican), and is thanked for holding down the fort in Edmonton in my absence. The greatest acknowledgement, however, belongs to my parents, who are thanked for being the best parents I can imagine. Of the innumerable ways they have been the best, they are most especially thanked for conducting their lives with intelligence, honor, honesty, respect, caring, and hard work, and thereby being the best teachers of all the important life lessons that one could hope for.

Abstract

Cloud condensation nuclei (CCN), the subset of atmospheric aerosol that nucleate cloud droplet formation, are a key component in cloud formation, and are an important factor in controlling climatically-relevant cloud properties such as cloud albedo, cloud lifetime, and precipitation rate.

A CCN instrument that satisfies the constraints for small aircraft operation – minimum weight, volume, and power consumption, good robustness, and high frequency measurement – was constructed. The measurement technique was based on that of Hudson (1989) because it reportedly offered the ability to make measurements of CCN at all supersaturations simultaneously at high frequency and with good counting statistics. Modelling studies, and laboratory and field measurements, subsequently showed that this technique exhibits poor sensitivity. The CCN instrument was also studied in fixed supersaturation mode, where it is able to accurately measure CCN concentration at a fixed supersaturation, whose value ranges from 0.1 and 2%.

The CCN instrument was flown during the 2nd Aerosol Characterization Experiment (ACE-2). The data were reported at a fixed supersaturation of 0.1%. Intercomparison of these measurements with those on two other aircraft shows good agreement. A sublinear relationship between measured CCN concentration and that predicted from aerosol size distribution and chemical composition measurements, $N_{meas} \sim N_{pred}^{0.72}$. In-situ measurements of below-cloud CCN concentration and cloud droplet number concentration are compared. The results are in agreement with model predictions and with previous studies. Cloud droplet concentration is predicted to depend on the CCN spectrum and updraft velocity.

Cloud droplet activation has often been assumed to be reasonably described by an equilibrium model. The error in calculated cloud droplet number concentration due to the influence of condensational growth kinetics was shown to be significant for some conditions. Such errors are estimated to lead to overestimates of indirect radiative climate forcing on the order of 1 $\mathrm{W\,m^{-2}}$. Accurate interpretation of measured CCN concentration may require consideration of activation kinetics associated with CCN instruments.

Contents

List of Figures

List of Tables

Chapter 1 Introduction

Nature is a mutable cloud which is always and never the same.

Ralph Waldo Emerson

1.1 Motivation

Clouds are an important component of the climate system, generally covering between half to two-thirds of the global surface. Clouds reflect incoming sunlight and absorb outgoing longwave radiation, thereby exerting both cooling and warming influences on the Earth. They are one of the controlling factors in regulating the tropospheric content of water vapor, an important greenhouse gas. They are intimately linked to precipitation, one of the crucial elements in climate forecasting. Precipitation is the major factor in determining cloud lifetime, and in the removal of atmospheric aerosols, and possibly in the creation of new particles in the troposphere. Chemical processes that occur within cloud droplets, such as the production of sulfate from SO_2, contribute significantly to the cycling of atmospheric compounds. Accurately predicting climate change requires an improved understanding of cloud formation and evolution, their influences on climate, and how they will react to global changes in atmospheric composition.

Cloud condensation nuclei (CCN) are defined as the subset of atmospheric aerosol that are able to nucleate cloud droplet formation. The activation of CCN is one of the first steps in cloud formation, and therefore the number concentration of CCN as a function of their cloud droplet nucleating ability is a key parameter in determining not only microscale but also possibly mesoscale cloud features, both of which are climatically relevant. Unfortunately, understanding of cloud microphysical processes is incomplete. In order to predict the influence of human activities on the climate system via global changes in cloud properties, great improvements in our knowledge are required. Experimental data relating to CCN are useful in understanding how anthropogenically-derived aerosols which can serve as CCN may perturb the clouds that they nucleate. Such data can then be used to test hypotheses about the role of CCN in cloud processes and cloud properties and eventually verify the predictive ability of general circulation models (GCMs) which are used for climate forecasting. Theoretical advances in understanding the role of CCN in cloud microphysics also improve and refine the algorithms used in such models, and also guide us towards making measurements of those variables that are most appropriate for climate research.

The effect of clouds on the Earth's radiative balance recently has been a subject of great interest. The ultimate goal of this research is to understand how anthropogenic gas- and particle-phase pollutants alter this radiative balance. The perturbation due to anthropogenic influences is, however, expected to be a small (but still climatically significant) compared to the total cloud forcing. The Intergovernmental Panel on Climate Change (IPCC), in its most recent report (IPCC, 1996), did not estimate the magnitude of the indirect effect of aerosols, defined as the change in cloud radiative forcing resulting from the addition of anthropogenically-derived CCN to the atmosphere, although a range of 0 to -1.5 Wm^{-2} was proposed. In contrast, the greenhouse gas forcing was estimated to be 2.5 Wm^{-2} with an uncertainty of 15%. To isolate the effect of CCN on clouds is challenging because cloud properties are also dependent on a number of other variables.

1.2 Objectives

Unmanned air vehicles (UAVs) offer advantages over traditional aircraft for in-situ sampling of the atmosphere. UAVs possess a number of advantages such as low operating costs, long flight duration, and pilot comfort and safety. However, UAV instrumentation are subject to a number of unique constraints, making many instruments designed for manned aircraft unsuitable for such platforms. Because UAVs tend to be smaller, instruments must be extremely lightweight, compact, and energy efficient. They must also be capable of autonomous operation for flights as long as 24 hours, should automatically restart if interrupted, and must be reliable over the course of many flights. Lastly, measurements should be made in near real time in order to examine the spatial variability within the atmosphere. A measurement taken over 10 minutes for an aircraft flying at 150 km/h is a composite look at a 25 km long leg, which is much larger than the characteristic spatial scales of many interesting phenomena.

Constructing a CCN spectrometer for UAV application therefore required a novel approach. The only instrument (Hudson, 1989) capable of collecting nearly real-time CCN data for a wide range of supersaturations is poorly characterized, extremely heavy (a crane is typically needed for installation), and requires constant operator attention. Traditional CCN instruments acquire data at a single supersaturation at a time, so obtaining a five point CCN spectrum would require on the order of half an hour or more. Such instruments also cannot measure CCN at supersaturations less than 0.1% even though such data are scientifically relevant. We therefore initially began the project with the intent to design and construct a new CCN spectrometer which is intended to measure climatically interesting data while satisfying all the above UAV constraints. In the course of this research, we discovered limitations in our new instrument as well as in other existing CCN instruments. This work is described in Chapter 2.

Participation in the 2nd Aerosol Characterization Experiment (ACE-2) provided an opportunity to take below-cloud CCN measurements while other aircraft simultaneously measure in-cloud and above-cloud properties. The whole dataset therefore permits local closure of CCN concentration (comparison of CCN spectra with that predicted from aerosol size distributions and chemical composition measurements) as well as attempts at understanding the relationship between below-cloud CCN with in-cloud microphysical properties such as cloud droplet concentration and effective diameter. It is important to attempt to relate these parameters in order to understand the possible pertubation of anthropogenic aerosols on clouds on a climatically relevant scale. Few data sets of this scope are available, so there is a real need for more coordinated measurements. Analysis of CCN data and their relationship with other parameters from case studies from the ACE-2 field project CLOUDYCOLUMN flights are presented in Chapter 3.

The classic model of CCN activation is an equilibrium model, and is widely used in GCMs. Chapter 4 describes some theoretical calculations that determine the error in using the equilibrium model as opposed to an explicit kinetic model. It is found that significant biases can occur in realistic atmospheric conditions which can change GCM calculations of climate forcing by amounts comparable to the radiative forcing estimated to be due to anthropogenic greenhouse gas. These results also have potentially important ramifications for CCN measurements. The effect of the presence of organic species as part of the composition of CCN is also investigated since, classically, CCN are thought to be inorganic salts such as sulfates and sodium chloride.

Chapter 2 Design of a CCN Spectrometer for Airborne Measurement

Hamlet: Do you see yonder cloud that's almost in shape of a camel?
Polonius: By the mass, and 'tis like a camel, indeed.
Hamlet: Methinks it is like a weasel.
Polonius: It is backed like a weasel.
Hamlet: Or like a whale?
Polonius: Very like a whale.
W. S. SHAKESPEARE, *Hamlet*

Abstract

A new instrument for measuring cloud condensation nuclei (CCN) onboard small aircraft is described. Small aircraft are attractive mainly because they are less costly, but require instruments that are designed for minimum weight, volume, and power consumption, and that are robust and capable of autonomous operation while also able to make high quality measurements at high frequency. The instrument design combines the streamwise gradient technique previously reported by Hudson (1989), and the alternating gradient condensation nuclei counter described by Hoppel et al. (1979). Field and lab measurements, and modeling studies show that this technique exhibits poor sensitivity for the measurement of CCN spectra; for the climatically important range of critical supersaturations, 0.03 to 1%, the measured variable, droplet diameter, varies by 30%. The ability to resolve CCN spectra using this technique is therefore questionable. Studies of this instrument in a fixed supersaturation mode show that it can measure CCN at a single critical supersaturation in the range of 0.1 to 2%. Calibration and testing of the instrument in this mode is described. The instrument is capable of making accurate, high frequency (> 0.1 Hz) measurements of CCN at a fixed supersaturation, while satisfying the constraints for small aircraft.

2.1 Introduction

Cloud condensation nuclei (CCN), those particles that nucleate cloud droplet formation, influence the droplet number and size distribution in a cloud, which in turn determine the cloud albedo, lifetime, and precipitation rate, with important climate effects. Knowledge of the nature of CCN is essential to understanding possible anthropogenically-induced climate change.

Ideally, a measurement of cloud condensation nuclei would reveal the distribution of particles with respect to the supersaturation at which they activate in the atmosphere. Unfortunately, no laboratory measurement can faithfully reproduce the atmospheric conditions in which cloud droplets form because of the compromises inherent in instrument design. Efforts to measure CCN in the cloud-forming regions of the atmosphere are particularly constrained. An airborne instrument must work within weight, power, and size constraints imposed by the aircraft on which the instrument is to be flown. Moreover, high flight speeds mean that measurements probe substantial distances along the flight path unless the measurement can be completed in a short time.

CCN are measured by exposing the aerosol to supersaturation with water vapor for sufficient time that the droplets activate and begin to grow. The supersaturation is achieved by maintaining wetted surfaces that enclose the aerosol sample at different temperatures. Maintaining the surface wetting is difficult, often requiring operator intervention or limiting the operating time of the instrument.

Most measurements are performed by exposing the aerosol to a fixed supersaturation so that the number concentration that activate at supersaturations equal to or lower than the posed value can be determined. The supersaturation distribution can be determined by a sequence of measurements at different applied supersaturations. The time required to determine a supersaturation distribution is long enough that few steps are employed in most airborne measurements.

Hudson (1989) introduced an indirect approach for rapid measurement of supersaturation distributions. In Hudson's method, the aerosol is exposed to a supersaturation that increases with time as the aerosol flows through the supersaturation apparatus. Particles that activate early, when the supersaturation is low, grow for longer time than do those that must wait until the supersaturation has reached higher values. The supersaturation at which the droplet activated is inferred from the ultimate size achieved at the end of the flow channel. Although this measurement method is less direct than the fixed supersaturation technique, and must be calibrated to account properly for the influence of growth kinetics on the size/critical supersaturation relationship, the possibility of measuring all critical supersaturations simultaneously and in short times makes it attractive for airborne measurements. Hudson (e.g., Hudson and Clarke, 1992; Hudson and Svensson, 1995; Hudson et al., 1998) has used his instrument to measure CCN distributions in a number of measurement campaigns. His instrument is, however, limited to use aboard large aircraft due to its size, weight, and the need for frequent operator intervention.

We seek to measure CCN using smaller, less costly aircraft. Such a strategy imposes serious constraints on the size, weight, and power consumption and requires robust, unattended operation. Chuang et al. (1999) implemented Hudson's (1989) streamwise gradient approach to CCN measurement in a novel tubular CCN design developed by Hoppel et al. (1979) to produce a robust instrument for CCN measurement that was small enough to fly aboard the Center for Interdisciplinary Remotely Piloted Aircraft Studies (CIRPAS) *Pelican*. During ACE-2, this instrument was used during 15 *Pelican* flights flown out of Tenerife in the Canary Islands in June and July, 1997. Although the instrument was designed to provide supersaturation spectra, the data obtained in the field measurements were deemed to exhibit sufficient detail only to report the number concentration of CCN at but one critical supersaturation, 0.1%.

This paper experimentally probes the reasons for the low resolution of the streamwise gradient CCN spectrometer. The suitability of the instrument of Chuang et al. (1999) for measurements at fixed supersaturation is also examined. The latter approach is shown to be preferable given the fundamental limitations of the streamwise gradient method. We begin with a brief review of CCN measurement methods.

2.2 Background

The equilibrium relationship between the diameter of a droplet and the relative humidity of the surrounding air is given by the Köhler equation (Seinfeld and Pandis, 1998):

$$\ln(\frac{p_w}{p^o}) = \frac{4\sigma M_w}{RT\rho_w D_p} - \frac{6n_s M_w}{\pi\rho_w D_p^3} \tag{2.1}$$

where p_w is the vapor pressure of water over a droplet, p^o is the vapor pressure of a flat surface of water, σ is the droplet surface tension, M_w is the molecular weight of water, R is the universal gas constant, T is the droplet temperature, ρ_w is the density of liquid water, n_s is the number moles of solution-phase species, and D_p is the droplet diameter. The Köhler curve exhibits a maximum at a droplet diameter known as the critical diameter, D_{pc}, and at a supersaturation, $S = (p_w/p^o) - 1$, known as the critical supersaturation, S_c. When a droplet grows (by condensation of water vapor in the case of clouds) to a diameter larger than the critical diameter, it is considered to be *activated*, and is able to grow spontaneously to very large sizes, limited only by the kinetics of condensational growth. The activation and subsequent growth of CCN are the first steps in the formation cloud droplets.

A review of existing CCN instruments, all of which have been implemented on aircraft platforms, is first presented. The review focuses on the features of each instrument, especially in regard to their utility for aircraft operation. Nearly all airborne CCN data that are in the literature have been acquired using the instruments to be reviewed, although there exist others for which airborne measurements have been reported (e.g., Leaitch and Megaw, 1982). The purpose of this review is to summarize the features of existing CCN instruments, especially with regard to their ability to make airborne measurements.

2.2.1 Static Thermal Diffusion Cloud Chamber

CCN counters that measure CCN concentration at one supersaturation at a time have existed for decades. The classic static thermal diffusion chamber design consists of two parallel horizontal metal plates whose facing surfaces are wetted (Twomey, 1963). When held at different constant temperatures, a nearly-parabolic supersaturation profile is achieved between the plates. Those particles that are able to activate at the peak supersaturation in the chamber grow to become large droplets, while those that cannot activate achieve only their equilibrium diameter. By measuring the number concentration of droplets, the concentration of CCN that activate at the peak supersaturation is determined without the need for calibration. In practice, this peak supersaturation is somewhat uncertain because the temperature of the water film is not precisely known.

To measure the CCN spectrum in this type of instrument, the density function describing the number concentration of CCN as a function of critical supersaturation, i.e., $dN/d\log S_c$, the temperature difference between the plates must be systematically changed. This typically requires several minutes. The thermal diffusion chamber is, therefore, limited to low temporal resolution, typically fewer than one measurement per minute (Lala and Jiusto, 1977). The minimum critical supersaturation that can be measured is generally greater than 0.2%, not low enough to match supersaturations found in some marine stratus clouds. The highest S_c is typically at least 2%. Predictions of the uncertainty in CCN concentration measurements in the static thermal diffusion cloud chamber have been estimated to be a factor of two at 1% supersaturation, increasing to a factor of 10 at 0.1% supersaturation (Alofs and Carstens, 1976). Radke and Turner (1972) compared simultaneous CCN concentration measurements using four thermal diffusion chambers from different research groups; the instruments agreed to within a factor of 4 at 0.3% supersaturation, and a factor of 1.5 at 0.75%.

Even though these instruments have long been in operation, there are a number of issues in the interpretation of static diffusion CCN counter data that remain unresolved. One common technique for determining the number concentration of activated droplets in static diffusion cloud chambers is through calibrated photometric measurements of the total intensity of light scattered from the ensemble of droplets within an illuminated view volume. Another popular method involves taking photographs or a video recording of an illuminated view volume and counting the number of imaged droplets. Recent research has shown that the photometric method is unreliable in some circumstances (G. C. Roberts, personal communication). Neither the peak light intensity nor integrated signal area can be unambiguously related to droplet number concentration because both measures are also dependent on the droplet size distribution, which is neither known a priori nor measured by the instrument. Counting droplets using photographs or videotapes of the view volume, while labour- and/or computationally-intensive, appears to be more accurate at present.

Another potential data interpretation issue involves the measurement of the temperature of the two plates. The relevant temperatures that determine the supersaturation profile for static diffusion chambers are those of the water films that wet the plates. Typically, however, these instruments measure and control the temperature at a location some distance from the plate surfaces, which could cause the stated supersaturation at which CCN are counted to be overestimated by a significant amount, especially at small temperature differences, i.e., low critical supersaturations.

Detection of sedimenting droplets that were not originally activated in the view volume may also bias CCN measurements. The supersaturation above and below the view volume that is approximately centered between the two plates is lower than that in the view volume, but may be sufficient to activate some particles. Moreover, higher supersaturations may occur before vapor and thermal diffusion reach steady state. Activated droplets can grow sufficiently large to sediment into the view volume in the interval during which the concentration measurement is being made, which could lead to a systematic measurement bias. No quantitative estimate of the magnitude of this bias has been reported in the literature.

On the positive side, static thermal diffusion chambers can be lightweight and robust (Delene et al. 1998). However, issues associated with data interpretation, and the large inherent uncertainties in measurements for supersaturations in the range relevant to marine stratiform clouds, i.e., less than 0.5%, suggest that other measurement techniques should be explored in order to facilitate accurate CCN concentration measurements.

2.2.2 Continuous-Flow Parallel-Plate Diffusion Chambers

A continuous-flow parallel-plate thermal diffusion chamber has a number of potential advantages over static diffusion counters. Because the sample flow is continuous, the time resolution of the instrument is not limited to that of the batch flow cycle as in static thermal diffusion chambers. Furthermore, the instrument operates at steady state so flow transients that complicate data analysis in static chambers are avoided. In the continuous-flow instrument, a particle-free sheath flow can be used to confine the sample to a region close to the supersaturation maximum so that all CCN are exposed to the same supersaturation, thereby increasing the precision of the measurement. However, such instruments are subject to some of the same limitations as static chambers. Due to the time required for droplet growth at low supersaturation, the lowest supersaturation at which the measurement can be made is about 0.1%. When the two plates are horizontal, gravitational sedimentation limits the time during which droplets experience a uniform supersaturation. Thermophoretic and diffusiophoretic forces limit the growth time between vertical plates, although this time limit is as much as eight times that for horizontal plates (Sinnarwalla and Alofs, 1973). Such instruments are also relatively massive, with typical plate sizes of 0.4 x 0.3 x 0.013 m (Hudson and Squires, 1976) and 1.0 x 0.13 m (Sinnarwalla and Alofs, 1973; plate thickness not reported). In order to measure the CCN spectrum, the temperature of the plates must be changed, which, given the large heat capacity of the plates, is both time and energy intensive.

An extension of this design, first published by Fukuta and Saxena (1979), utilizes a gradient in temperature transverse to the flow direction to expose particles along different streamlines (but still flowing in the plane centered between the two plates) to different uniform supersaturations. Although this principle can be used to measure the CCN spectrum in near real-time, it is still limited in supersaturation range and, in its current form, by size and weight (0.84 x 0.23 x 0.0064 m and 26 kg for the chamber alone).

Continuous-flow parallel-plate devices can achieve better time resolution and precision than static thermal diffusion chambers since they are not subject to a batch flow cycle and complex transient supersaturations. Such instruments must be significantly larger than static chambers, however, to minimize end effects. As a result, they tend to be heavier and consume more power than the smaller diffusion cloud chambers.

2.2.3 Isothermal Haze Chambers

Isothermal haze chambers (IHCs), first proposed and built by Laktionov (1972), differ from other CCN instruments in that they do not activate droplets, but rather measure the diameter of particles in equilibrium with a saturated atmosphere (relative humidity of 100%). Köhler theory is then used to deduce the critical supersaturation of the particle from its equilibrium size. In practice, it is difficult to maintain exactly 100% RH, and the measurement is highly sensitive to deviations from 100% RH (Figure 2.1). If the RH is 99.5%, for example, rather than exactly 100%, it can be seen from Figure 2.1 that a systematic overestimation of each particle's critical supersaturation results. This overestimation is about 20% for particles with S_c of 0.2%, increasing to more than a factor of two for particles with S_c of 0.04%. Alternately, this systematic bias can also be interpreted as resulting in an underestimate of the cumulative CCN concentration at a given S_c. For example, the concentration of droplets larger than 0.5 μm in diameter is the concentration of CCN with S_c less than approximately 0.17%; if an IHC actually operates at 99.5% RH, the measured concentration of CCN would be those with S_c less than 0.12%, resulting in an underestimation of the CCN concentration at 0.17%. One solution for this problem would be to calibrate the instrument with CCN of known S_c. If the RH in the instrument is stable over time, then the correct relationship between droplet diameter and S_c could be established at this RH.

One advantage of such an instrument is that measurements of the size distribution of the outlet droplets reveals the entire range of critical supersaturations of the input aerosol simultaneously. Another advantage is that it is able to probe supersaturations lower than those of most other instruments (though subject to increasing uncertainties as supersaturation decreases as described above). IHCs have been operated down to 0.016% S_c (Alofs, 1978). Current IHCs are, however, limited to supersaturations below around 0.25% because the optical particle counters used for droplet sizing cannot detect particles less than 0.16 μm in diameter. That minimum size corresponds to the equilibrium size for a salt particle with $S_c = 0.25\%$. If the measurement range could be extended to smaller particle sizes, the upper limit in critical supersaturation could be increased. Although the instrument itself is fairly compact (e.g., the instrument of Alofs (1978) was 5.5 cm in diameter and 30 cm long), the low sample rate is required to achieve equilibration limits the count rate and may cause poor counting statistics in clean environments.

Perhaps the most important limitation, however, is that IHCs do not, strictly speaking, measure CCN since droplets are not activated. In theory, this is not a problem if the particles are composed of completely soluble, surface-inactive compounds since the particle S_c can be uniquely derived from its equilibrium size at 100% RH. However, the results become ambiguous if slightly soluble compounds or surfactants are present in the particles. Such substances can change droplet diameter at 100% RH but not cause changes in S_c (Alofs, 1978; Shulman et al., 1996). Such issues are likely to be more important in cases where substantial amounts of organics are present.

IHCs are attractive primarily because of their small size, their ability to probe a range of supersaturations simultaneously, and their ability to measure CCN with very low critical supersaturations. The main drawbacks are potentially large uncertainties in the relationship between droplet diameter and critical supersaturation, and the fact that they do not measure activated CCN. Whether or not these drawbacks do cause measurement problems remains an open question.

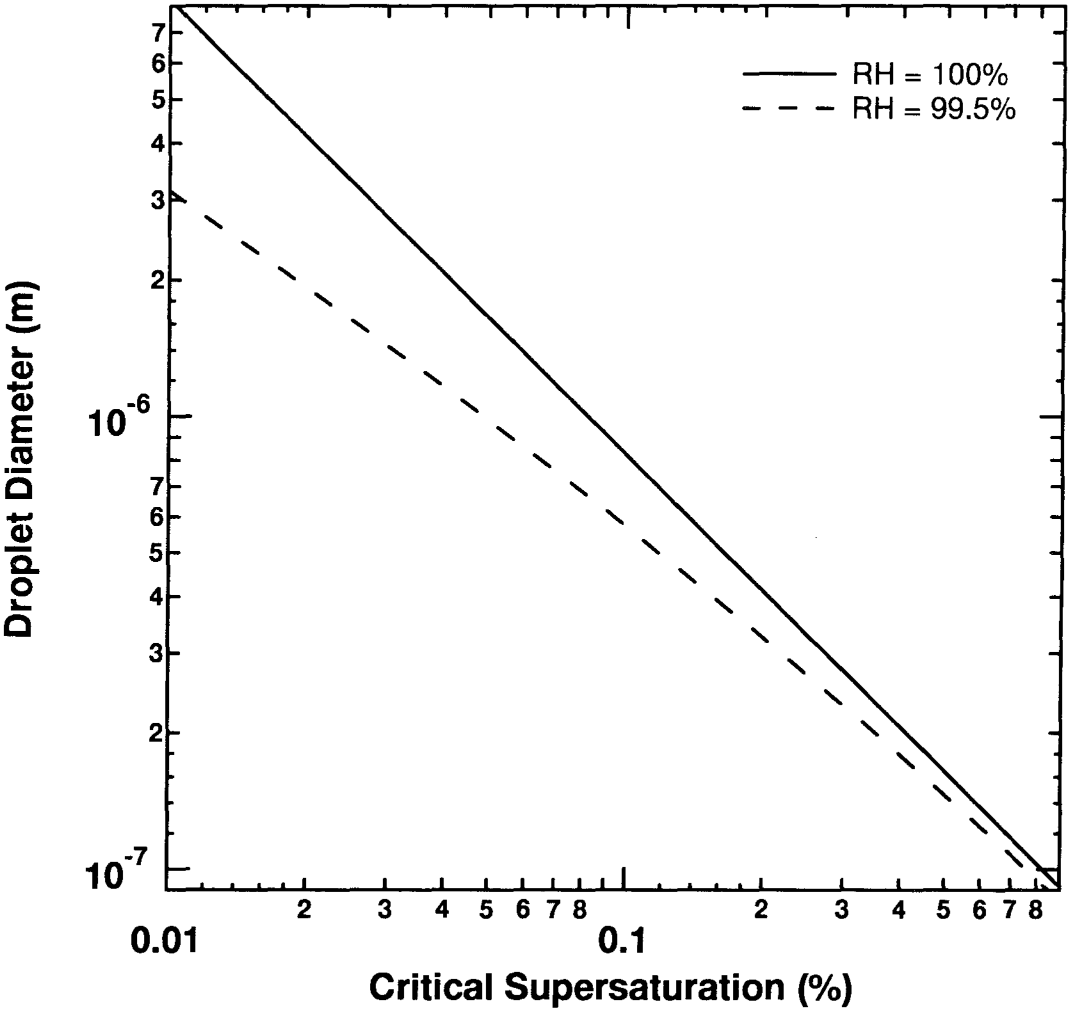

Figure 2.1: Equilibrium diameter of droplets at 100% and 99.5% relative humidity as a function of particle critical supersaturation.

2.2.4 Streamwise Gradient CCN Spectrometer

Hudson (1989) modified a continuous-flow thermal diffusion chamber so that the supersaturation that particles experience increases with time as they flow through the instrument. Particles that activate at low supersaturations near the entrance to the instrument have more time to grow than do those that activate at higher supersaturations (closer to the outlet of the instrument). The CCN spectrum is inferred from measurements of the size distribution of the droplets at the instrument outlet. Since this method measures the end result of particle growth in a time-varying environment, it must be calibrated to relate outlet droplet diameter to inlet S_c. The range of measurable critical supersaturations is reported to be much larger than that for other thermal diffusion chambers, about 0.01 to 1%, covering much of the range of interest for climatically important warm clouds. The size of Hudson's chamber is comparable to previous continuous-flow thermal diffusion instruments. As in the isothermal haze chamber measurements, the S_c distribution can be obtained simultaneously for all S_c, a desirable feature for aircraft studies.

Inversion of the raw data from the streamwise gradient CCN spectrometer to produce a CCN spectrum is non-trivial. Even particles with identical critical supersaturations produce a distribution of optical signals, so an inversion routine that accounts for this distribution of responses is needed to infer the CCN spectrum from the optically measured size distribution. This inversion problem is analogous to that encountered in the interpretation of differential mobility analyzer data, and can be described by the integral equation

$$\int_a^b K_i(S_c)N(S_c)dS_c + \varepsilon_i = y_i, \qquad i = 1 \text{ to } m \tag{2.2}$$

which can be approximated by

$$\sum_{j=1}^{n} K_i(S_{c,j})N(S_{c,j}) + \varepsilon_i = y_i, \qquad i = 1 \text{ to } m \tag{2.3}$$

where K_i is the instrument kernel function, N is the critical supersaturation distribution (the desired quantity), y_i is the measured variable (in this case, measured light scattering intensity), ε_i is the error associated with each measurement y_i, m is the number of measurement channels (in this case, the number of different light intensities measured), and n is the number of discrete values into which the S_c interval $[a, b]$ is divided. For this instrument, the kernel function describes the measured distribution of outlet signals for a sample containing particles of only one S_c and this function is determined experimentally through calibration. Solving equation (2.2) is an ill-posed problem for which an infinite number of solutions is possible (e.g., Kandlikar and Ramachandran, 1999). Smoothing requirements are typically imposed to constrain the solution. If, instead of solving equation (2.2), each output signal is assumed to correspond uniquely and exactly to one inlet S_c, the inferred CCN spectrum is systematically smoothed because features in the inlet spectrum are broadened and flattened due to the instrument transfer function. If the resulting CCN spectra are then parameterized using $N = CS^k$, as is commonly done, then the values of k will be systematically underpredicted.

The streamwise gradient CCN spectrometer has a number of attractive features. It is reportedly able to measure CCN with a wide range of critical supersaturations simultaneously. Moreover, in contrast to IHCs, these droplets are activated. For these reasons, the instrument developed for use aboard the Pelican (with a total instrument payload of 150 kg) was based on the streamwise gradient concept. However, the size and weight of Hudson's instrument are prohibitive for small aircraft, and therefore a totally different physical implemntation was selected. The accuracy of the inversion of droplet size distributions to produce CCN spectra has not been adequately addressed in the literature. This key question will be addressed below.

2.3 Instrument Design

The instrument described here is an adaptation of the streamwise gradient CCN spectrometer described by Hudson (1989), but with a redesigned physical implementation. The goal was to build a robust and automated instrument with minimum mass, volume, and power consumption that is suitable for unattended operation on small aircraft, and that makes high quality measurements at high frequency simultaneously for a wide range of supersaturations. The performance of this new design in the original, streamwise gradient spectrometer mode raise important questions about previous implementations of this method.

2.3.1 CCN Column

The CCN column is the part of the spectrometer that establishes the supersaturation profile that allows the aerosol to activate and grow to large (> 1 μm) size. The column is based on a condensation nuclei (CN) counter design of Hoppel et al. (1979) that employed a wet-wall tubular column that is divided into alternating hot and cold segments to generate a supersaturation profile. To achieve the small supersaturations required for CCN measurements, the present instrument uses much smaller temperature differences (less than 12 K) than the Hoppel et al. instrument. By saturating the air stream at the hot temperature, and then exposing it to the cold temperature, a supersaturation is generated. The supersaturation is maximum on centerline. The temperatures of the successive segments and gas flowrate can be adjusted to generate a monotonically increasing supersaturation profile, although non-monotonic profiles can also be used.

The instrument is illustrated in Figure 2.2. A thin-walled stainless steel tube (19.0 mm OD x 0.25 mm wall thickness) serves as the droplet growth section. Alternating sections of "hot" and "cold" aluminum segments are slip fit over top of this tube. Each of the segments is 28 mm tall, 25 mm square in width, and separated from adjacent sections by a 6.4 mm thick insulation layer. To maximize thermal conduction between these segments and the tube, thermal compound (Wakefield 120-8) is used. Hot sections are heated using resistance heaters and the cold sections are cooled with thermoelectric coolers. To maximize the efficiency of the coolers, a fan at the bottom of the column blows air through a duct enclosing heat sinks attached to the cold sections. A shimstock duct constrains this air flow. All sides of the column segments, except for the heat sinks, are insulated to minimize losses. Each segment has a 20 kΩ thermistor embedded in it to measure the segment temperature. The interior of the stainless tube is lined with wetted filter paper.

The aerosol sample is introduced into the column along its centerline, and is surrounded by a particle-free sheath flow that constrains the sample flow. The inlet assembly also provides a path for water to flow to the top of the column to wet the filter paper. The column outlet is a 9.5 mm diameter thin walled tube that tapers down to a nozzle 1 mm in diameter. The focused droplets are then optically detected as described below. In this way, measurement of the droplet outlet diameter occurs as close to the column exit as possible, minimizing the possibility of any changes in droplet size.

2.3.2 Optical Particle Counter

To minimize instrument weight and to measure particle diameter accurately, a new optical particle counter (OPC) was designed specifically for measuring water droplets in the size range 1 to 20 μm (Figure 2.3). The output from a robust laser diode module coupled to a fiber optic cable (Blue Sky FBC011-00) is expanded to produce a beam that is approximately 4 mm wide and 0.5 mm high. This output beam cross section was chosen to minimize the probability of two droplets passing through the beam simultaneously, while maximizing the uniformity of the intensity seen by particles passing through slightly different parts of the beam. The sample flow is accelerated through a nozzle (half angle 15°, output diameter 1 mm) and passes through the beam 1 mm after leaving the nozzle. Ideally, the nozzle tip is as small as possible so that the droplets all pass through the same part of the laser, but it was found that tip diameters significantly smaller than 1 mm resulted in droplet impaction. The scattered light is collected at an axis 45° off forward and over a solid angle of 0.48 sr (a cone subtended by 45° total angle) using an aspheric lens. This light is then refocused using an identical aspheric lens onto a fiber optic (1 mm core) that transmits the scattered light to a photomultiplier tube that converts the light

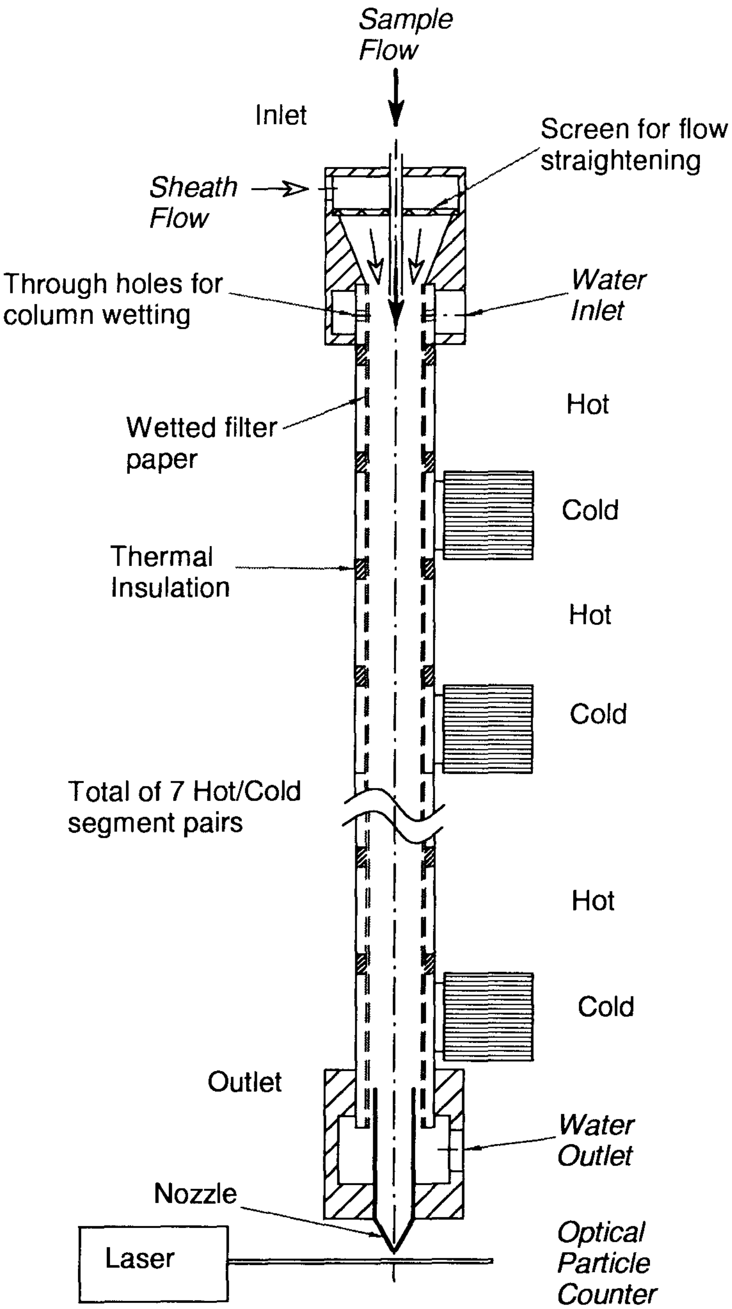

Figure 2.2: Schematic of wet-walled column for CCN instrument.

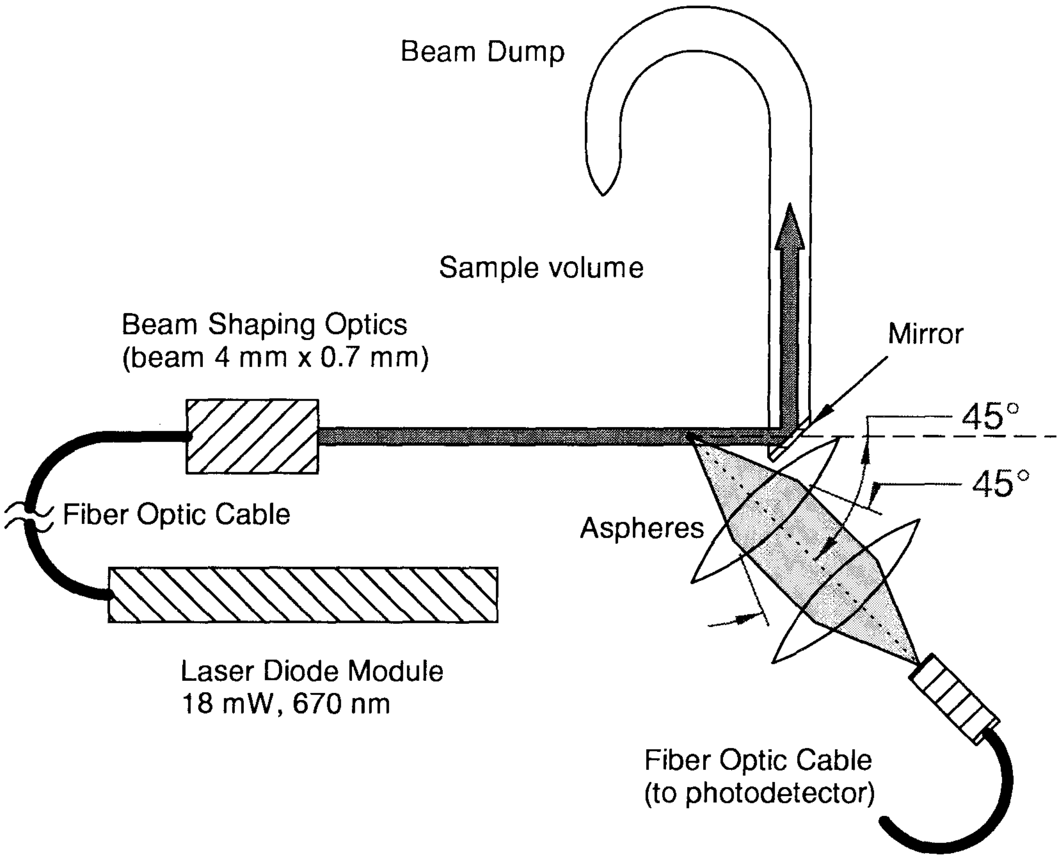

Figure 2.3: Optical particle counter schematic.

intensity to a voltage signal. An avalanche photodiode detector (Hamamatsu C5460-01) has also been used for the same purpose with success. A multichannel analyzer (EG&G Ortec Trump-2k) card measures the peak height of each the voltage pulse generated as droplets pass through the laser beam, and bins that peak height into one of 2048 linearly-spaced bins between 0 and 10 V, i.e., in roughly 5 mV wide bins. As can be seen from Figure 2.3, the collection optics intersect the main beam. To solve this problem, a mirror was mounted onto the bottom of a tube, allowing the unwanted main beam to reflect down the axis of the circularly-bent black tube and thereby be attenuated.

Using a Mie-scattering code (FORTRAN program bhmie.for from Bohren and Huffman, 1983), an OPC with this configuration was simulated. The theoretically-predicted response of the OPC for water (n = 1.33) and diethyl sebacate (DES, n = 1.436) droplets is shown in Figure 2.4. Also shown are experimental calibration data obtained using DES droplets generated from a Berglund-Liu vibrating orifice aerosol generator (Berglund and Liu, 1973). The agreement between theory and experiment is good. The OPC design was chosen such that its response for water droplets is monotonic and does not exhibit any ambiguities due to Mie resonances which are, for example, present for the DES curve between 1.5 and 2 μm.

2.3.3 Flow Scheme

A flow diagram of the instrument is presented in Figure 2.5. The total flow is controlled with a critical orifice, and the sheath flowrate is controlled with a mass flow controller (Sierra Instruments 840). The aerosol flow is then the difference between the total and sheath flows, and is monitored by measuring the pressure drop across a laminar flow tube. The instrument is operated at ambient pressure. The diffusivities of heat and water vapor in air are pressure dependent; this dependence must be considered in the data analysis. Also, since the mass flowrate of the sheath gas is controlled, the sheath volumetric flowrate increases with decreasing pressure. These variations are accounted for in the data analysis.

The column is wetted before each flight. Because almost all of the water loss in the column is due to evaporation to the gas phase and not to condensed water in the aerosol phase, the sheath flow is humidified to an RH of about 97%. We have found that column performance remains constant for periods over 6 hours without further wetting. A peristaltic pump connected to a water reservoir is used to periodically wet the column as necessary.

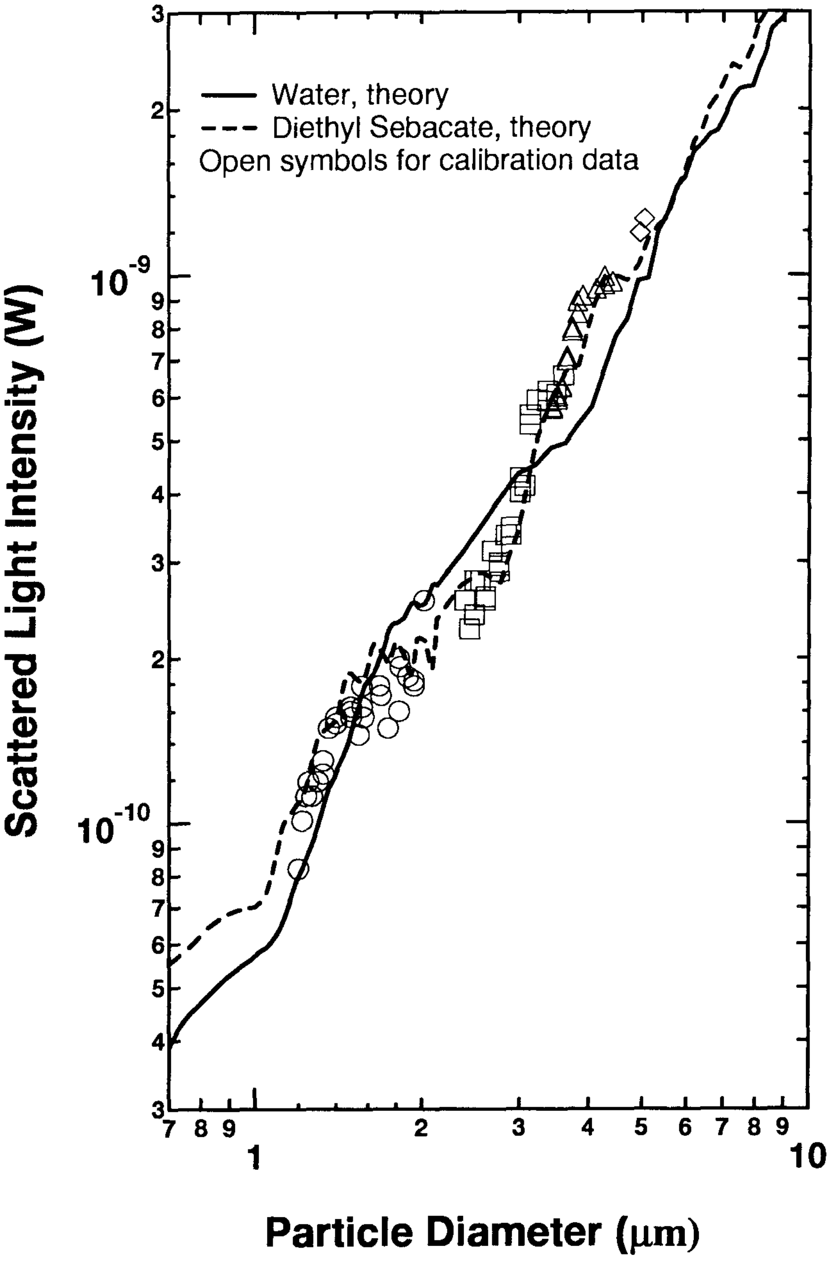

Figure 2.4: Comparison of theoretical and measured OPC response. The open symbols are experimental data for diethyl sebacate (DES) droplets.

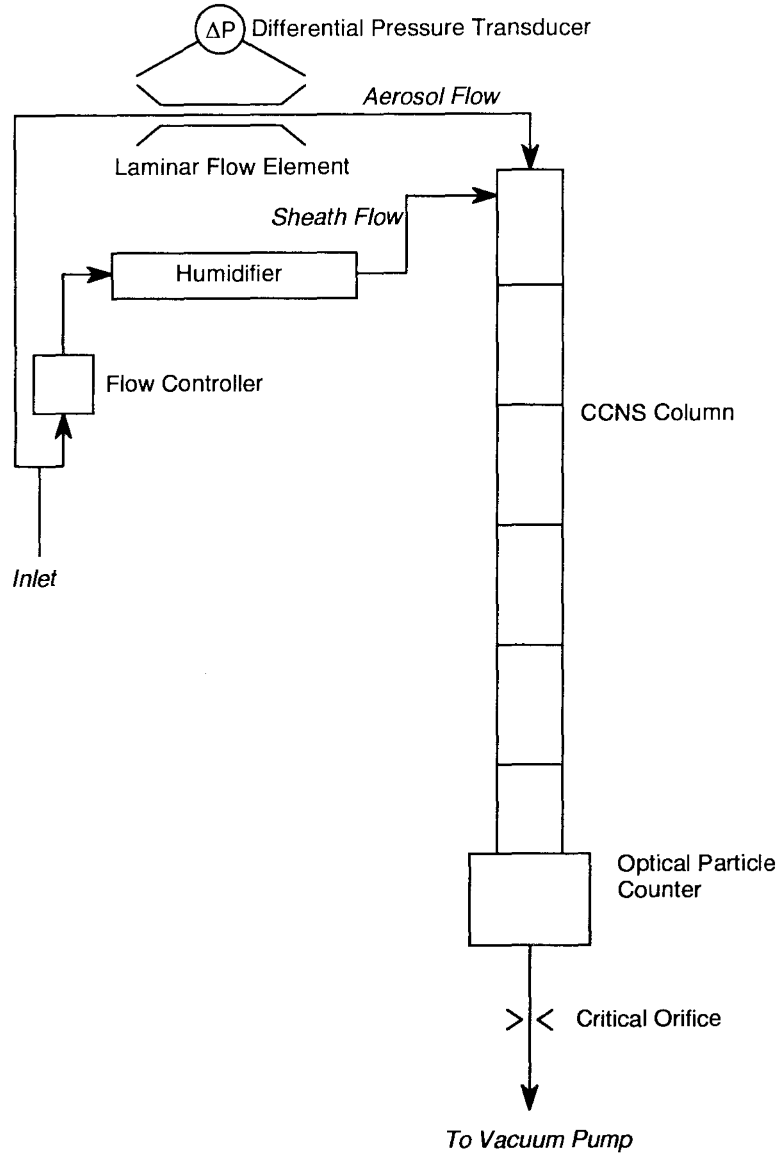

Figure 2.5: CCN instrument flow schematic.

2.3.4 Instrument Electronics

Temperature control of each segment of the column is achieved using a small, lightweight analog proportional-integral (PI) controller (Wavelength Electronics RHM-4000). Acquisition of the temperature, flowrate, and pressure data is done using a data acquisition card (National Instruments AT-MIO-64E). The multichannel analyzer (MCA) card and the data acquisition board are both run using a PC/104 half-sized computer (Advantech 386SX-33) with 16 MB of flash memory using the MS-DOS operating system. The data acquisition and control software was developed using the National Instruments LabWindows application. Instrument status data (column segment temperatures and aerosol and sheath flowrates) are acquired and sent to the aircraft onboard computer once per second. Approximately once per minute, the status data stream is interrupted, and the data acquired by the MCA over the past 60 seconds are read by this program and sent to the aircraft computer, and the MCA board is re-initialized and acquisition of a new spectrum starts.

2.4 Instrument Performance

A model has been developed to simulate the performance of a variety of CCN instruments, including that described in the present work, in order to aid in understanding the effects of changes in instrument operating parameters, such as the temperature ramp.

2.4.1 CCN Instrument Model

The gas phase is treated as a continuum, so differential momentum, mass and heat balances are written for a fixed Eulerian grid. A Lagrangian approach is used for describing the evolution of aerosol particles; each particle is tracked as it grows inside the CCN instrument. The model assumes that:

1. The flow is at steady state and 2-D axisymmetric

2. Each particle follows a single streamline at the streamline velocity
3. Sedimentation, coagulation, and Brownian diffusion are neglected
4. Walls act as a perfect sink/source of water vapor

Governing Equations

With these assumptions, the following system of equations is solved. The continuity equation for the gas phase:

$$\frac{\partial}{\partial z}(r\rho u) + \frac{\partial}{\partial r}(r\rho v) = 0 \tag{2.4}$$

The momentum equation in the radial direction for the gas phase:

$$\frac{\partial}{\partial z}(r\rho uv)+\frac{\partial}{\partial r}(r\rho vv)-\frac{\partial}{\partial z}\left(r\mu\frac{\partial v}{\partial z}\right)-\frac{\partial}{\partial r}\left(r\mu\frac{\partial v}{\partial r}\right) = -r\frac{\partial p}{\partial r}+r\frac{\partial}{\partial z}\left(\mu\frac{\partial u}{\partial r}\right)+\frac{\partial}{\partial r}\left(r\mu\frac{\partial v}{\partial r}\right)-\frac{\mu v}{r} \tag{2.5}$$

The momentum equation in the axial direction for the gas phase:

$$\frac{\partial}{\partial z}(r\rho uu)+\frac{\partial}{\partial r}(r\rho vu)-\frac{\partial}{\partial z}\left(r\mu\frac{\partial u}{\partial z}\right)-\frac{\partial}{\partial r}\left(r\mu\frac{\partial u}{\partial r}\right) = -r\frac{\partial p}{\partial z}+r\frac{\partial}{\partial z}\left(\mu\frac{\partial u}{\partial z}\right)+\frac{\partial}{\partial r}\left(r\mu\frac{\partial v}{\partial z}\right)+\Phi_b \tag{2.6}$$

where r and z are the radial and axial coordinates, u and v are the axial and radial components of velocity, p is the pressure, μ is the viscosity, and ρ is the density. The last term on the RHS of equation (2.6) represents a momentum source due to thermal buoyancy, which for ideal gases is

$$\Phi_{buoyancy} = -\rho g\left(\frac{T - T_{bulk}(z)}{T_{bulk}(z)}\right) \tag{2.7}$$

where $T_{bulk}(z)$ is the radially-averaged temperature at axial position z. Although buoyancy is not expected to be a significant momentum source, it is included for completeness.

The gas phase energy equation is

$$\frac{\partial}{\partial z}(\rho u T) + \frac{\partial}{\partial r}(\rho v T) - \frac{k_a}{c_p}\frac{\partial^2 T}{\partial z^2} - \frac{k_a}{c_p}\frac{1}{r}\frac{\partial}{\partial r}\left(r\frac{\partial T}{\partial r}\right) = \frac{\Delta H_{vap}}{c_p}\Phi_{cond} \tag{2.8}$$

where k_a is the thermal conductivity of air, c_p is the heat capacity, ΔH_{vap} is the enthalpy of vaporization of water. Φ_{cond} is the rate of condensation of liquid water on the aerosol particles, and is calculated from the droplet growth equation (2.10) below.

Conservation of water vapor is described by

$$\frac{\partial}{\partial z}(uC) + \frac{\partial}{\partial r}(vC) - D_v\frac{\partial^2 C}{\partial z^2} - D_v\frac{1}{r}\frac{\partial}{\partial r}\left(r\frac{\partial C}{\partial r}\right) = \Phi_{cond} \tag{2.9}$$

A Lagrangian reference frame is used for simulating the particles as they flow through the CCN instrument. The rate of change of droplet size for each of the particles is calculated from the diffusional growth equation using (Seinfeld and Pandis, 1998)

$$\frac{dD_{pi}}{dt} = \frac{1}{D_{pi}} \cdot \frac{S_v - S_v^{eq}}{\frac{\rho_w RT}{4p^o(T)D_v^{'}M_w} + \frac{\Delta H_{vap}\rho_w}{4k_a^{'}T}\left(\frac{\Delta H_{vap}M_w}{RT} - 1\right)} \tag{2.10}$$

where $p^o(T)$ is the saturation vapor pressure at temperature T, S_v is the local saturation ratio, S_v^{eq} is the equilibrium saturation ratio of the droplet, and R is the universal gas constant. $D_v^{'}$ is the diffusivity of water vapor in air modified for non-continuum effects

$$D_v^{'} = \frac{D_v}{1 + \frac{2D_v}{a_c D_p}\left(\frac{2\pi M_w}{RT}\right)^{1/2}} \tag{2.11}$$

where a_c is the mass accommodation coefficient. $k_a^{'}$ is the thermal conductivity of air modified for non-continuum effects

$$k_a^{'} = \frac{k_a}{1 + \frac{2k_a}{a_T D_p \rho c_p}\left(\frac{2\pi M_a}{RT}\right)^{1/2}} \tag{2.12}$$

where M_a is the mean molar mass of air, a_T is the thermal accommodation coefficient. The equilibrium saturation ratio of the droplet S_v^{eq} is given by the Köhler equation, equation (2.1), where $S_v^{eq} = p_w/p^o$.

Boundary and Initial Conditions

For velocity distribution, two types of initial conditions are considered, either fully developed (i.e., parabolic) or plug flow. Near the wall, a no-slip boundary condition is assumed, $u = v = 0$ and for the outlet, $\partial u/\partial z = 0$ and $v = 0$. Finally, at the symmetry axis, $\partial u/\partial r = \partial v/\partial r = 0$.

For temperature, the inlet conditions are prescribed. At the wall, a constant temperature boundary condition is posed for the each temperature-controlled segment, while a no heat-flux condition is posed for the insulation sections separating the temperature-controlled sections. At the outlet, $\partial T/\partial z = 0$, while at the symmetry axis, $\partial T/\partial r = 0$.

For water vapor concentration, the inlet conditions are prescribed based on the inlet relative humidity. At the wall, the air is assumed to be at saturation at the wall temperature. For the outlet, $\partial C/\partial z = 0$, while at the symmetry axis, $\partial C/\partial r = 0$.

Numerical Solution of Mathematical Model

The model equations cannot be solved analytically, so a numerical solution is obtained by the finite volume method using an upwind differencing scheme (Patankar, 1980). A staggered grid is employed in the calculations such that each velocity grid node lies between two scalar volumes. This procedure ensures that the numerical solution is consistent with respect to pressure. The SIMPLE iterative solution method is used to solve the hydrodynamical cycle of the finite volume equations, while the particle growth equations are solved using the LSODE solver of Hindmarsh (1983). The computer code used for the numerical simulations was based on a modified version of the TEACH-2E code (Gosman and Ideriah, 1976). Finally, the numerical solution was obtained using 100 cells for each of the z- and r- directions.

2.4.2 Streamwise Gradient Operation

The measured outlet droplet diameter is shown in Figure 2.6 as a function of critical supersaturation for an ammonium sulfate aerosol. The measured droplet diameter exceeds the critical diameter for $S_c \gtrsim 0.02\%$. For lower critical supersaturations, the droplet diameter remains smaller than the critical diameter, indicating that the residence time in the column is insufficient to reach the very large critical diameters. Model predictions are also shown in Figure 2.6. Model 1, corresponding to the measured hot and cold segment temperatures, significantly overpredicts the final droplet size. This is not surprising since the model assumes that each wall segment is isothermal at the temperature measured in the aluminum blocks. The temperature difference between the block and the stainless steel tube, and between the tube and the inside water surface, are not taken into account. Unfortunately, they also cannot be measured without perturbing the flows and heat transport. The axial distributions of temperatures along the length of the segments have also been neglected. To compensate for this limitation, calculations were also performed for less severe wall temperatures as shown in Figure 2.7. The experimental data agree well with Model 4 for high S_c, but for lower S_c, the agreement is better for Model 3. The centerline supersaturation profile corresponding to Model 1 is also shown in Figure 2.7.

The most notable feature in the growth data shown in Figure 2.6 is that, over the large range in S_c shown (0.003 to 1%), the outlet droplet diameter changes by at most a factor of two (Model 4). Extremely precise measurements of outlet diameter would be required to resolve particles with substantial differences in S_c, particularly in the climatically important S_c range of 0.03 to 1% where a factor of 30 difference in S_c must be resolved through measurements of a change in diameter of about 30%. The small difference of final droplet size is the result of rapid growth immediately following activation that quickly decelerates as the particles grow, causing newly activated particles to “catch up” with those activated much earlier. Since the rate of condensational growth, dD_p/dt, is inversely proportional to diameter D_p, particles that start off smaller grow more quickly than larger ones, which causes droplets to

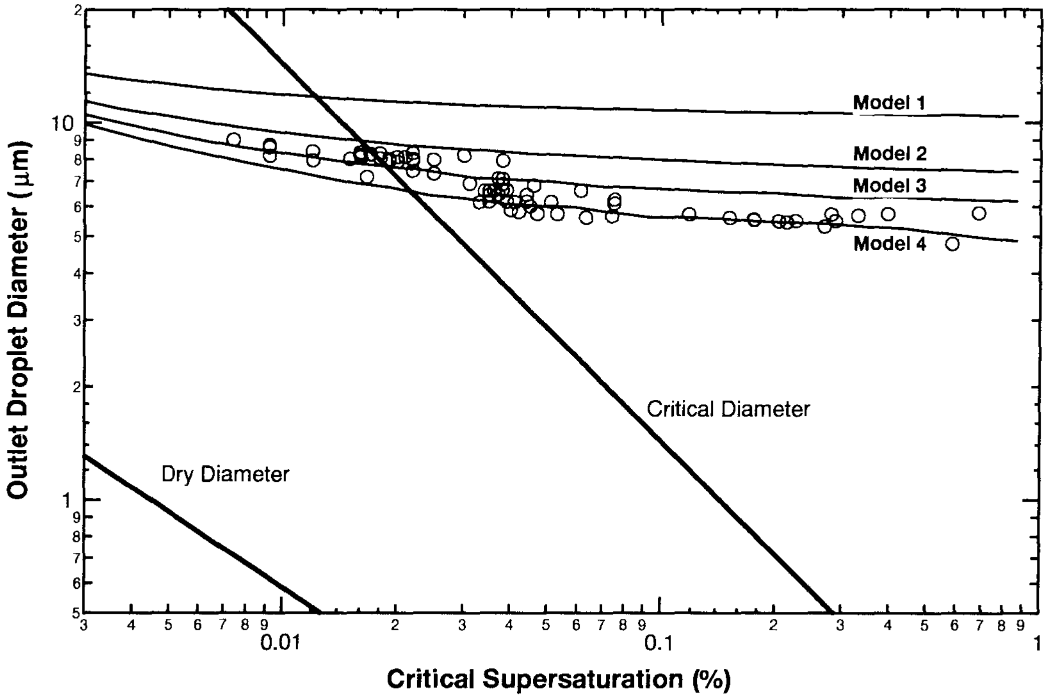

Figure 2.6: Model predictions and experimental data relating droplet diameter at the outlet of the CCN column as a function of critical supersaturation for the CCN instrument in streamwise gradient mode. Models 1 through 4 use different temperature ramps (Figure 7). Also shown is the critical diameter (droplets larger than the critical diameter are activated), and the aerosol dry diameter (chemical composition assumed to be pure ammonium sulphate), as a function of critical supersaturation. Open circles are measured calibration data.

converge to similar sizes.

Despite the great attention devoted to maximizing the potential of the current instrument, particularly the OPC, the inherent lack of sensitivity in the diameter measurement to S_c precludes accurate inversion of the size distribution to produce S_c distributions. However, the instrument can still be effectively used as a single supersaturation counter, as discussed below.

2.4.3 Airborne CCN Measurements

The streamwise gradient instrument was flown onboard the CIRPAS *Pelican* during the 2^{nd} Aerosol Characterization Experiment (ACE-2; Raes et al., 1999) during June

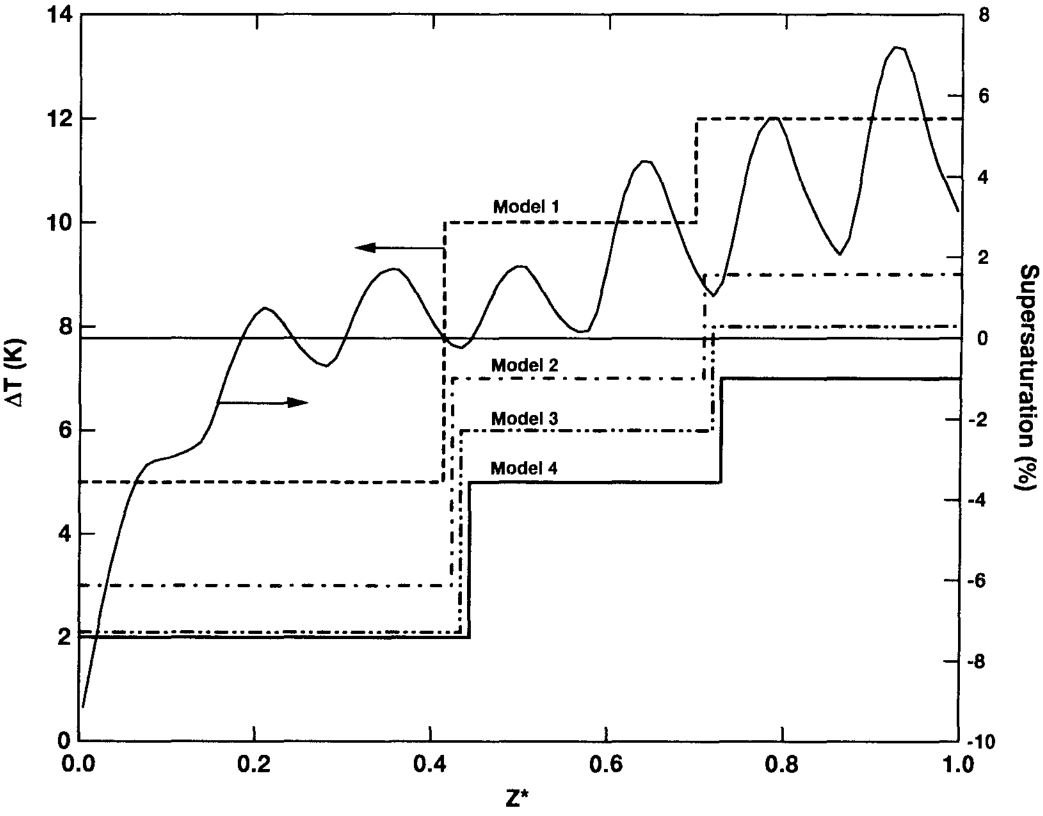

Figure 2.7: Temperature difference profiles (left axis) assumed for simulation runs Model 1 through 4, and supersaturation profile (right axis) on centerline for Model 1 assuming inlet RH of 90%, as a function of nondimensionalized distance along the tube z^*, where $z = 0$ and $z = 1$ are the inlet and outlet, respectively. All hot temperature segments were held at 295 K, and the cold segment temperatures were changed to impose the temperature differences shown. Some of the temperature profiles are offset slightly from each other for presentation clarity; the true profiles change temperature at identical z^*.

and July 1997. The results are reported by Chuang et al. (1999). At the time, it was expected that CCN spectra would be measured using this instrument. Subsequent processing of the data showed that the data could not be inverted reliably to produce spectra, in large part because of the reasons discussed above. It was, however, determined that CCN concentration at 0.1% supersaturation could be measured with a high degree of confidence. The instrument exhibited stable operation for 15 flights with an average duration of 5 h, and a maximum duration of 10 h. Intercomparison of the CCN measurements with CCN instruments onboard two other aircraft (Meteo-France *Merlin*-IV and the MRF C-130) showed good agreement. Overall, the ratio of *Pelican* to *Merlin* CCN concentrations was 1.15 ± 0.15 ($1\ \sigma$), which represents over 360 min of *Pelican* data. The MRF C-130 and *Pelican* were in close proximity for a 15 min period on July 14, during which the present and MRF instruments measured CCN concentrations of 57 cm^{-3} and 47 cm^{-3}, respectively. Comparisons of CCN concentration measured with the current instrument directly below marine stratiform clouds with in-cloud properties (cloud droplet number concentration and effective diameter) as measured by the *Merlin* are also in reasonable agreement with previous studies.

During ACE-2, a number of discoveries relating to the CCN instrument were made. Experiences obtained from the field missions serve as the basis for improvements to the current instrument. For example, during ACE-2 water was introduced to the top of the column using a peristaltic pump that forced water to circulate through the column at a constant low flowrate (< 0.5 mL/min). Excess water at the bottom of the column was returned to the water reservoir located below the level of the column. However, it was found that small changes in the water flowrate changed the output diameter substantially, apparently because the flowing water changes the temperature profile along the wet walls and therefore changes the supersaturation profile within the instrument. The revised scheme is to wet the column initially, allow the column to come to steady state, and make measurements with no forced water flow, as described above.

2.5 Studies of Fixed Supersaturation Operation

Because of the inherent limitations of the streamwise gradient technique, we have examined the performance of the instrument as a single supersaturation device. For this mode, the temperature differences between successive segments were held constant. This configuration imposes a supersaturation profile that reaches a constant centerline value. In this mode of operation, the instrument operates as a traditional CCN counter in that particles below a fixed critical supersaturation activate and subsequently grow to sufficiently large enough sizes that they are distinct from particles that remain unactivated. Instrument performance in this mode has been studied both experimentally and theoretically.

2.5.1 Simulations of Single Supersaturation Instrument

The instrument has been modelled for various temperature differences and pressures. Figure 2.8 shows the effect of changing the temperature difference ΔT. For all curves, the temperature of the cold segments is held at 290 K, while the hot temperature segments are adjusted to reach the specified ΔT. When the temperature difference exceeds 2.5 K, the predicted outlet droplet diameter decreases sharply for particles with S_c larger than some threshold value. As a result, measurements of the concentration of particles whose size exceeds some threshold size (defined by the lower detection limit of the OPC, estimated to be 1 μm for the present instrument) provides a good estimate of the concentration of CCN below the corresponding critical supersaturation. As the temperature difference is increased, so does the threshold S_c, and the distinction between activated and unactivated particles sharpens.

Figure 2.9 shows the predicted outlet droplet size distribution as a function of instrument pressure. Dropping the pressure from 1000 mb initially causes an increase in the growth of droplets because the diffusivities of water and heat increase with decreasing pressure, causing the steady state supersaturation in the instrument to increase. As the pressure decreases further, however, heat and water vapor diffuse so rapidly that each segment more closely approaches equilibrium, lowering the effective supersaturation. As a result, the driving force for condensational growth and the outlet droplet sizes decrease.

The influence of the inlet RH and total particle concentration was also investigated. Even if the flow to the instrument is completely dry, there is very little change in the predicted outlet droplet sizes. A humidifier is desirable, however, to reduce loss of water from the column. CCN concentrations as high as 10^4 cm^{-3} did not significantly alter activation behavior due to water vapor depletion.

2.5.2 Experimental Studies of the Single Supersaturation Instrument

The present instrument operated in fixed supersaturation mode was calibrated using monodisperse ammonium sulfate aerosol at a range of particle sizes, temperatures, pressures, and concentrations. A polydisperse aerosol generated by a nebulizer was dried and then classified using a cylindrical differential mobility analyzer (DMA) to produce a dry, monodisperse aerosol. Figure 2.10 shows the variation of the counting efficiency as a function of S_c for different values of ΔT. In all cases, the cold temperature segments were maintained at 290 K, while the temperature of the hot segments was changed to give the reported ΔT. The efficiency curves exhibit behavior that qualitatively matches the simulations (Figure 2.8). As ΔT increases, the S_c at 50% efficiency, S_{50}, increases, since a larger ΔT results in a higher supersaturation. It also appears that the curves are more sharply defined at higher ΔT, as is also predicted. For comparison, the curves are normalized to a maximum counting efficiency of unity. Un-normalized, the counting efficiency reaches $95 \pm 5\%$. These curves demonstrate that, because the efficiency curves change sharply from zero to nearly unity, the CCN instrument can be effectively used as a single supersaturation CCN counter. Simulations of S_{50} do not agree exactly with those measured using the current instrument. The likely explanation for this discrepancy is, again, the temperature difference between the temperature measurement point and the surface of the water film. The actual imposed ΔT is therefore smaller than that obtained by taking the difference

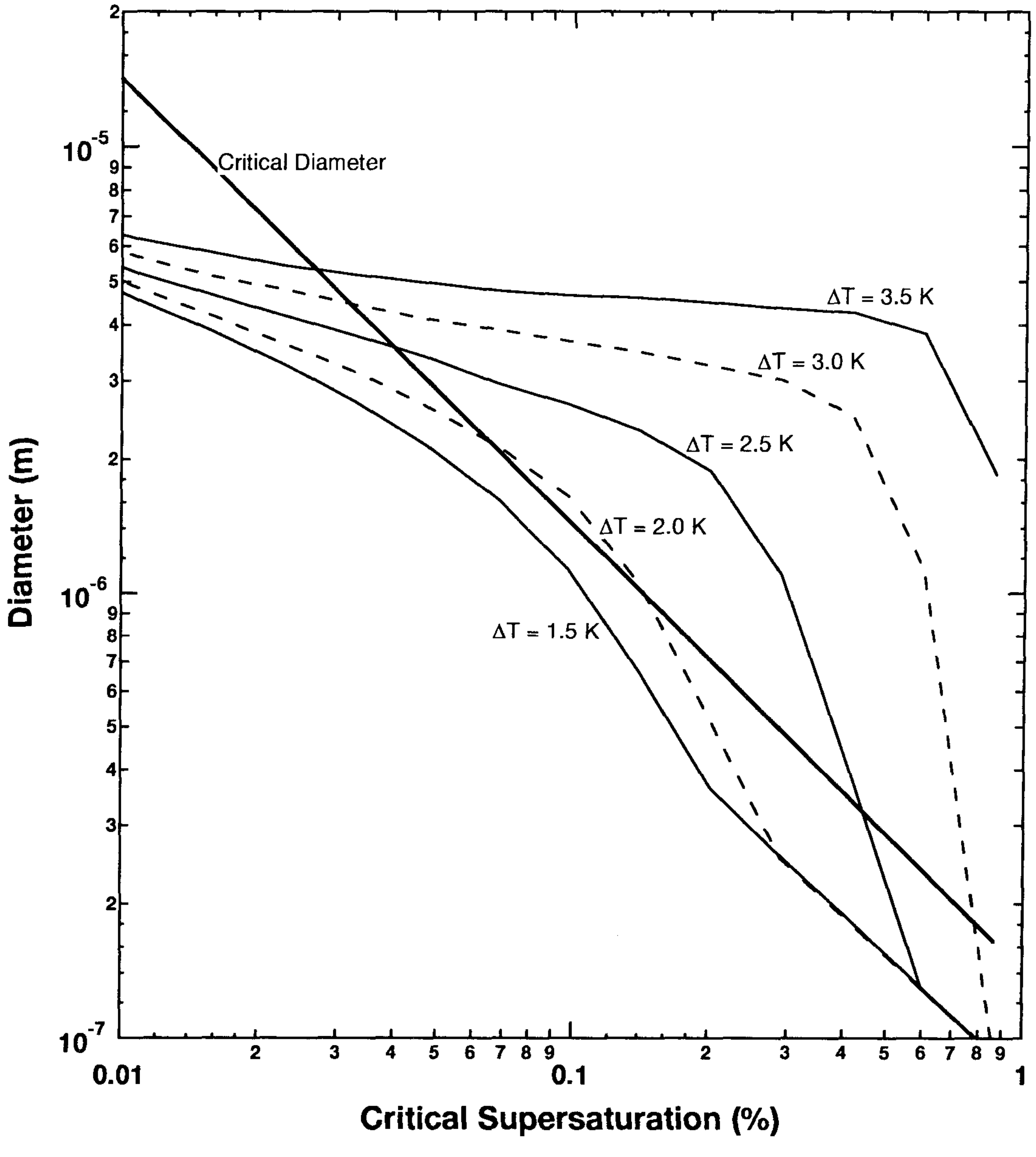

Figure 2.8: Simulations of the effect of temperature difference on the final droplet size as a function of critical supersaturation for the fixed supersaturation CCN counter. For all runs, $p = 1000$ mb.

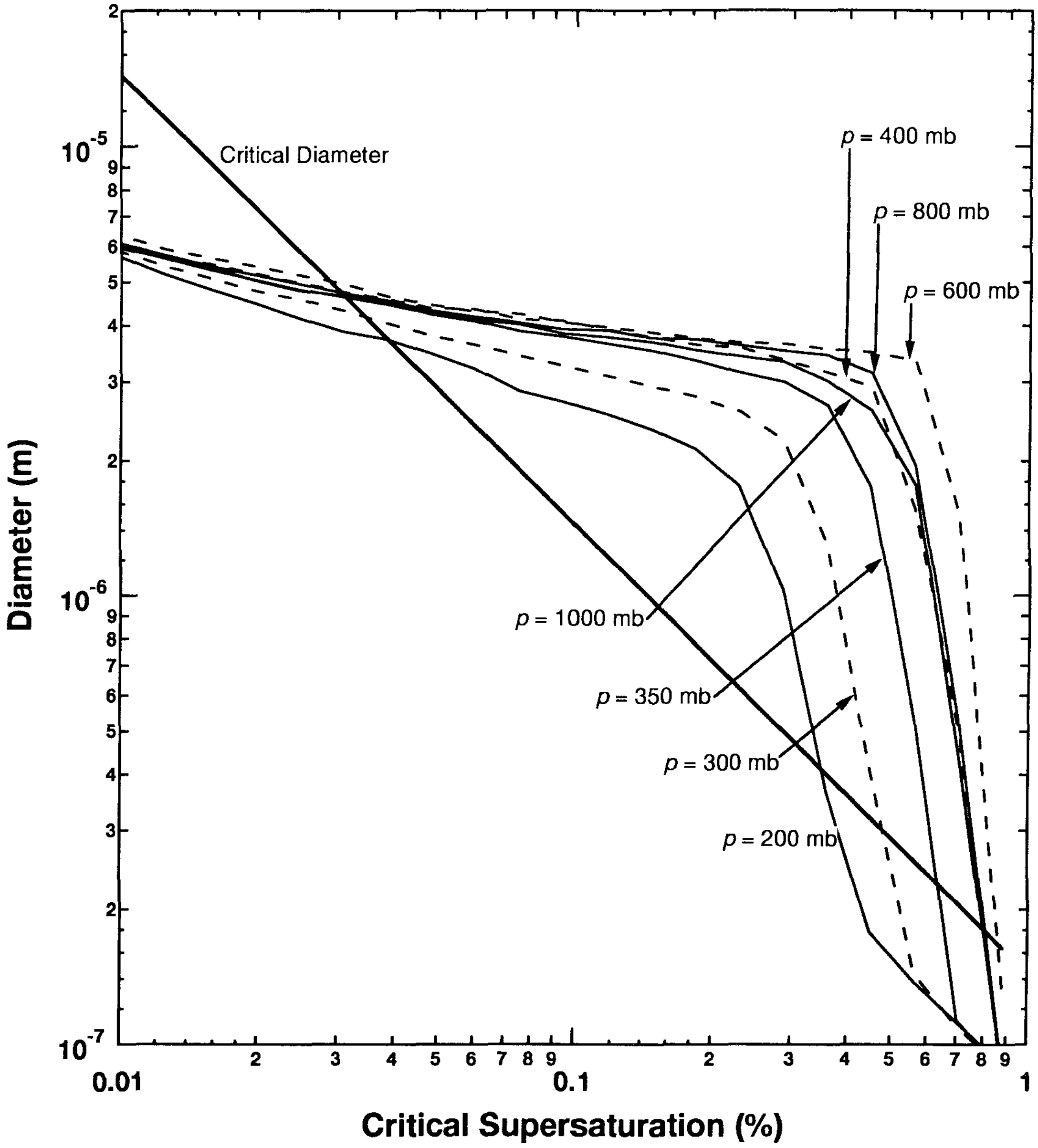

Figure 2.9: Simulations of the effect of pressure on the the final droplet size as a function of critical supersaturation for the fixed supersaturation CCN instrument. For all runs, $\Delta T = 3$ K.

of the temperature set points, accounting for the disagreement between predictions and experimental data.

Because the instrument is designed for airborne measurements, it is important to investigate its behavior as a function of pressure. Figure 2.11 shows the counting efficiency curves measured during experiments performed at five different pressures. For all five cases, ΔT was fixed at 3 K. The model predicts that, for pressures greater than 350 mb, the variations in S_{50} are small (Figure 2.9). The experimental data exhibit somewhat larger changes at low pressures. For pressures 700 mb and above, S_{50} is essentially constant whereas the model predicts a slight increase. At 600 mb and 400 mb, predictions suggest that S_{50} should not differ significantly from the 1000 mb value, but the data show decreases of approximately 20% and 50%, respectively. Again, we speculate that this difference may result from deviations of the temperature profile from that assumed using the model. A complete heat and mass transfer model of the CCN instrument would be needed to resolve these differences completely, but this is outside the scope of the current study.

One interesting feature of the counting efficiency curves is discontinuity of slope at low efficiency (~ 0.15), particularly at lower pressures. Ideally, all particles classified by the DMA possess a single charge, permitting unambiguous calculation of their aerodynamic diameter from electrical mobility. In reality, a fraction of the particles carry multiple charges, so larger particles can exhibit the same electrical mobility as the singly charged particles. The ratio of multiple to single charged particles increases as particle size increases, causing the multiple charging problem to be more noticeable at lower S_{50}. If the data were corrected for multiple charging, the efficiency curves would reach zero efficiency much more quickly.

Instrument performance can also be altered due to depletion of water vapor. If condensational growth at high CCN concentration causes a significant decrease in the water vapor concentration, then the supersaturation would decrease, leading to a decrease in S_{50} with concentration. The instrument response was studied for CCN concentrations between 20 and 1300 cm^{-3}, a range that covers the CCN concentrations expected for most conditions. It was found that the counting efficiency changed

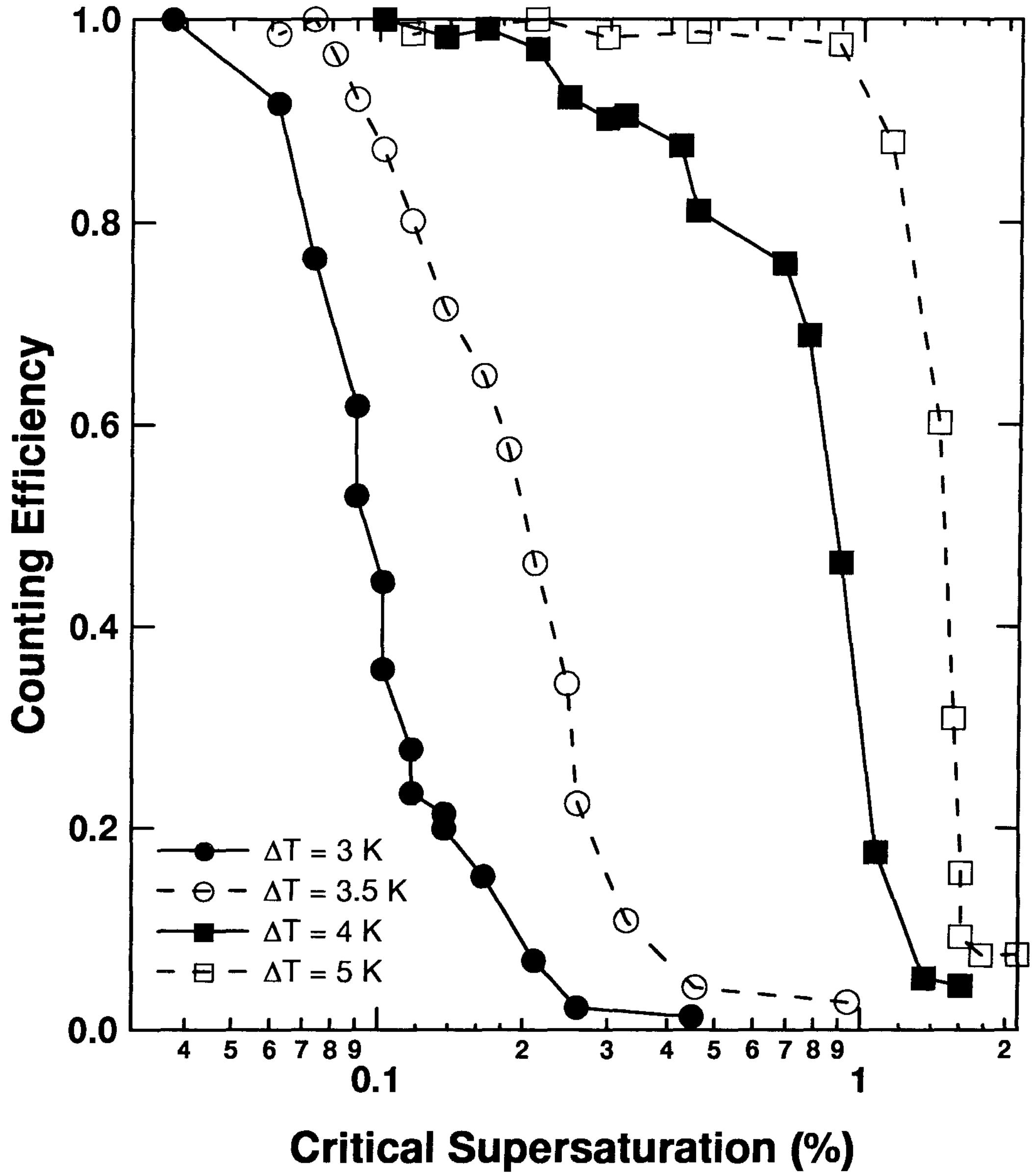

Figure 2.10: Results of experiments studying the effect of temperature on the counting efficiency as a function of critical supersaturation for the fixed supersaturation CCN counter. For all runs, $p = 1000$ mb.

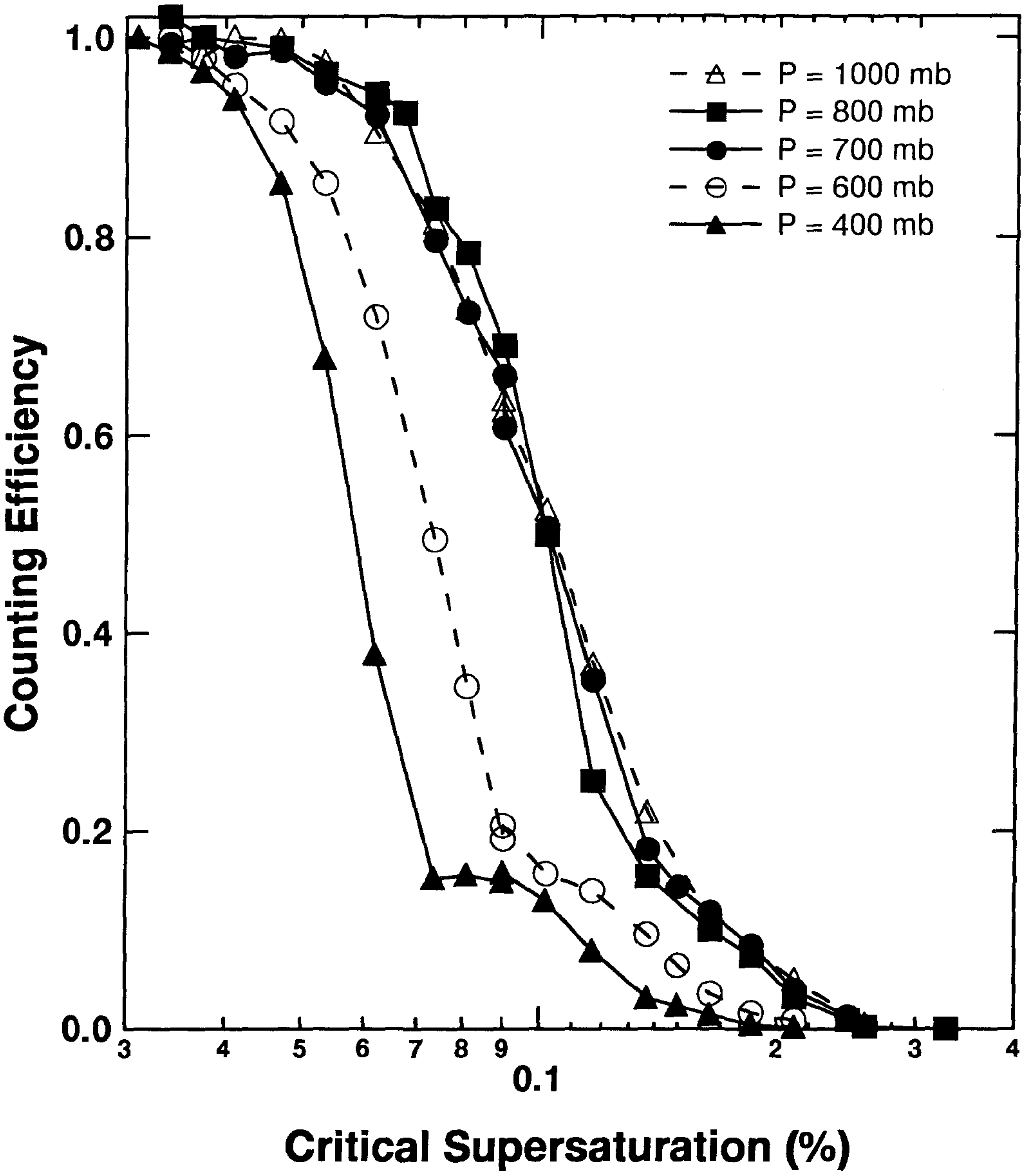

Figure 2.11: Results of experiments studying the effect of pressure on the counting efficiency as a function of critical supersaturation for the fixed supersaturation CCN counter. For all runs, $\Delta T = 3$ K.

very little as a function of CCN concentration (efficiency standard deviation/efficiency average was 0.07), suggesting that water vapor depletion is not a problem for atmospherically relevant CCN concentrations.

A different experiment was conducted to demonstrate that the current instrument can operate as a single supersaturation CCN counter under conditions in which the sample is a polydisperse aerosol instead of a monodisperse aerosol as used for the above experiments. For this experiment, the DMA system is set up in parallel, rather than in series, to the CCN instrument. Dry polydisperse aerosol generated by the nebulizer is used simultaneously as the input for both the CCN instrument and the DMA system. The DMA characterizes the size distribution of the aerosol. Using the efficiency curves calculated for the CCN instrument and the measured aerosol size distribution, the CCN measurement can be predicted and compared with the actual measurement made by the fixed supersaturation CCN instrument. Table 2.1 shows the results of ten such experiments performed for a wide range of CCN concentrations (60 to 2880 cm^{-3}). The average ratio of measured to predicted CCN concentration is 0.96 ± 0.20 ($1\ \sigma$). For six of the ten experiments, prediction and measurement agree to within 6%; all the experiments agree with each other to within about 30%. Some of this variability might be explained by changes in the nebulizer output. The output of the nebulizer is not always constant over the 20 min during which the DMA is characterizing the aerosol size distribution, and any drifting in the source would cause the average size distribution (which is what the CCN instrument measures) to be different from that calculated using the DMA. This observation is supported by the fact that the cases exhibiting less agreement show no trend with respect to CCN concentration (which could be explained by water vapor depletion at the very high CCN concentrations), and show no bias for one instrument to systematically measure a higher value than the other.

Measured Conc. (cm^{-3})	Predicted Conc. (cm^{-3})	Measured/Predicted
60.6	60.3	1.00
91.7	86.9	1.05
109	110	.989
184	188	.977
185	238	1.30
203	156	.776
253	364	.695
930	813	1.14
1380	1470	.942
2880	4230	.682
	Average:	.957
	σ:	.196

Table 2.1: Results of experiments simultaneously measuring the aerosol size distribution and the CCN concentration at a single supersaturation. From the measured size distribution, the CCN concentration was predicted and compared to that measured.

2.6 Summary and Future Work

Field measurements using a new streamwise gradient CCN spectrometer have raised questions about the ability of such instruments to resolve the distribution of atmospheric particles with respect to their critical supersaturations. Modeling studies and calibration experiments have confirmed that streamwise gradient CCN spectrometers have limited capability to resolve supersaturation distributions. Over a climatically important range of critical supersaturations from 0.03 to 1%, the final particle size varies only by 30%. This limited range is difficult to resolve with the optical particle counters that have been used to measure particle size, even for the present instrument that has been optimized for water droplets. One must, therefore, question the ability of streamwise gradient instruments to resolve supersaturation distributions. They do, however, appear to provide good total CCN counts for a single critical supersaturation.

A CCN instrument based on the alternating gradient supersaturation device of Hoppel et al. (1979) has been shown to be well-suited for unattended airborne measurements, even if it cannot measure the entire supersaturation spectrum simultaneously. Since the instrument can probe at most one supersaturation at a time, it is more appropriate to operate it in a fixed supersaturation mode. The instrument has been shown to give sharp S_c cutoff over critical supersaturations ranging from below 0.1% to over 2%. The continuous-flow instrument can make measurements rapidly (<10 s), and can be operated autonomously. Its size, weight, and low power consumption make it particularly well-suited for measurements aboard small aircraft.

Chapter 3 CCN Measurements during ACE-2 and their Relationship with Cloud Microphysical Properties

(Submitted to *Tellus*, 24 January 1999)

Look at the bow in the cloud, in the very rain itself. That is
a sign that the sun, though you cannot see it, is shining still
– that up above beyond the cloud is still sunlight and warmth and
cloudless blue sky.
CHARLES KINGSLEY (1819-75)

Abstract

Measurements of cloud condensation nuclei (CCN) concentration at 0.1% supersaturation in marine conditions were made onboard the CIRPAS *Pelican* during June and July, 1997, in the vicinity of Tenerife, Spain, as part of the second Aerosol Characterization Experiment (ACE-2). The average CCN concentration (N_{ccn}) in the marine boundary layer for clean air masses was 27 ± 8 and 42 ± 14 cm^{-3} for cloudy and clear conditions, respectively, consistent with measurements made near the British Isles (Raga and Jonas, 1995) and close to Tasmania, Australia, during ACE-1 (Hudson et al., 1998) for similar conditions. A local CCN closure experiment was conducted. Measured N_{ccn} is compared with predictions based on aerosol number size distributions and size-resolved chemical composition profiles determined from measurements and the literature. A sublinear relationship between measured and predicted N_{ccn}, $N_{ccn} \sim N_{ccn,predicted}^{0.72}$, was found. This result is consistent with some previous studies, but others have obtained results much closer to the expected 1:1 relationship between measured and predicted N_{ccn}. A large variability between measured and predicted N_{ccn} was also observed, leading to the conclusion that, for 95% of the data, the predictions are accurate to a factor of 8.3. About half the variability with respect to the best-fit relationship is attributed to factors other than instrumental error. Relationships between below-cloud N_{ccn} and aerosol accumulation mode concentration, and in-cloud cloud droplet number concentration, measured onboard the *Pelican* and the Meteo-France *Merlin* IV, respectively, are calculated for periods while the two aircraft were in close proximity at approximately the same time. Measured relationships are reproduced by an adiabatic parcel model, and are also consistent with some previous studies. However, the shape of the CCN spectrum, or the aerosol size distribution, and the updraft velocity are predicted by the model to affect these relationships to a significant extent. Therefore, parameterizations of cloud microphysical properties need to include these variables to accurately predict cloud droplet number concentration. A relationship between N_{ccn} and cloud droplet effective diameter is also calculated and shown to be consistent both with the liter-

ature and with the parameterization of effective diameter proposed by Martin et al. (1994).

3.1 Introduction

Clouds are an important component of the climate system. They reflect incoming sunlight, absorb outgoing longwave radiation, and are one of the controlling factors in regulating the tropospheric content of water vapor, an important greenhouse gas. Clouds are intimately linked to precipitation, a crucial element in climate. Precipitation also plays a role in determining cloud lifetime, in the cycling and ultimate removal of atmospheric aerosols, and possibly in the creation of new particles in the troposphere. Chemical processes that occur within cloud droplets, such as the production of sulfate from SO_2, are also climatically important. Accurately predicting climate change requires an improved understanding of clouds, their influences on climate, and how they will react to changes in atmospheric composition.

To predict climate change, we must understand how anthropogenic aerosol perturbs cloud properties on a global scale. Specifically, it is necessary to understand how cloud properties change as aerosol properties change, i.e., $\frac{d(cloud\ property)}{d(aerosol\ property)}$. Cloud albedo is one important climate-related cloud property; it is thought that increases in the concentration of atmospheric aerosol, or more specifically, that subset of atmospheric aerosol upon which cloud droplets nucleate, termed cloud condensation nuclei or CCN, may cause an increase in globally-averaged albedo. It is estimated that such an increase, the so-called indirect climatic effect of aerosols, could alter the global radiation budget to an extent similar in magnitude, but opposite in sign, to greenhouse gas forcing (IPCC, 1996).

In this work, we will focus on two major questions, both relating to marine stratus clouds. Such clouds are believed to be climatically the most important due to their frequency of occurrence and because their albedo is thought to be particularly sensitive to changes in cloud droplet concentration (Charlson et al., 1992). The first question is whether or not closure can be achieved for simultaneous aerosol size and composition distributions, and CCN measurements. It is generally assumed that, if the aerosol size distribution and chemical composition are perfectly known, then the CCN spectrum is exactly derivable. Several studies (Bigg, 1986; Raga and Jonas, 1995; Hegg et al., 1996; Liu et al., 1996; Covert et al., 1998) have examined the validity of these assumptions by performing a "local CCN closure" experiment, with widely varying results. A closure experiment is one where a property is measured (in this case CCN concentration at one supersaturation) and compared with results derived using independently measured data (in this case aerosol number size distributions and chemical composition). Closure is achieved if the compared data agree within well-established experimental error. We will address the question of local CCN closure using data from a variety of conditions during ACE-2 and compare the results with those of past studies. CCN closure provides confidence in our understanding of the aerosol properties that are relevant to CCN, in our measurement of CCN, and therefore in our use of the CCN spectrum as a controlling variable for microphysical cloud models and parameterizations.

The albedo of a warm cloud is, to first order, determined by the cloud droplet number size distribution, which describes the number concentration of cloud droplets as a function of size, and the cloud depth h. It is commonly (but approximately) assumed that, for the purposes of calculating cloud albedo, this distribution can be sufficiently well described by three parameters: the number concentration of cloud droplets, N_{cd}; the cloud droplet effective diameter, D_{eff}, defined as the ratio of the total droplet volume to the total droplet surface area; and the liquid water content, LWC. Using this parameterization, the optical depth τ_c of a spatially uniform cloud is (e.g., Seinfeld and Pandis, 1998):

$$\tau_c \simeq \frac{1}{2}\pi h N_{cd} D_{eff}^2$$

Cloud albedo R_c can then be approximated by:

$$R_c = \frac{\tau_c}{\tau_c + 7.7}$$

The extent to which the number concentration of CCN, N_{ccn}, and the aerosol number size distribution (or more specifically for this work the accumulation mode particle concentration, N_{ap}, defined as those particles with $D_p > 0.1$ μm) determine cloud microphysical properties, specifically N_{cd} and D_{eff}, is the second important issue addressed in this work. Parameterizations of cloud processes used in climate models currently rely on such relationships to predict cloud properties such as albedo. Identifying the variables that control N_{cd} and D_{eff} is critical for developing physically-based parameterizations that reflect atmospheric processes and therefore are predictive. If N_{ccn} and N_{ap} are not the only significant factors influencing N_{cd} and D_{eff}, what other variables are relevant? Measurements from ACE-2 will be used to examine these questions and the results will be compared to those in the literature. Changes in LWC will not be studied as it is thought that total liquid water content is determined predominantly by large-scale processes rather than microphysical variables. There is evidence that LWC is enhanced in ship tracks (Coakley et al., 1987), which does suggest a microphysical scale influence on LWC, but the data collected for the present study are not suitable for examining this question.

3.2 Instrumentation

During the ACE-2 field campaign (Raes et al., this issue), the Tenerife-based CIRPAS *Pelican* (Bluth et al., 1996) flew a number of missions, both alone and coordinated with other aircraft, in support of the CLEARCOLUMN, LAGRANGIAN, and CLOUDYCOLUMN experiments. Of specific interest in the present work are the four flights supporting the CLOUDYCOLUMN experiment during which the *Pelican* flew below stratus cloud decks while the Meteo-France *Merlin*-IV flew within the cloud deck. Because the *Pelican*'s speed is slower ($\sim$ 60 m s^{-1}) and its flight duration longer ($\sim$ 12 h) than that of the *Merlin* ($\sim$ 90 – 120 m s^{-1}, $\sim$ 6 h), the two aircraft did not fly stacked but rather flew either patterns in the same place but at slightly different times, or non-overlapping patterns that were close to each other, as can be seen in Figure 3.1. The flights took place north or northeast of Tenerife. The DLR Dornier-228 also flew above cloud at similar times during these missions measuring cloud radiative properties, but these data will not be discussed here.

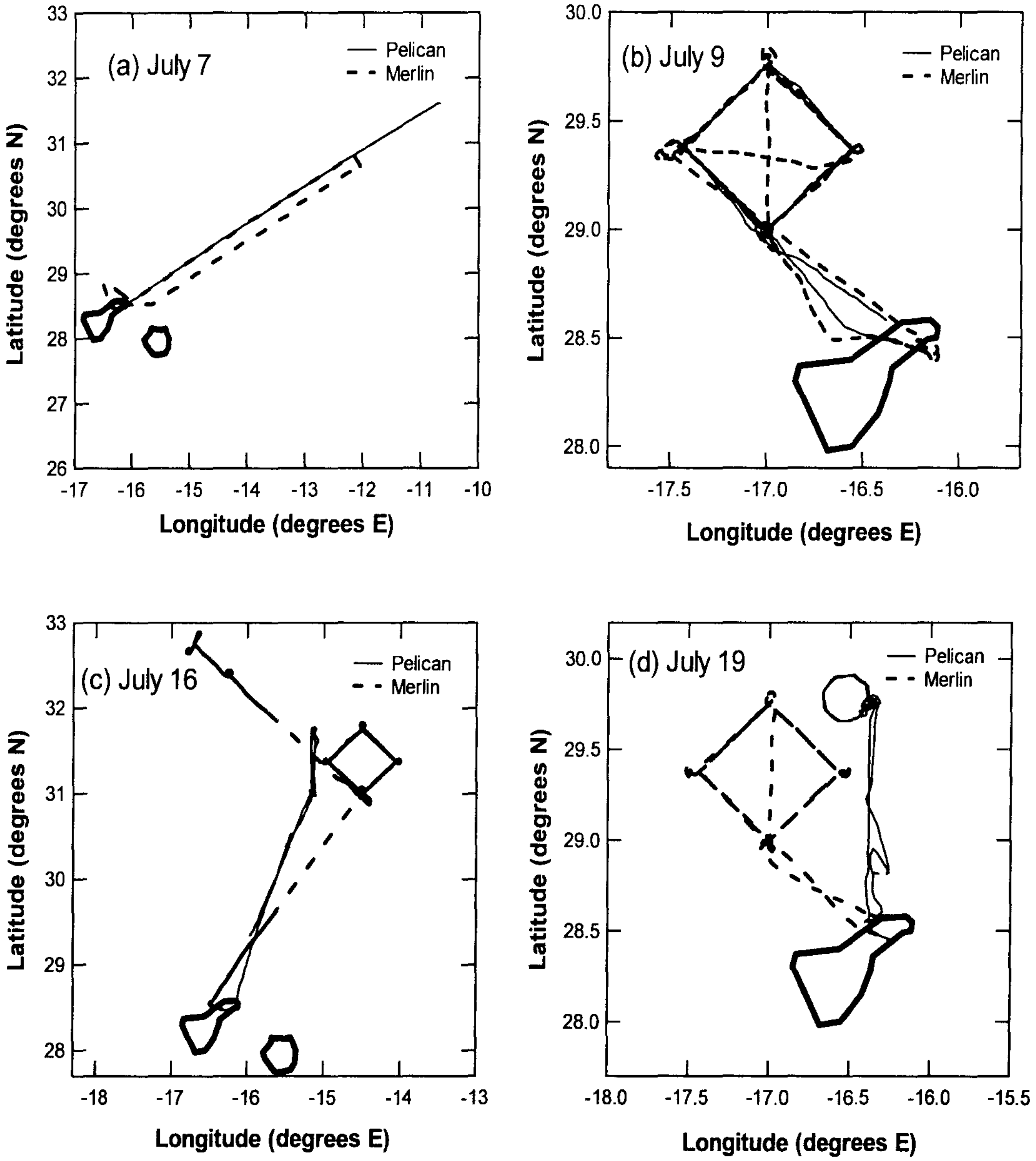

Figure 3.1: Flights tracks for the *Pelican* and *Merlin* for (a) July 7, (b) July 9, (c) July 16, and (d) July 19. The *Pelican* return flight track for July 7 is superimposed on the outgoing leg. Flight track data are not complete for July 16, but the period relevant to this study is shown.

The *Pelican* ACE-2 payload included: the Caltech CCN spectrometer which during ACE-2 measured CCN at a fixed supersaturation of 0.1% at a frequency of one measurement approximately every 60 s; the Caltech Automated Classified Aerosol Detector (or ACAD; Russell et al., 1996; Collins et al., this issue) which measures the aerosol size distribution from 0.005 to 0.2 μm at a frequency of one distribution per 45 s using a radial differential mobility analyzer (or DMA; Zhang et al., 1995); a wing-mounted Particle Measuring Systems PCASP-100X optical particle counter measuring the aerosol size distribution from 0.1 μm to 3 μm; and meteorological data measurements such as temperature, pressure, and relative humidity. A wing-mounted Particle Measuring Systems FSSP-100 was also onboard the *Pelican* but stopped working on July 4, so FSSP data are not available for the CLOUDY-COLUMN flights which all occurred after July 4. The ACAD and PCASP data are combined to produce aerosol size distributions from 0.005 to 3 μm (Collins et al., this issue). The CCN spectrometer and ACAD were both located inside the *Pelican* nose and sampled aerosol through a common inlet which had three identical cyclones in parallel. The two instruments shared the same inlet line up until the last 0.75 m. The cyclones have a nominal cut-off diameter of 2.5 μm.

The *Merlin* ACE-2 payload included: the University of Wyoming CCN counter (similar to that described in Delene et al., 1998) which measured CCN concentration every 40 s for 4 different supersaturations (0.2, 0.4, 0.8 and 1.6%) for a CCN spectrum frequency of one every 160 s; the wing-mounted Meteo-France Fast FSSP (Brenguier et al., 1998) for high frequency (1 Hz during this experiment) data acquisition of the droplet size distribution between 2 and 33 μm; liquid water content using a Gerber PVM 100 probe and a PMS King probe; and meteorological data.

3.2.1 CCN Instrument

The Caltech CCN instrument was designed to operate as a CCN spectrometer during ACE-2, i.e., to produce CCN number concentration as a function of supersaturation. However, during post-processing of the data, several factors were identified that limited stability and resolution of the instrument during its initial field deployment. Changes to the instrument that will correct these inadequacies for future missions have been made. Although these problems limit our ability to invert the raw data to produce CCN spectra for the ACE-2 data set, the instrument can reliably be considered as a fixed 0.1% supersaturation CCN counter for these flights.

The instrument is based on an original design by Hoppel et al. (1979). The Hoppel et al. instrument (originally intended as a condensation nuclei counter) was built using a wet-wall cylindrical column with alternating segments along the column length maintained at warm or cool temperatures to generate a supersaturation profile. The Caltech CCN instrument uses the same principle: a vertically-oriented wet-walled cylindrical tube is axially divided into 14 sections of alternating "hot" and "cold" temperatures. The sample air flows from the top to the bottom of the column. By saturating the air stream at the hot temperature, and then exposing it to the cold temperature, a supersaturation that is maximum on the centerline is generated. By increasing the difference in temperature between the hot and cold sections, and by carefully choosing the flow rate, the aerosol sample is exposed to a monotonically increasing supersaturation profile.

This supersaturation profile leads to activation of those particles with lower critical supersaturation (S_c) earlier than those with higher S_c, which allows the lower S_c CCN a longer time to grow within the wetted column. This creates a situation in which CCN with lower values of S_c can be discriminated from those with higher values of S_c by virtue of having grown larger. Therefore, the droplet size at the column exit, which is optically measured, can be related to the critical supersaturation for each particle (Hudson, 1989). In contrast to a number of CCN counters for which calibration is thought not to be an inherent requirement, calibration of the device is needed to establish the relationship between outlet diameter and S_c.

A specially designed optical particle counter (OPC) was used to measure droplet diameter at the exit of the CCN growth column. It measures the total laser (670 nm) light scattered from each droplet in the near forward direction. This light scattering measurement has been optimized through theoretical and laboratory studies to produce a nearly monotonic response for water droplets 0.7 to 20 μm in diameter. The scattered light pulses from individual particles are converted to a voltage signal using a photomultiplier tube. The peak intensity of each voltage pulse, which corresponds to droplet diameter, is then measured and binned by a multichannel analyzer (MCA), which has 2048 channels from 5 mV to 10 V.

Laboratory calibrations of the CCN counter were performed before and after ACE-2, and field calibrations were performed during the experiment. The instrument was calibrated by generating a nearly monodisperse salt aerosol (ammonium sulfate for laboratory experiments, sodium chloride in the field) by atomizing a salt water solution, drying the resulting aerosol, and selecting those particles within a narrow size range using a differential mobility analyzer. For the purposes of the single supersaturation instrument used for this study, the important result is that for particles whose size is calculated to correspond to 0.1% supersaturation, the channel in the MCA at which the response is maximum is reasonably constant over all calibrations. From this calibration, it is assumed that all droplets larger than this threshold diameter are CCN with critical supersaturations below 0.1%. The effect of changes in this threshold channel has been investigated and found to result in a negligibly small change in the measured CCN concentrations relative to instrumental error for the data considered here.

3.2.2 Instrument Intercomparison

To validate the CCN instrument performance we compare the instrument response against that of other CCN counters for a common aerosol sample. During ACE-2, there were a number of opportunities for such comparisons, mostly with the *Merlin* CCN instrument but also with a similar instrument onboard the MRF C130. Both of these instruments are classic static thermal diffusion CCN counters (Twomey, 1963; Delene et al., 1998). For the C130, there was a 15 min period on July 14 during which the two aircraft flew in close proximity at the same altitude. During this interval, the Caltech and MRF instruments measured N_{ccn} values of 57 cm^{-3} and 47 cm^{-3} at

0.1% supersaturation, respectively.

To estimate CCN concentrations at 0.1% supersaturation from the *Merlin* CCN counter, the CCN spectrum is assumed to follow the parameterization $N_{ccn} = CS^k$ (where S is supersaturation and C and k are fitting parameters). Using the values of N_{ccn} measured at 0.2 and 0.4% supersaturation, the two fitting parameters C and k are determined, from which N_{ccn} at 0.1% is then calculated by using this parameterization. CCN spectra measured from the CCN instrument onboard the MRF C130 (which measured CCN concentration at 5 different supersaturations, 0.1, 0.2, 0.4, 0.6, and 1.0%) during ACE-2 show that this assumption is likely to be reasonable. Much of the time, the CCN concentration at 0.1% supersaturation measured by the MRF instrument agrees well with the value extrapolated from the MRF CCN data at 0.2 and 0.4% supersaturation. For the remaining cases, the number of spectra for which this assumption is an over-estimate of CCN concentration appears roughly equal to the number of spectra for which the opposite is true. Therefore, it is believed that estimation of CCN concentrations at 0.1% supersaturation from higher supersaturation data does not lead to a systematic bias or to errors that exceed the inherent uncertainties in the CCN measurements themselves.

A number of opportunities existed for intercomparison of the *Merlin* and *Pelican* CCN instruments; during 4 periods the *Merlin* and *Pelican* were in close proximity for an extended time. The results from these direct comparison intervals are presented in Table 3.1. The "*Merlin* σ" and "*Pelican* σ" columns give the standard deviation of the mean *Merlin* and *Pelican* concentration data over the interval. The "*Pelican* Number of Measurements" gives the number of data points (which corresponds closely to the number of minutes) available for each interval. Examination of the time series during the first period on July 1 and on July 4 shows that, in contrast to typical conditions, a large amount of variability is observed, especially in the *Merlin* data (relative standard deviations σ/N_{ccn} of 0.76 and 0.71). For these two cases, the agreement is not very good, with ratios of *Merlin* to *Pelican* N_{ccn} of 0.35 ± 0.30 and 0.40 ± 0.30. For the other two periods, less variability is observed and the two instruments appear to agree reasonably well, with *Merlin* to *Pelican* N_{ccn} ratios of

0.73 ± 0.59 and 1.32 ± 0.64. There are also a number of longer periods over 6 flights for which both the *Merlin* and *Pelican* were sampling below cloud at about the same place and time. A comparison of the average N_{ccn} for constant level legs is also shown in Table 3.1. It can be seen that in general the intercomparison agreement is good. The ratio of *Merlin* to *Pelican* CCN concentration averaged over all flights (except those where the data can be reasonably neglected as discussed below) is 1.15 ± 0.15 (1 σ). For July 1, the two *Pelican* measurements with very low concentrations (11 and 15 cm^{-3}) may be a result of rain that was observed in the flight path. On July 4, the concentrations observed by the *Pelican* appear to be systematically higher than those observed by the *Merlin*. This difference may be explained by the fact that the first three legs of the *Pelican* flight were performed beneath a cumulus layer that was present below the stratus cloud deck. The significantly lower concentration measured during the fourth *Pelican* leg that was flown between the cumulus and stratus layers where the *Merlin* was sampling agrees more closely with the *Merlin* data. On July 19, the *Pelican* and *Merlin* flew adjacent patterns (Figure 3.1). The *Merlin* time series shows a strong gradient in CCN concentration, with the air being significantly cleaner towards the north and east where the *Pelican* was flying. It is possible, then, that this could help explain the large discrepancy between the *Pelican*, measuring clean conditions, and the *Merlin*, measuring more polluted air.

3.3 Adiabatic Cloud Parcel Model

An adiabatic cloud parcel model developed at Caltech (Ghan et al., 1999) will be used to aid data evaluation. Model predictions of below-cloud and in-cloud properties of an idealized cloud will be compared with measured relationships. Consistency between predicted and measured relationships provides experimental verification of our theoretical understanding of the underlying physical processes that give rise to these relationships. Differences between the observed and predicted trends suggest that either the measurements need to be improved, or the model does not accurately describe the physical system. Potential measurement problems include: biasing of

Table 3.1: Intercomparison of *Merlin* and *Pelican* CCN measurements at 0.1% supersaturation. Measurements are for periods when the aircraft are below stratus clouds. The data labelled "Direct Comparisons" were obtained during intervals when the two aircraft were simultaneously in close proximity. The rest of the data were measured in approximately the same location but not necessarily at the same time. Time offset typically is 60 min, but could be as large as 340 min.

Date	***Merlin*** **Conc** (cm^{-3})	***Merlin*** σ (cm^{-3})	***Pelican*** **Conc** (cm^{-3})	***Pelican*** σ (cm^{-3})	***Pelican*** **Number of Measurements**
July 01	36	10	34	6	16
			24	8	18
			11	8	14
			32	14	12
			15	6	13
July 04	15	4	30	8	33
			37	13	28
			26	12	28
			22	4	33
July 07	176	46	145	37	27
			161	35	59
July 09	187	82	134	16	65
			143	11	59
July 16	34	12	25	9	29
			30	9	21
			32	10	28
July 19	79	21	27	3	30
			22	3	29
			Direct Comparisons:		
July 01	17	13	48	18	44
July 01	24	19	33	5	14
July 04	14	10	36	11	26
July 09	196	92	148	20	74

the data due to non-isokinetic sampling or droplet shatter; incorrect assumptions about particle refractive index leading to incorrect inversion of optical particle counter data; and changes in the supersaturation profile in CCN instruments due to problems with water delivery. Model predictions could be inaccurate if processes that are not included in the model, such as turbulence, coalescence, and uptake of soluble gases, are important.

Ghan et al. (1999) compare the Caltech model with a similar but independent model developed at Texas A&M; the models yield very similar results for identical input conditions. Both models are based on the dynamic Köhler theory as described by, for example, Seinfeld and Pandis (1998). Entrainment was neglected for the simultations presented in this study. Ghan et al. (1999) used two aerosol size distribution/chemical composition profiles that are relevant to the present study (Figure 3.2). The first, labelled D1, is a size distribution from O'Dowd et al. (1997) characteristic of clean marine conditions. The chemical composition was assumed to be predominantly ammonium bisulfate for particles with $D_p < 1$ μm, and predominantly sodium chloride for larger particles. The second size distribution, labelled D2, is obtained from ACE-2 size distribution measurements from the *Pelican* (Collins et al., this issue) for polluted marine conditions. This aerosol was assumed to be composed solely of ammonium sulfate. Both distributions were used, however, as model inputs under both clean and polluted conditions, by scaling the total number of aerosol particles but not changing the shape of the aerosol size distribution, in order to evaluate the effect of different size distribution shapes on predicted cloud properties.

3.4 Results and Discussion

3.4.1 CCN Measurements

Table 3.2 summarizes CCN concentrations and their standard deviations measured in the marine boundary layer (MBL) during ACE-2. The standard deviations are those calculated from all the CCN concentration data (60 s per datum) available

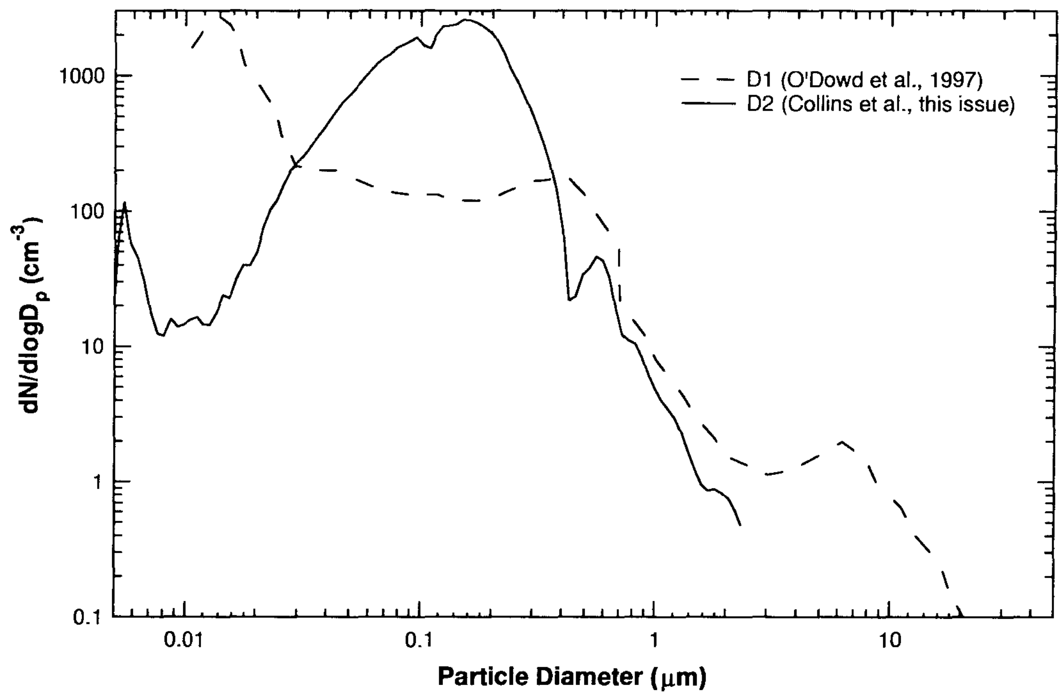

Figure 3.2: Size distributions D1 and D2 used for adibatic parcel model calculations. D1 is representative of clean marine conditions and obtained from O'Dowd, et al. (1997). D2 is representative of polluted marine conditions in the northeast Atlantic as measured during ACE-2 (Collins et al., this issue).

for each interval. Broadly, there are four different conditions during which CCN measurements were made, categorized by two factors: whether the air is clean or polluted; and whether the local conditions are clear or cloudy. Results are reported only for the MBL, which was characterized by high relative humidity (RH). The difference in RH between the free troposphere and the MBL is normally quite large (typically $< 30\%$ for the free troposphere versus $>70\%$ for the boundary layer) and quite sharp, so it is straightforward to distinguish between these environments.

CCN number concentrations from the clean cases can be compared with previous relevant studies. Measurements during ACE-1 over the southern Pacific in the vicinity of Tasmania reported by Hudson et al. (1998) show average CCN concentrations at 0.1% to be roughly 35 cm^{-3} for cloudy conditions, and 50 cm^{-3} for clear conditions. These values are similar to the present data, 27 ± 8 and 42 ± 14 cm^{-3}. The average Northern Hemisphere CCN concentration might be expected to exceed that for the Southern Hemisphere because of anthropogenic influences, but, at least for these two snapshots of data, this expectation is not supported. This finding may not be surprising because back trajectories (not shown) for the clean cases reveal that these air parcels had not come close to continents for at least 5 days, and perhaps longer, such that much of the anthropogenic aerosol should have been removed by the time the air mass was sampled. MBL CCN concentrations were observed to be lower under cloudy conditions than under clear conditions during both studies. The ratios of cloudy to clear CCN concentrations, 0.70 for Hudson and 0.64 in this study, are also quite consistent. This observation might be explained as follows. CCN in a below-cloud air parcel are advected upward and, upon entering the cloud, activate to form large droplets. These droplets coagulate very slowly due to their low diffusivities, but collisions with other droplets due to differential settling or turbulent mixing may reduce the number concentration of droplets in the cloud. When the air parcel subsequently advects downwards and out of the cloud, causing the cloud droplets to evaporate, the total number of CCN is lower. Another possibility is the removal of cloud droplets by precipitation, which would also cause a decrease in CCN number in an air mass that was recently in-cloud.

Table 3.2: Summary of CCN concentrations measured by the *Pelican* during ACE-2 as a function of conditions.

Conditions	**Date**	**Flt #**	**Alt (m)**	**# Data Pts**	N_{ccn} **(cm^{-3})**	σ **(cm^{-3})**
Clear, Clean	July 10	17	92	8	28	6
	July 08	15	57	6	29	4
	July 05	12	1260	29	34	6
	June 30	8	46	17	43	21
	July 05	12	189	28	45	10
	July 05	12	28	31	46	16
	July 05	12	743	28	48	14
Average:				**147 total**	**42**	**14**
Clear, Polluted	July 17	20	61	11	82	13
	July 10	17	88	15	144	49
	July 10	17	650	18	282	85
	July 17	20	645	14	526	103
Average:				**58 total**	**267**	**180**
Cloudy, Clean	July 19	22	509	29	22	3
	July 16	19	20	29	25	9
	July 19	22	44	30	27	3
	July 16	19	50	21	30	9
	July 16	19	37	28	32	10
Average:				**109 total**	**27**	**8**
Cloudy, Polluted	July 18	21	184	26	63	25
	July 18	21	612	26	70	14
	July 18	21	58	28	79	37
	July 18	21	182	25	97	33
	July 18	21	56	24	111	31
	July 18	21	605	25	127	13
	July 09	16	458	65	134	16
	July 09	16	183	59	143	10
	July 07	14	203	67	145	37
	July 07	14	296	59	161	34
	July 09	16	184	9	198	8
	July 09	16	456	10	202	11
Average:				**423 total**	**128**	**43**

Raga and Jonas (1995) report CCN measurements onboard the MRF C130 over the British Isles on May 7, 1992 when "relatively clean conditions" were encountered within a cloud-topped boundary layer. Average CCN concentrations of 25, 35, and 50 cm^{-3} (average = 37 cm^{-3}) were found at 3 different altitudes within the boundary layer (1050, 1500, and 60 m respectively). These values are also similar to the clean cloudy condition average of 27 ± 8 cm^{-3} measured here. Lastly, an average of 30 cm^{-3} has been reported as the Cape Grim historical average for the months November and December (which is roughly the same season as for ACE-2 except in the Southern Hemisphere) for the years 1987 to 1993 (Covert et al., 1998). Cape Grim is a remote coastal site in northwest Tasmania that often experiences very clean air. To estimate CCN concentrations at 0.1% supersaturation from the Cape Grim and MRF data, the averaged measured spectra were extrapolated from the lowest two supersaturation values (approx. 0.5 and 0.2%; and 0.45 and 0.2%, respectively) to 0.1% using the parameterization $N_{ccn} = CS^k$ that, as described above (Section 2.2), is likely to yield reasonable estimates.

3.4.2 Past Studies of Simultaneous CCN and Aerosol Measurements

As discussed above, it is generally assumed that, if the number size distribution and chemical composition of an aerosol is perfectly known, then we can predict exactly the CCN spectrum. It is often further assumed that for determining the critical supersaturation of an aerosol particle, i.e., that supersaturation at which that particle activates, only two parameters are important: the number of moles of solution-phase species in the particle, and the volume of insoluble material present. These assumptions can be tested using CCN closure experiments, in which CCN concentration predicted using measured aerosol size distributions, and chemical compositions that are either assumed or derived from experimental data, are compared with simultaneous CCN measurements. It is important to note that achieving such CCN closure implies that we understand the processes that govern CCN activation in the CCN instrument. It does not imply that we fully understand how CCN activate and grow in actual clouds, as there are several factors that are relevant in clouds that are currently inadequately unaccounted for in CCN instruments, e.g. the kinetics of cloud droplet activation (Chuang et al., 1997), the presence of soluble gases (Laaksonen et al., 1998), and the time profile of supersaturation that an aerosol particle experiences, which is influenced by cloud dynamical processes such as entrainment, and by cloud microphysical factors such as the total CCN concentration. An inability to achieve closure implies that the traditional Köhler equation used to predict CCN concentration measurement data requires additional variables not previously considered in order to accurately do so, or alternately that the CCN concentration, aerosol size distribution, and/or chemical composition measurements are not sufficiently accurate for the purposes of closure experiments. A number of previous studies that have examined local CCN closure are summarized in Table 3.3 and are discussed in more detail below.

Bigg (1986) compared predicted and measured CCN for a wide range of CCN concentrations at Cape Grim, Australia. Predicted CCN concentration was based on measured size distributions and the assumption that the particles were composed solely of either sodium chloride or ammonium sulfate. For two supersaturations, 0.25% and 0.5%, the agreement between predicted and measured CCN concentrations was substantially better for low concentrations. The ratio of measured to predicted N_{ccn} (averaged for 0.25 and 0.5% supersaturation) assuming the aerosol to consist of sodium chloride was 0.76, 0.47, and 0.21 for air with particle concentrations of less than 300 cm^{-3}, between 300 and 3000 cm^{-3}, and greater than 3000 cm^{-3}, respectively. If the aerosol was assumed to be ammonium sulfate, the ratios are 1.1, 0.67, and 0.30. Discussion of these findings follows below.

Raga and Jonas (1995) compared aerosol concentrations measured using a PCASP probe (nominal range 0.1 to 3 μm diameter) with CCN concentrations measured between 0.85 and 0.95% supersaturation. The measurements were made from the MRF C-130 aircraft in marine conditions near the British Isles. A regression of all available data to a straight line in log-log coordinates gave the relationship $N_{ccn} \sim N_{aerosol}^{0.44}$,

Table 3.3: Summary of prior relationships among N_{ap}, N_{ccn}, N_{cd}, and D_{eff} and those for the present study. C. I. and R are the confidence interval and correlation coefficient, respectively.

Variables	**Authors**	**Relationship**	**Notes**
N_{ccn} vs N_{ap}	Bigg (1986)	Sublinear	
	Raga and Jonas (1995)	$N_{ccn} \sim N_{ap}^{0.44}$	95% C.I.: 0.32 to 0.58 0.9% supersaturation
	Hegg et al. (1996)	$N_{ccn} \sim 0.1\, N_{ap}$	Arctic location
	This study	$N_{ccn} \sim N_{ap}^{0.63}$	95% C.I.: 0.58 to 0.68
N_{ccn} vs Predicted N_{ccn}	Liu et al. (1996)	$N_{ccn}/N_{ccn,pred} = 0.9 \pm 0.3$	Chemical data used
	Covert et al. (1998)	$N_{ccn}/N_{ccn,pred} = 0.79$	90% of data between 0.6 and 1.1 TDMA data used
	This study	$N_{ccn} \sim N_{ccn,pred}^{0.72}$	0.1% supersaturation
N_{cd} vs N_{ccn}	Hegg et al. (1991)	$N_{cd} \sim 0.71\, N_{ccn}$ (1% supersaturation)	Clean air masses ($N_{ccn} < 80$ cm^{-3})
	This study	$N_{cd} \sim 0.71\, N_{ccn}$ (0.1% supersaturation) or $N_{cd} \sim N_{ccn}^{0.31}$	95% C.I.: 0.58 to 0.83 $R = 0.9$ 95% C.I.: 0.24 to 0.38 $R = 0.86$
D_{eff} vs N_{ccn}	Vong & Covert (1998)	$D_{eff} \sim -2.9 \ln N_{ap}$ or $D_{eff} \sim -4.6 \ln N_{ccn}$	$R = 0.72$ Derive w/ $N_{ccn} \sim N_{ap}^{0.63}$
	This study	$D_{eff} \sim -4.2 \ln N_{ccn}$	95% C.I.: -3.5 to -4.9 $R = 0.91$

with a 95% confidence interval for the exponent of 0.32 to 0.58. This means that if the aerosol is assumed to be composed of only soluble compounds, then a decreasing fraction of $N_{aerosol}$ is measured as CCN as $N_{aerosol}$ increases. To explain the sublinear relationship between N_{ccn} and $N_{aerosol}$, Raga and Jonas hypothesize that non-hygroscopic aerosol constitute up to 50% of the aerosol by number in polluted air masses. One limitation of this study is that the lowest measurable dry diameter of the PCASP is 0.1 μm, which corresponds to critical supersaturations of 0.10%, 0.14%, and 0.16% for particles of pure sodium chloride, ammonium sulfate, and ammonium bisulfate, respectively. This means that if these salts are representative of the aerosol composition, N_{ccn}, which is measured at around 0.9% supersaturation, in general should be greater than $N_{aerosol}$ by an amount determined by the difference in concentration of CCN that activate at approximately 0.15% and 0.9% supersaturation. Therefore the expected result for successful closure would be a consistent under-prediction of N_{ccn}. This was observed for low $N_{aerosol}$ ($N_{aerosol} < 300$ cm^{-3}) but the opposite was observed for high $N_{aerosol}$.

Hegg et al. (1996) report airborne measurements in the Arctic of CCN at 1% supersaturation along with aerosol number size distributions that were obtained using the combination of a differential mobility analyzer and a PCASP. A comparison of the CCN concentration and the aerosol number concentration between 0.03 and 3 μm revealed a linear relationship, $N_{ccn} \sim 0.1\, N_{aerosol}$. The very low value for the constant of proportionality was attributed to insoluble material.

Liu et al. (1996) examined the relationship between CCN measurements at 0.06% supersaturation at a ground site in Nova Scotia, Canada, using an isothermal haze chamber, and CCN concentration predictions based on a combination of size distribution measurements (from a PCASP measuring 0.135 to 3.0 μm) and chemical composition data obtained from filter samples. Both internal and external mixture models for aerosol composition were examined. The ratio of measured to predicted CCN concentrations averaged over all data was 0.9 ± 0.3 (1 σ). The dominant inorganic anions measured were sulfate, nitrate, and chloride, and the main cations were sodium and ammonium. Acetate, oxalate, and methanesulfonate in general comprised by mass 50 to 80% of the nine particle-phase, water-soluble organics that were individually measured. No measurement of total organic carbon was made. One difference between this study and the others cited is the use of an isothermal haze chamber for measuring N_{ccn}. This instrument does not activate droplets but, instead, measures the equilibrium diameter of particles at 100% RH, so factors that are relevant to droplet growth and activation should not affect the isothermal haze chamber measurements to the same extent that they do classic CCN counters. Thus, it is possible that prediction of the 100% RH equilibrium size may be more easily achieved given a size and chemical composition distribution than the CCN activation spectrum. It is also possible that the authors did indeed achieve local closure within measurement error.

At the Cape Grim site during the ACE-1 field campaign, Covert et al. (1998) measured the aerosol number size distribution using two different DMAs (total range 0.003 to 0.800 μm dry diameter) and CCN concentration at 0.5% supersaturation. In addition, they measured hygroscopic growth factors using a tandem DMA (TDMA) system which selects initially dry ($RH = 15\%$) aerosol at a given size (a total of four different dry sizes, 0.03, 0.05, 0.10, and 0.25 μm diameter were used) and then measures the growth of these particles upon exposure to air at a fixed relative humidity of 90%. This method thereby quantitatively differentiates more hygroscopic aerosol from less hygroscopic aerosol, from which information about the chemical composition can be inferred. By examining the distribution of hygroscopic growth factors, the mixing state of the aerosol can be determined. For example, if all particles exhibit very similar growth factors, then the aerosol is likely to be internally mixed. But if a wide range of growth factors is measured, the aerosol is more reasonably modelled as an external mixture.

Covert et al. found that, when predicted N_{ccn} was plotted against measured N_{ccn} without incorporation of the hygroscopic growth data, the correlation coefficient R for a linear straight line fit was 0.71. When the hygroscopic growth data were combined with the size distribution data to predict N_{ccn}, R increased to 0.84. As a result, Covert et al. concluded that the indirect chemical information obtained from the

TDMA system was useful for N_{ccn} prediction because these data explained some of the variability in the plot of predicted to measured N_{ccn}. Physically, the chemical information increases the accuracy of predicting N_{ccn} by excluding that fraction of the aerosol that is unlikely to serve as CCN because of their limited hygroscopic nature, and by improving estimates of the superaturation at which the CCN activate based on the chemical compositions inferred from the hygroscopic growth rates. The average ratio of measured N_{ccn} to N_{ccn} predicted using TDMA data is 0.79, with 90% of the data lying in the range of ratios from 0.6 to 1.1. However, they also found a systematic over-prediction of N_{ccn} that they could not explain in terms of random instrument error, and as a result, conclude that they could not achieve local closure. The greatest discrepancies appeared to occur for polluted air masses. This result is interesting since previous investigators have assumed that the scatter in a plot of measured versus predicted CCN concentration can be explained by differences in chemical composition and in the mixing state of the aerosol, factors that the TDMA data should take into account.

Further discussion of these local closure experiments follows the next section which addresses the data from the present study.

3.4.3 Current Study

The current study uses the *Pelican* CCN and aerosol number size distribution measurements to evaluate the extent to which local CCN closure can be achieved. CCN data are reported every 60 s, whereas the size distribution data are reported every 90 s. The size distribution measurement closest in time is used to compare against each CCN measurement. Size-resolved aerosol chemical composition data were not available at the same spatial and temporal resolution as the size distribution and CCN data. Instead, flight-averaged chemical profiles were estimated from a combination of filter measurements at Punta Del Hidalgo (PDH), Tenerife, and by making assumptions regarding the relative concentrations of the various components. PDH is located at the northern end of Tenerife at an elevation of 30 m. Because northerly winds generally prevail in this region, PDH is assumed to be representative of marine boundary layer air that is undisturbed by the local islands. Major species measured at PDH are NH_4^+, SO_4^{2-}, Na^+, Cl^-, and both elemental and organic carbon (EC and OC, respectively; Van Dingenen et al., this issue) for both fine ($D_p < 1\ \mu m$) and coarse ($D_p > 1\ \mu m$) aerosol modes. The distribution of sulfate among H_2SO_4, NH_4HSO_4, and $(NH_4)_2SO_4$ was based on observations of the ammonium to sulfate ratio. Sea salt was assumed to be externally mixed with the sulfate aerosol. EC and OC were assumed to be predominantly internally mixed with sulfate and sea salt aerosol with a small amount externally mixed. Volatility measurements in marine conditions in the North Atlantic (Clarke et al., 1996) showed that a majority of particles contained a non-volatile residual core that was composed partially or entirely of EC, supporting this assumption for EC. While no similar data are available to support the assumption that OC is internally mixed, it is believed that organic aerosol originates predominantly from land sources (Cachier et al., 1986) and generally will have become internally mixed through condensation and coagulation over the several days since the organic compounds were emitted. By combining the PDH measurements and these assumptions, a size-resolved chemical composition profile for each flight is obtained. Figure 3.3 shows the chemical composition profiles assumed for the various flights. The two flight days with clean conditions (July 16 and July 19) are characterized by the same chemical profiles, as are the two flights with polluted conditions (July 07 and 09), which is reasonable upon examination of data from PDH for these days (not shown).

A CCN spectrum was then be computed based on these size/composition distributions. The predicted CCN concentration at 0.1% supersaturation was then calculated by summing all CCN with critical supersaturation less than 0.1%. To do so, it was assumed that: the surface tension of the droplets is that of water; all inorganic salts fully dissociate; and the OC and EC fractions are insoluble. For droplets of sizes close to their critical diameter, the solute concentration is fairly low (order 10 mM) so the surface tension correction is small and the important inorganic species are well below their solubility limit. It is expected that the EC fraction is hydrophobic,

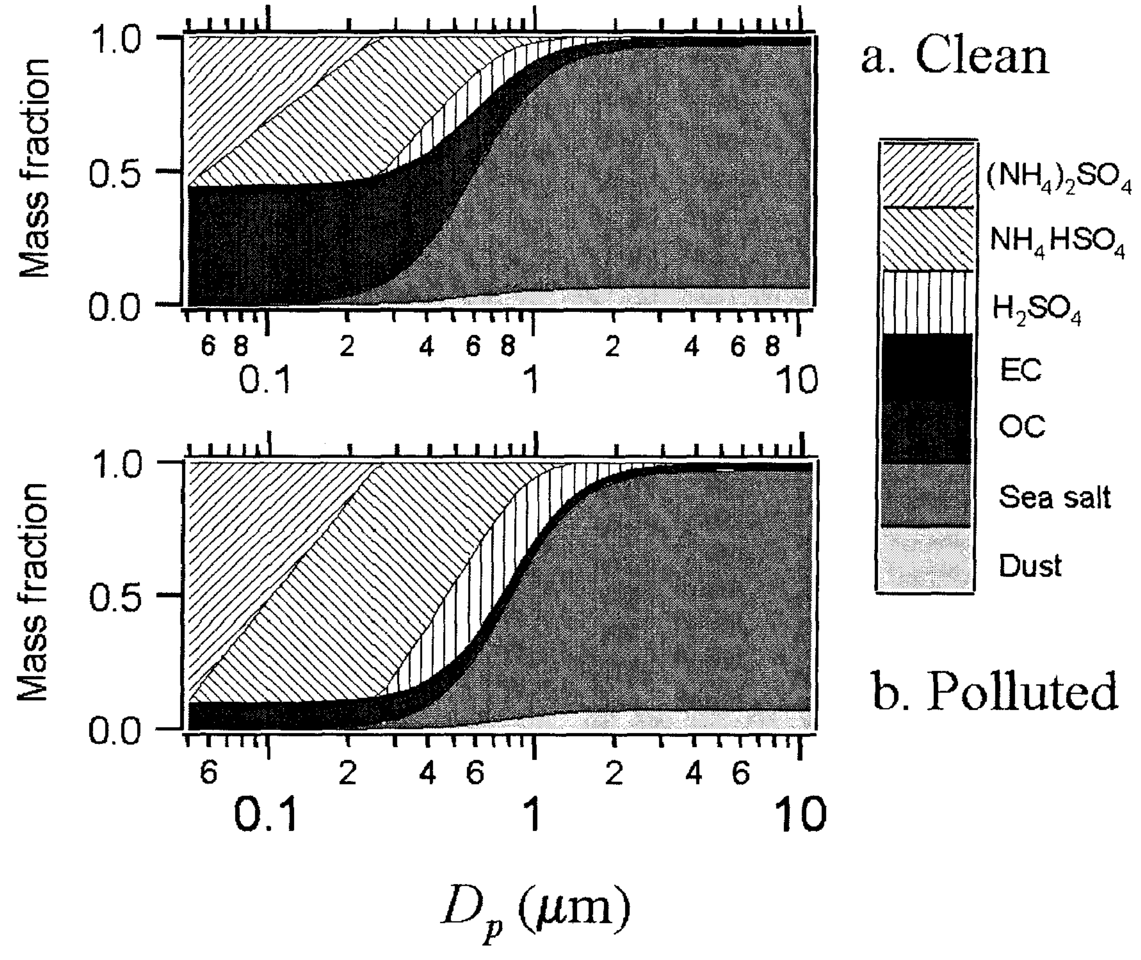

Figure 3.3: Size-resolved chemical composition profiles for (a) clean and (b) polluted conditions that are used together with aerosol size distribution dta to derive CCN spectra (see text).

but it is likely that the OC fraction is partly water soluble, and partly insoluble. The assumption of an insoluble OC fraction leads to a lower-bound estimate of the CCN concentration at 0.1%, as increasing the amount of soluble species by assuming some of the OC to be water soluble would increase the derived CCN concentration by shifting the CCN spectrum toward lower critical supersaturations.

A total of 687 comparisons of measured and predicted CCN concentrations over 9 flights are shown in Figure 3.4. The data were taken in the boundary layer during constant altitude legs in both clear and cloudy conditions. While there is considerable scatter, a regression of all data (except data from July 08, 10, and 19, as explained below) gives the relationship $N_{ccn} \sim N_{ccn,predicted}^{0.72}$, with a 95% confidence interval for the exponent of 0.65 to 0.78, where N_{ccn} and $N_{ccn,predicted}$ are measured and predicted CCN concentration at 0.1% supersaturation, respectively. The large variability observed in Figure 3.4 does not appear to originate only from random instrument error. The average instrumental error as measured by relative standard deviation (σ/N_{ccn}) for all N_{ccn} data is 0.22, with a maximum of 0.49. In comparison, the average ratio of measured to predicted CCN concentration, $F_{ccn} = N_{ccn}/N_{ccn,predicted}$, is 0.45. Therefore, it is unlikely that instrumental random error is the cause of this systematic bias in F_{ccn}. The 2.5 and 97.5 percentile values of F_{ccn} are 0.12 and 1.2 (i.e., 95% of the data falls between 0.12 to 1.2), a difference of a factor of 10. Therefore, we conclude that, for the present study, use of aerosol size distribution and chemical composition data results in predictions of CCN concentration that are, on average, larger than measured N_{ccn} by a factor of 2.2, and are within a factor of 8.3 (= 1/0.12) of the measurements 95% of the time. A different analysis examines the ratio of measured N_{ccn} to that calculated from the best-fit relationship $N_{ccn} \sim N_{ccn,predicted}^{0.72}$, which is on average 1.2, with 66% of the values lying between 1.4 and 0.57 (factor of 2.5), and 95% of the values lying in the range 0.28 and 2.9 (factor of 11). In comparison, the 1 σ variability in F_{ccn} caused by random error is expected to be a factor of 1.5 $(= (1+0.22)/(1-0.22))$. Therefore, the variability expected to result from instrument error is only 60% (= 1.5/2.5) of the observed variability. Thus, we further conclude that 40% of the variations observed with respect to the best-fit relationship are due to factors not considered in the calculation of predicted N_{ccn} in the present study, and that this relationship predicts N_{ccn} to within a factor of 3.6 (= 1/0.28).

Data from July 08 (clear conditions with dust layer aloft), July 19 (clean cloudy conditions), and part of July 10 (polluted clear conditions) lie significantly below the best fit line and are possibly inaccurate. The N_{ccn} data for July 19 were likely affected by an instrument problem. Drying of the CCN column because of a problem in the water delivery system was noted post-flight and is the likely cause of the low CCN concentrations measured. Scaling these data to higher N_{ccn} as suggested from this plot (scaling the data to a mean of around 60 cm^{-3}) improves the agreement of the data relating N_{ccn} with N_{cd} and D_{eff} (described below), which is independent evidence suggestive of an instrument malfunction. The data from July 10 that fall well below the regression line at around $N_{ccn,predicted}$ of 500 cm^{-3} and N_{ccn} of 30 cm^{-3} may also be an instrument artifact, perhaps a result of the change in altitude that occurred just prior to the measurement. The time series (not shown) exhibits a large reduction in N_{ccn} which is not mirrored in the size distribution data. Such responses were not seen for many altitude changes but did occasionally occur. The data from July 10 may also be a result of such problems as there are only a few minutes worth of data at the end of a spiral maneuver. The *Pelican* ascended back into the free troposphere after only a few minutes in the boundary layer so there was no opportunity to observe a relaxation to higher N_{ccn} if it would have happened.

The data from July 17 with very high N_{ccn} correspond to the *Pelican*'s flight path crossing the wake of Tenerife. Integrating the size distribution data yields an estimate of the total aerosol number concentration of 13500 cm^{-3}, reflecting highly anthropogenically-influenced air. Interestingly, these data exhibit F_{ccn} values greater than 2. It is unclear, however, why the recently-emitted accumulation-mode aerosol in this polluted air mass should exhibit such large ratios of N_{ccn} to $N_{ccn,predicted}$ as compared to the rest of the data set.

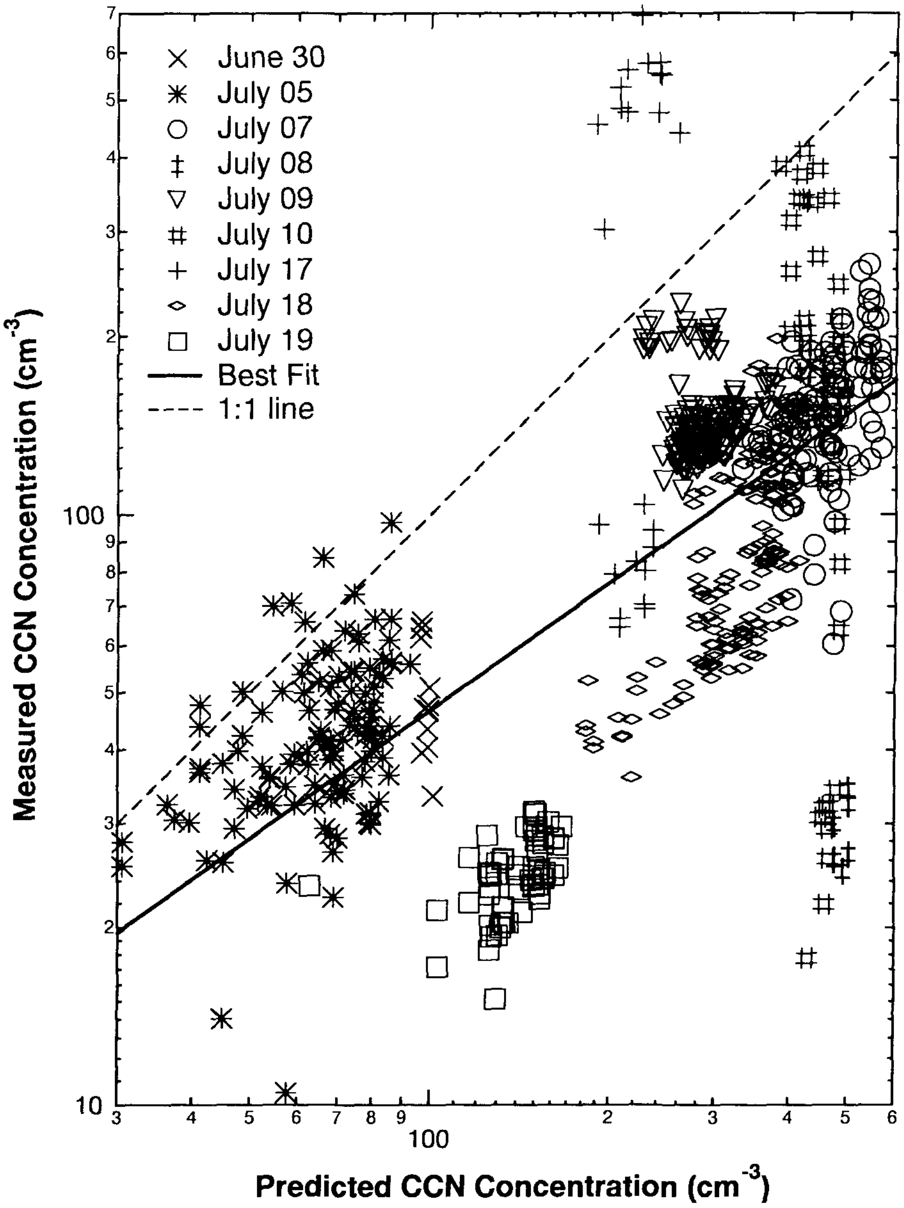

Figure 3.4: Local closure of CCN. Plot of number concentration of CCN at 0.1% supersaturation versus the accumulation mode aerosol concentration (defined as particles with $D_p > 0.1$ μm) for cloudy (closed symbols, e.g., O) and clear (non-closed symbols, e.g., X) conditions. The best fit line does not include part of the data from July 17, and also excludes all of the data from July 08 and 19 (see discussion in text). The error bars for each measurement are not shown; the average relative standard deviation (defined by $\sigma/N_{ccn,measured}$) for the plotted data is 0.22. Error bars for the predicted CCN concentration were not estimated.

3.4.4 Local CCN Closure: Discussion

The studies by Bigg (1986), Raga and Jonas (1995), and the present study suggest that the relationship between measured and predicted N_{ccn} is sublinear, i.e., that the ratio of measured to predicted N_{ccn} decreases as predicted N_{ccn} increases. Such a relationship does not correspond with proper CCN closure. However, these three studies either assume the chemical composition of the aerosol (Bigg, and Raga and Jonas) or infer chemical composition indirectly (present study) and therefore the measurements are not ideal for examining CCN closure. Covert et al. (1998) use TDMA measurements to infer the aerosol mixing state and chemical composition. While they are close to achieving CCN closure, they conclude that the systematic discrepancy between predicted and measured N_{ccn} is real. Covert et al. also state that their data suggest that this discrepancy increases as N_{ccn} increases, which would again reflect a sublinear relationship. Only the study by Liu et al. (1996) appears to achieve CCN closure. The isothermal haze chamber they used to measure CCN may facilitate closure since CCN activation does not occur. Additional studies of CCN closure in a variety of conditions will be required before this issue can be definitively settled.

If a sublinear relationship between measured and predicted N_{ccn} does exist, one possible explanation is depletion of water vapor within a CCN instrument. Given a sufficiently high aerosol loading, all CCN counters will experience a drop in the supersaturation available for growth when the amount of water condensed onto particles becomes a significant fraction of the available water vapor. This would explain decreases in measured N_{ccn} for increasing predicted N_{ccn}. However, it appears that the static diffusion cloud chambers used by Bigg (1986), Raga and Jonas (1995), and Covert et al. (1998) do not experience significant water vapor depletion for CCN concentrations in the range that is relevant to any of the above studies (Delene et al., 1998).

The presence of insoluble and/or organic species in the aerosol in increasing amounts as aerosol concentrations increase is another possible explanation of a sublinear relationship between N_{ccn} and N_{ap}, since polluted air masses tend to contain greater quantities of organic compounds than clean air masses. It is known that organics can modify the traditional Köhler curve by altering the droplet surface tension, by exhibiting slightly soluble behavior (Shulman et al., 1996), and possibly by other mechanisms such as changes in the mass accommodation coefficient. Impeded droplet growth due to organic coatings has been hypothesized to explain observations of delayed droplet growth in static thermal diffusion CCN instruments (Bigg, 1986). The kinetics of CCN activation in CCN instruments could also significantly decrease measured N_{ccn} (Chuang et al., 1997), especially under conditions of high N_{ap}. Such modifications to traditional Köhler theory would change the calculation of the CCN spectrum which would therefore alter predicted CCN concentrations. In the present study, however, the relative abundance of organic compounds is higher for clean air masses than for polluted ones. It is possible, then, that these effects are caused only by those organic species formed from anthropogenic sources and not from naturally occurring ones, thereby causing the observed sublinear behavior. Without detailed organic speciation data in conjunction with the other measurements necessary for local closure, the effect of organics on CCN remains an open question.

3.4.5 Below Cloud Properties vs Cloud CCN Concentration

The formation of a cloud is dependent on a number of variables, some microphysical and others of larger scale. Microphysical parameters include the CCN spectrum, which is related to the aerosol number size distribution and chemical composition. The latter category includes variables such as updraft velocity, cloud thickness, and turbulent mixing. The following sections discuss the relationship between measured CCN concentration N_{ccn} and measured cloud microphysical properties N_{cd} and D_{eff}. A consistent, quantitative relationship among these variables would prove to be extremely useful for parameterizations of cloud properties based on aerosol properties. If N_{ccn} is found not to be the only controlling variable for these cloud properties, it is useful to identify and quantify these other relevant variables. A summary of the results from this section is found in Table 3.3.

Past Studies

Few studies are available from which the relationship between N_{ccn} and cloud properties for marine stratus clouds can be quantitatively inferred. Hegg et al. (1991) measured airborne CCN spectra between 0.2 and 2% supersaturation off the coast of Washington State in and around marine stratus clouds, and cloud droplet concentrations using an FSSP-100. They found that N_{cd} is linearly related to N_{ccn} measured at 1% supersaturation according to $N_{cd} \sim 0.71\,N_{ccn}$ with correlation coefficient R of 0.88. The reported data are, however, limited to relatively clean environments (maximum N_{cd} of 80 cm^{-3}).

Yum et al. (1998) compared CCN data acquired during the ACE-1 campaign (Hudson et al., 1998) with cloud droplet measurements obtained with an FSSP. They found that N_{cd} averaged over entire flights was poorly correlated ($R \simeq 0.3$) with cloud-base N_{ccn} at variety of supersaturations between 0.2 and 1.2%. Using an adiabatic parcel model with measured updraft velocities to predict N_{cd} from CCN data, the authors found greatly improved agreement between predicted and measured N_{cd}. The apparent conclusion is that N_{cd} is a strong function of updraft velocity and therefore incorporation of this information greatly improves predicted N_{ccn}.

Current Study

Because the *Pelican* and *Merlin* did not fly at exactly the same position at exactly the same time, the CCN data and cloud microphysical data are compared by averaging constant altitude legs from each. A typical flight was planned such that the *Pelican* and *Merlin* took off at approximately the same time so measurements made near takeoff were made very close in time. Because of the *Merlin*'s faster speed and shorter flight duration, however, the measurements became progressively separated in time. For the CLOUDYCOLUMN flights, the *Merlin* and *Pelican* average flight durations were 210 min and 340 min, respectively. The average time lag between *Pelican* CCN and *Merlin* FSSP measurements was approximately 60 min with a typical maximum lag of 100 min, although for very long *Pelican* flights the time difference was as much as 140 min. Furthermore, the *Pelican* flight plan typically consisted of multiple levels beneath cloud, usually including at least one near the ocean surface and one just under cloud. However, there is only one constant altitude leg of in-cloud data from the *Merlin* that is available that corresponds to these multiple *Pelican* legs, so the average for each of these below-cloud legs is compared to the same in-cloud microphysical data set. Note that, as described above, it is believed that the July 19 N_{ccn} data are systematically low because of an instrument malfunction. In the following discussions we do not scale these data in any way, although such a scaling would cause only small changes in the quantitative relationships involving N_{ccn}.

Overall, the four flights for which complete data sets are available (07, 09, 16, and 19 July) can be separated into two categories: clean (16 and 19 July) and polluted (07 and 09 July). The N_{ccn} values encountered for both clean flights are approximately the same as can be seen from Figure 3.5. This is also true for the two polluted cases. As a result, the data are grouped closely together with respect to N_{ccn}. Unfortunately, this prevents any meaningful examination of the functional relationship between N_{ccn} and N_{cd}, or N_{ccn} and D_{eff}, since any two-parameter function can be fit to the data. The relationships assumed in analyzing the data from this study, therefore, are guided by past observations.

Figure 3.5 shows N_{cd} as a function of N_{ccn}. Overall, 33 observations were compiled from 103 minutes of in-cloud *Merlin* data and 13 hours of *Pelican* below cloud data. The horizontal bars in Figure 3.5 represent the standard deviation in N_{ccn} (which has a 60 s averaging time) for the observation period. The vertical bars represent the standard deviation in 30 s averaged N_{cd}. Regression of these data assuming a linear relationship (as per Hegg et al., 1991) yields $N_{cd} \sim 0.71\, N_{ccn}$ with an R value 0.9. The 95% confidence interval for the slope is 0.58 to 0.83. The fact that the slopes of the relationship between N_{cd} and N_{ccn} for the current study and for Hegg et al. (1991) are the same is at first surprising since the supersaturations for the CCN measurements were 0.1% and 1%, respectively. These two supersaturations correspond roughly to dry particle diameters of 0.1 μm and 0.03 μm for typical marine boundary layer

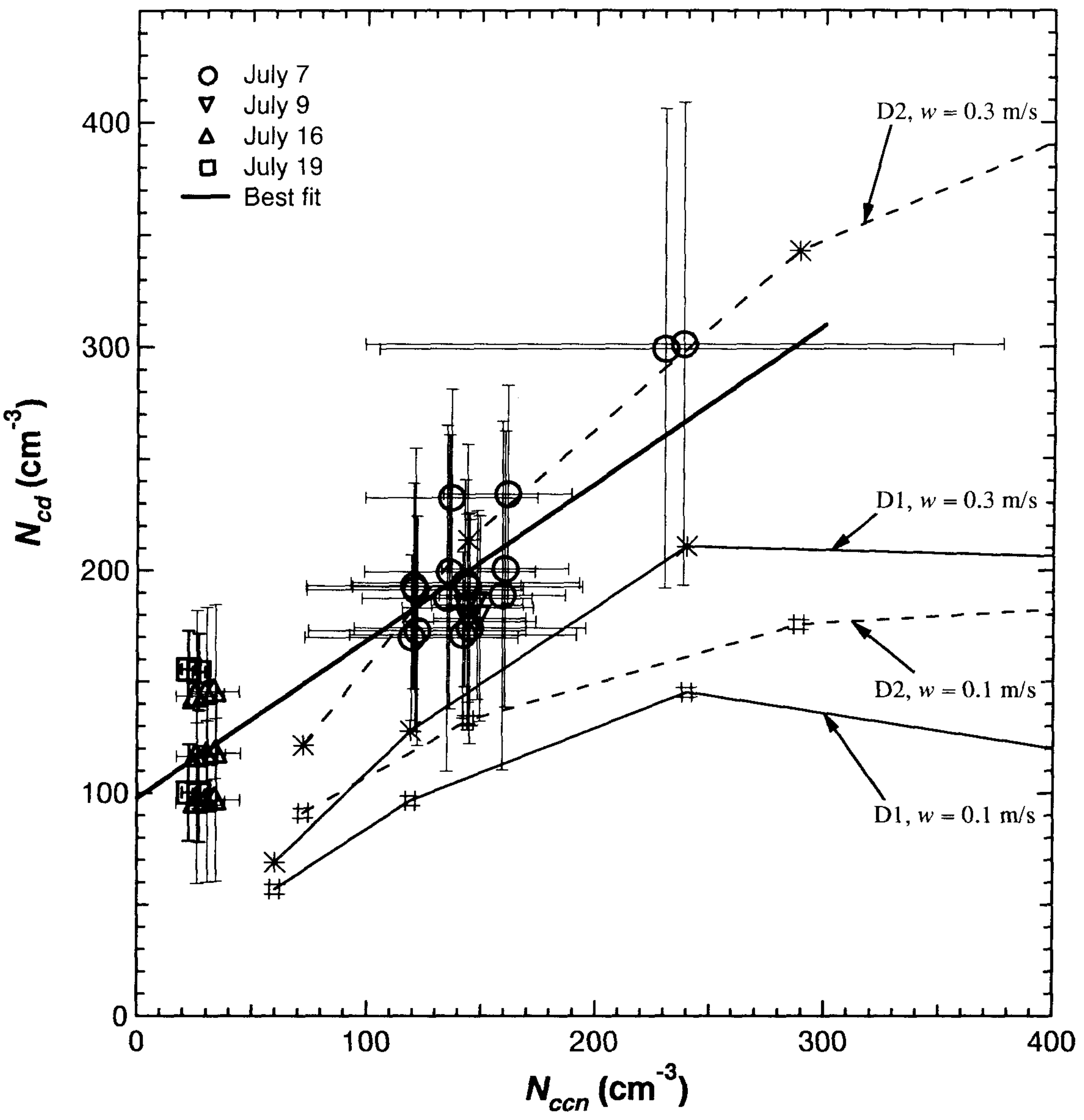

Figure 3.5: Cloud droplet number concentration N_{cd} as a function of below-cloud CCN concentration at 0.1% supersaturation for the four CLOUDYCOLUMN flights. Model predictions correspond to two updraft velocities (0.1 and 0.3 $\mathrm{m\,s^{-1}}$) and two aerosol size/chemical composition distributions (see Figure 1 and text). The horizontal and vertical bars represent the standard deviation in the observations over the averaging period for each datum (see text). The symbols with lines are $N_{cd} - N_{ccn}$ relationships predicted by an adibatic cloud parcel model for two different aerosol size distributions (D1 and D2) and two different updraft velocities w (0.1 and 0.3 $\mathrm{m\,s^{-1}}$).

aerosol. Both relationships cannot be true for identical cloud conditions unless there were no CCN between 0.1 and 1% supersaturation, which is clearly unrealistic. One possible explanation is that the effective supersaturation for stratus clouds during ACE-2 was significantly lower than that during the study of Hegg et al., resulting in similar fractions of 0.1% and 1% supersaturation CCN activating to form cloud droplets. The apparent similarity of the two studies would in such a case not be meaningful but coincidental.

As discussed above, a power-law relationship can just as easily be fitted to the data in Figure 3.5 as a linear relationship since there are only two main groupings of data. A regression of these data using a power-law relationship yields $N_{cd} \sim N_{ccn}^{0.31}$, with an R value of 0.86 and a 95% confidence interval for the exponent of 0.24 to 0.38. It will be argued later that a power law is a more physically realistic relationship for these two variables and, therefore, should be more useful for relating N_{cd} to N_{ccn}.

Effective Diameter

Figure 3.6 shows D_{eff} as a function of N_{ccn}. Again, the horizontal and vertical bars represent the standard deviation in the 30 s and 60 s averaged D_{eff} and N_{ccn} data, respectively. A best-fit curve for the data plotted using a linear scale for D_{eff} and a log scale for N_{ccn} (as per Vong and Covert, 1998) gives the relationship $D_{eff} \sim -4.2 \ln N_{ccn}$, $R = 0.91$, where D_{eff} is in μm and N_{ccn} in cm^{-3}. The 95% confidence interval for the slope is -3.5 to -4.9. For comparison, the data from Vong and Covert follows the relationship $D_{eff} \sim -2.9 \ln N_{ap}$, $R = 0.72$. If one uses the best-fit relationship $N_{ccn} \sim N_{ap}^{0.63}$, which is calculated for the present study using the same data set as Figure 3.4 but without use of the chemical composition data, to convert the Vong and Covert data to CCN data their relationship becomes $D_{eff} \sim -4.6 \ln N_{ccn}$, which is similar to the slope obtained from this study. This similarity suggests that there might exist a consistent relationship between D_{eff} and N_{ccn} in stratus clouds, although more data are required to evaluate this possibility. It is important to note that D_{eff} has been predicted by adiabatic parcel models to depend strongly on cloud height. Ideally, measurements used for determining the relationship between D_{eff} and

N_{ccn} would be made at constant cloud height. A comparison of N_{ccn} with D_{eff} for samples at a variety of cloud heights, as is the case for the present study, would not be expected to result in a single curve, but rather a family of curves, each representing the relationship between D_{eff} and N_{ccn} at different cloud heights. Since the data from the present study are used to predict changes in D_{eff} (rather than its absolute value) as a function of N_{ccn}, it is plausible that the best-fit curve for these data is independent of the variability caused by these sampling complications, and therefore represents the dependency of D_{eff} on N_{ccn} if sampling were accomplished at constant cloud height. However, there is the possibility that D_{eff} was not uniformly sampled from all cloud heights which would cause a bias in the calculated relationship between D_{eff} and N_{ccn}.

Vong and Covert (1998) did not give a theoretical justification for their choice of relating D_{eff} to $\ln N_{ccn}$. Martin et al. (1994) suggest that an appropriate parameterization of effective diameter is $D_{eff} \sim (LWC/N_{cd})^{1/3}$. Assuming that to first order LWC is constant, and that N_{ccn} and N_{cd} are related linearly as found by Hegg et al. (1991), this relationship becomes $D_{eff} \sim N_{ccn}^{-0.33}$. If the data from the present study are also fitted to a power law, the result is the relationship $D_{eff} \sim N_{ccn}^{-0.27}$, with $R = 0.91$ and 95% confidence interval for the exponent of -0.22 to -0.32. If the data from Vong and Covert are similarly analyzed, the result is also $D_{eff} \sim N_{ccn}^{-0.27}$, with $R = 0.71$ and 95% confidence interval for the exponent of -0.23 to -0.30. Although not conclusive, the data from both Vong and Covert and the present study do support the scaling of D_{eff} with N_{cd} for the parameterization proposed by Martin et al. (1994). In contrast, Moeng and Curry (1990) and McFarlane et al. (1992) proposed parameterizations that were dependent only on LWC and not directly dependent on N_{cd}. However, it seems reasonable that for clouds with the same LWC but different N_{cd}, D_{eff} would not necessarily be a constant as calculated by the latter two studies.

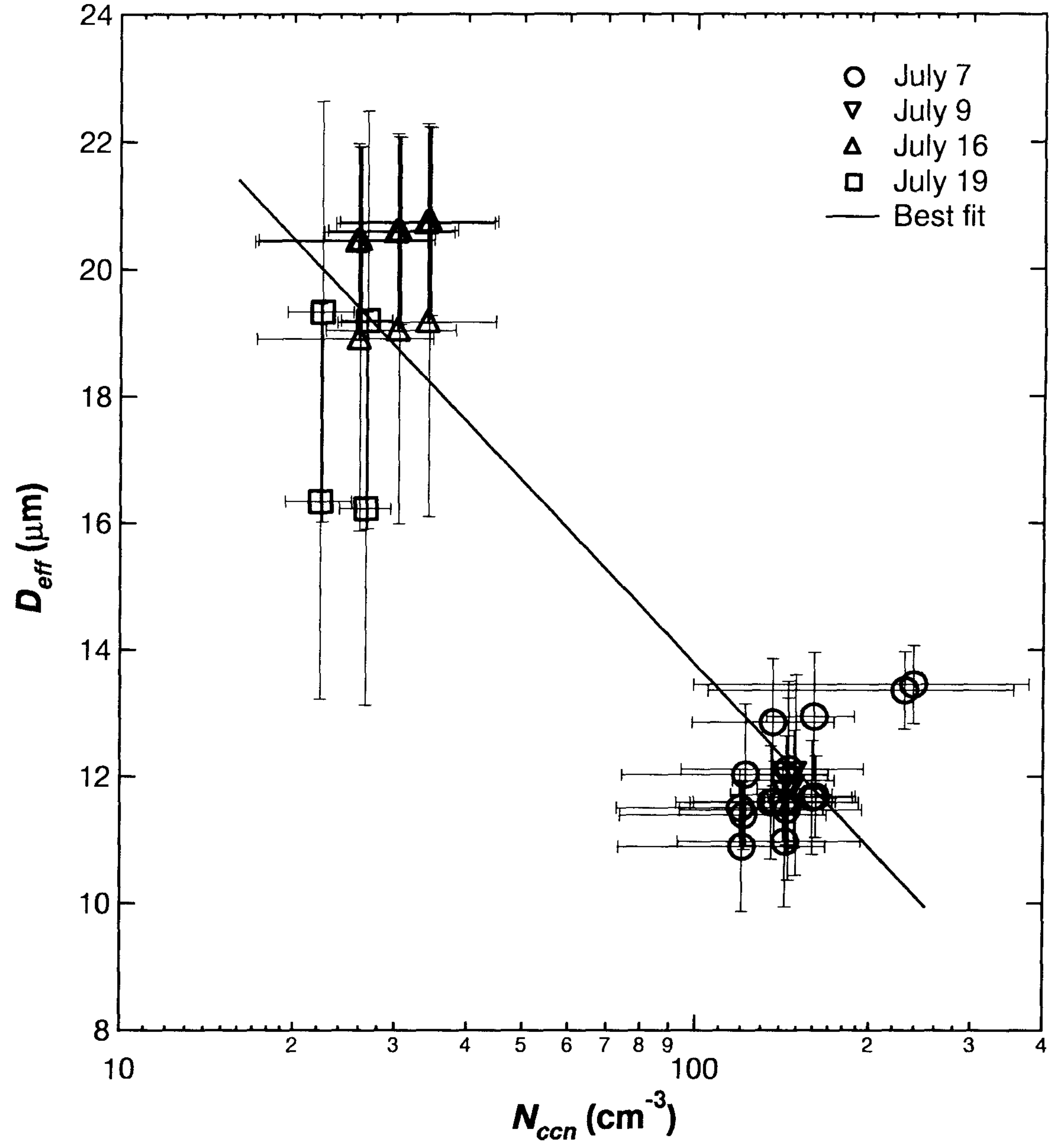

Figure 3.6: Effective diameter of cloud droplets as a function of the below-cloud CCN concentration at 0.1% supersaturation for the four CLOUDYCOLUMN flights. The horizontal and vertical bars represent the standard deviation in the observations over the averaging period for each datum (see text).

3.4.6 Below Cloud Aerosol Number Concentration vs Cloud Droplet Number Concentration

Past Studies

Because many more studies address the relationship between accumulation mode aerosol number concentration N_{ap} and cloud droplet number concentration N_{cd} than between N_{ccn} and N_{cd}, these data will also be presented here and compared with previous work. Table 3.4 shows a summary of the conditions under which previous investigators have examined this relationship. In general, the methods for measuring N_{ap} and N_{cd} are similar although the variations in the size range measured could produce systematic biases in the data, as will be discussed shortly. The data from Pueschel et al. (1986) and Raga and Jonas (1993) are obtained from Slingo and Schwartz (1996), who replotted the data from both studies.

Figure 3.7 shows the results from the studies listed in Table 3.4. The concentrations under the N_{cd} and N_{ap} columns give the approximate range of these variables over the various studies. Fitting all the data together (a total of 185 observations), assuming a straight line in log-log coordinates, gives the relationship $N_{cd} \sim N_{ap}^{0.48}$, R=0.75, with a 95% confidence interval for the exponent of 0.42 to 0.55. The average value of $N_{cd,measured}/N_{cd,predicted}$ where $N_{cd,predicted}$ is obtained from the regression relationship, is 1.1, with 95% of the data lying between 0.30 and 2.1. We therefore conclude that, based on a data set containing a number of different studies, the best-fit relationship for these data can, 95% of the time, predict cloud droplet concentration to within a factor of 3.3 (= 1/0.3). While most of these studies did not report error bars for the data, it is unlikely that all of the observed variability can be wholly accounted for by instrumental error. Factors such as updraft velocity, aerosol chemical composition, and size distribution shape are expected to also contribute to this variability.

There does not seem to be a clear bias due to differences in the smallest or largest sizes measured for determining N_{ap} and N_{cd}. Even though Pueschel et al. (1986) and Martin et al. (1994) defined N_{cd} as droplets larger than 0.5 μm diameter rather

Table 3.4: Summary of studies of cloud droplet number concentration versus below-cloud or in-cloud aerosol accumulation mode number concentration.

Authors	**Location**	N_{ap}	N_{cd}
Pueschel et al.1986 (from Slingo and Schwartz 1996)	Whiteface Mtn, VT	0.1 to 47 μm 100 to 10000 cm^{-3} In-cloud, ambient RH	0.5 to 47 μm 20 to 4000 cm^{-3}
Raga and Jonas 1993 (from Slingo and Schwartz 1996)	British Isles	0.1 to 3 μm 50 to 5000 cm^{-3} Below cloud, dry	2 to 47 μm 20 to 150 cm^{-3}
Martin et al., 1994	California coast S. Atlantic British Isles N. Atlantic (Azores)	0.1 to 3 μm 0 to 1500 cm^{-3} Below cloud, dry	0.5 to 47 μm 0 to 500 cm^{-3}
Gillani et al., 1995	Syracuse, NY	0.17 to 2 μm 160 to 1100 cm^{-3} In-cloud, dry	2 to 35 μm 0 to 1100 cm^{-3}
Leaitch et al., 1996	Nova Scotia, Canada	0.13 to 3 μm 50 to 2000 cm^{-3} Out of cloud, dry	2 to 35 μm 50 to 400 cm^{-3}
Vong and Covert, 1998	Cheeka Peak, WA	0.08 to 47 μm 0 to 1000 cm^{-3} In-cloud, dry	2 to 47 μm 0 to 800 cm^{-3}
This study	N. Atlantic (Canary Islands)	0.1 to 3 μm 80 to 2000 Below cloud, dry	2 to 47 μm 90 to 300

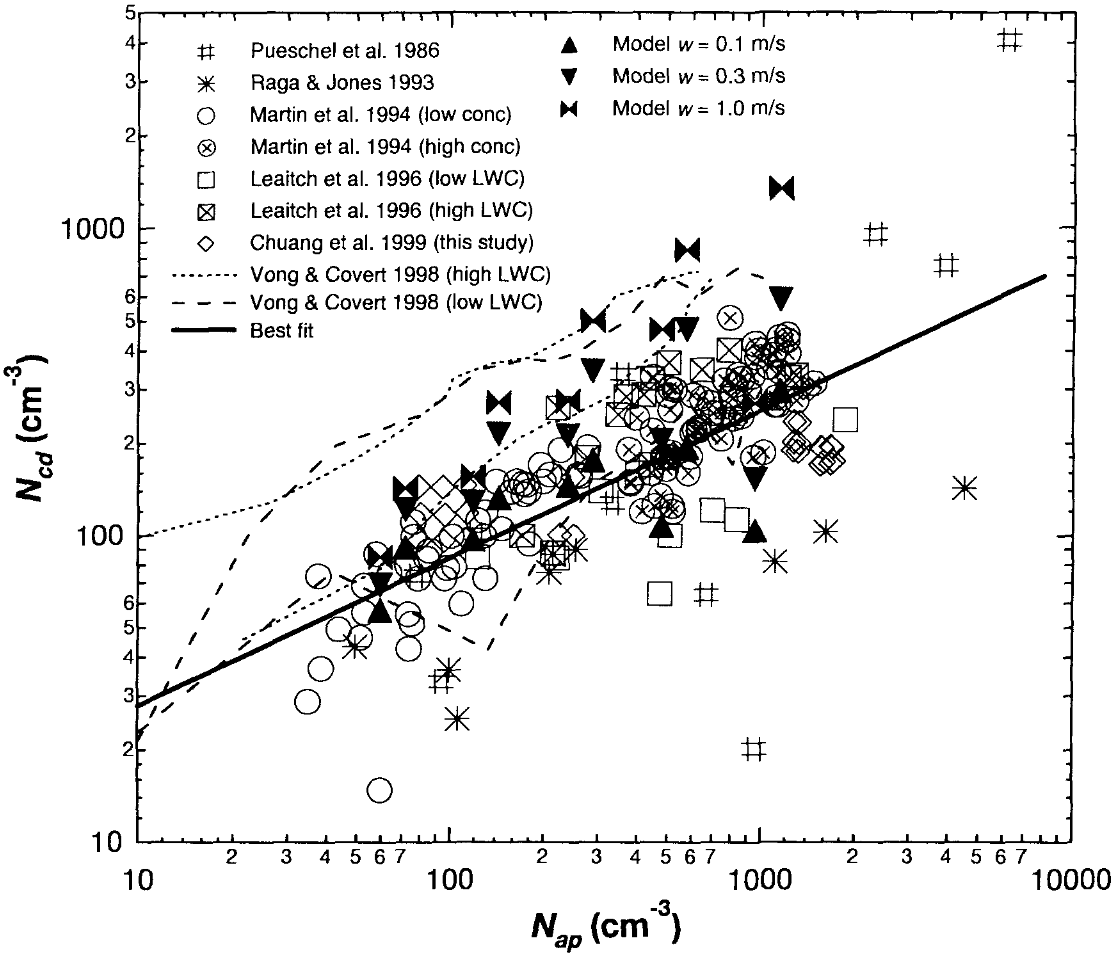

Figure 3.7: Number concentration of cloud droplets as a function of below-cloud or in-cloud accumulation mode number concentration (as defined in Table for each study) for the present study and data found from literature. The lines for the Vong and Covert (1998) data represent the envelope of their data (for both high and low liquid water content cases). The best fit line is a regression of all measurements except for the Vong and Covert data. The model data represents results for both size distributions D1 and D2.

than 2 μm, as used by the other studies, there does not appear to be a systematic shift towards higher N_{cd} in their data relative to the scatter present in the data set as a whole. Similarly, Leaitch et al. (1996) defined N_{ap} to be those particles larger than 0.17 μm diameter rather than 0.1 μm, but no shift towards lower N_{ap} is evident. Although data from Vong and Covert (1998) might be expected to exhibit a shift to higher N_{ap} because they defined N_{ap} to be particles larger than 0.08 μm, the opposite is observed.

Current Study

For an examination of the data from the current study, the comments that apply to comparing *Pelican* N_{ccn} and *Merlin* microphysical measurements apply here also. The data presented are averaged size distributions obtained for exactly the same periods as are used for the CCN comparisons. N_{ap} is defined as the number concentration of particles between 0.1 and 3 μm dry diameter.

Figure 3.8 shows N_{cd} as a function of N_{ap}. A log-log relationship was found to be more appropriate than a linear relationship for these data. Regression of the data yields the relationship $N_{cd} \sim N_{ap}^{0.20}$ with $R = 0.80$ and 95% confidence interval for the exponent of 0.15 to 0.26. This exponent is significantly lower than the value of 0.48 that was found for a regression of all studies combined. In a study in the northeast Atlantic, Raga and Jonas (1993) do, however, find this exponent to be 0.25. Possible explanations for the lower value for the exponent observed here and by Raga and Jonas (1993) as compared with other studies include a consistently greater amount of entrainment or, perhaps, a systematic bias in updraft velocities. Entrainment would lead to a lower value for the exponent because it reduces the value of the maximum supersaturation attained in an air parcel, and as a result a smaller fraction of aerosol would activate to form cloud droplets. A systematically lower updraft velocity would also lead to a lower value of the exponent for the same reason.

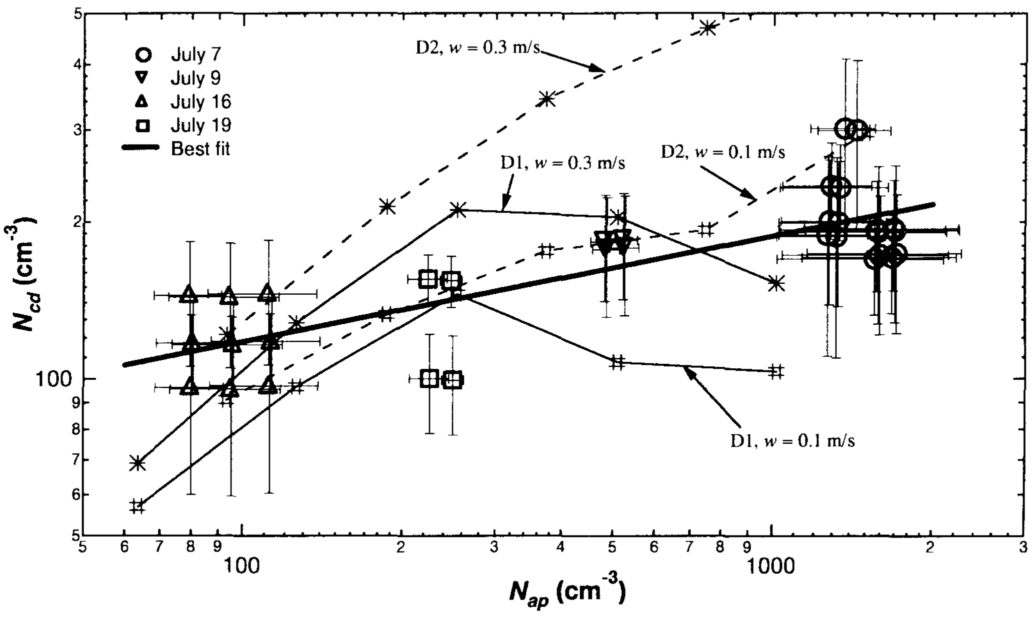

Figure 3.8: Cloud droplet number concentration as a function of the accumulation mode aerosol concentration (defined as particles with dry $D_p > 0.1$ μm) for the four CLOUDYCOLUMN *Pelican* flights during ACE-2. The horizontal and vertical bars represent the standard deviation in the observations over the averaging period for each datum (see text). The symbols with lines are $N_{cd} - N_{ccn}$ relationships predicted by an adibatic cloud parcel model for two different aerosol size distributions (D1 and D2) and two different updraft velocities w (0.1 and 0.3 m s^{-1}).

3.4.7 Discussion of N_{cd}, N_{ccn}, and N_{ap} Relationships

One expects a sublinear relationship between N_{cd} and N_{ccn} and therefore also between N_{cd} and N_{ap}. The latter assumes that N_{ap} and N_{ccn} are related either linearly or sublinearly as is consistent with previous studies and the present study. This expectation occurs because, for all variables held constant except the total number of CCN, an increase in N_{ccn} causes a suppression in the maximum supersaturation achieved in an air parcel that, in turn, should decrease the maximum critical supersaturation of the activated CCN. Therefore, the fraction of CCN that activate is reduced (for constant CCN spectrum) as the total number of CCN increases, resulting in a sublinear relationship between N_{cd} and N_{ccn}.

This effect is shown in Figure 3.5 by the sublinear behavior of the adiabatic cloud parcel model predictions for two size distributions D1 and D2 and two updraft velocities (0.1 and 0.3 $\mathrm{m\,s^{-1}}$). For both the predictions and measurements, N_{ccn} is taken at 0.1% supersaturation, and N_{cd} is defined as those droplets greater than 2 μm diameter at cloud top. The predictions indicate that the slope of the relationship between N_{cd} and N_{ccn} is dependent on both updraft velocity and size distribution shape. Note that cloud thickness was assumed to be 100 m; changing the cloud thickness did not significantly change the predicted relationship between N_{cd} and N_{ccn} and between N_{cd} and N_{ap}. The best fit curve for the ACE-2 measured data agrees fairly well with the predictions for a cloud with an updraft velocity of 0.3 $\mathrm{m\,s^{-1}}$, a reasonable value for marine stratus clouds. The variability in the measured data is comparable to that caused by the different size distributions considered or reasonable variations ($\sim$ 0.1 $\mathrm{m\,s^{-1}}$) in the updraft velocity. The ability of the predictions to describe the qualitative features of the data may indicate that entrainment was not significant in the observed clouds since entrainment was not included in the adiabatic parcel model. We conclude that, while there is a consistent, quantitative relationship between N_{cd} and N_{ccn}, the actual relationship depends on other factors such as updraft velocity and the shape of the aerosol size distribution. This conclusion is consistent with the findings of Yum et al. (1998). Therefore, an important conclusion is that knowledge of N_{ccn} is useful and probably necessary for predicting cloud properties, but it is not sufficient for doing so accurately.

The model predictions also describe qualitatively observed relationships between N_{cd} and N_{ap} (Figure 3.8), although not as well as that between N_{cd} and N_{ccn} (Figure 3.5). The agreement is similar for updraft velocities of both 0.1 and 0.3 $\mathrm{m\,s^{-1}}$. The decrease of predicted N_{cd} at large N_{ap} for aerosol size distribution D1 results from the definition of N_{cd} as those droplets greater than 2 μm diameter. The depletion of water due to increasing N_{ap} shifts the droplet size distribution to sufficiently smaller sizes such that, for N_{ap} larger than 250 $\mathrm{cm^{-3}}$, N_{cd} decreases with increasing N_{ap}. When droplets as small as 1 μm are included in N_{cd}, the curves monotonically increase like those for distribution D2. With this modification, the predictions for an updraft velocity of 0.1 $\mathrm{m\,s^{-1}}$ more accurately match the observations of Figure 3.8. Again, however, it should be noted that updraft velocity and size distribution shape can affect the relationship between N_{cd} and N_{ap}.

Comparing the predictions with the overall data set of N_{cd} versus N_{ap} (Figure 3.7) shows good agreement for model updraft velocities of 0.1 and 0.3 $\mathrm{m\,s^{-1}}$, and poorer agreement at 1 $\mathrm{m\,s^{-1}}$ updraft velocity. This behavior is not unexpected since the latter value is probably too high for typical marine stratus clouds. Variability in the predictions resulting from assumed updraft velocity is quite high, and is roughly the same magnitude as the scatter in the overall data set. This finding suggests that at least some of the variability of the data in Figure 3.7 might be attributable to sampling of clouds formed from air with varying updraft velocity. The magnitude of these variations seems well within that expected for marine stratus cloud conditions. Changes in the size distribution shape do not appear to be as significant as updraft velocity for the two distributions considered here, though it is possible that the range of distributions that are found in the marine boundary layer can cause similar variability in the relationship between N_{cd} and N_{ap}. Therefore, we conclude that N_{ap}, similarly to N_{ccn}, can be used for predicting N_{cd}, but that other variables, specifically the shape of the aerosol number size distribution and the updraft velocity, must also be incorporated to improve such predictions.

3.5 Summary

CCN concentration at 0.1% supersaturation was measured onboard the CIRPAS *Pelican* using the Caltech CCN instrument in the northeast Atlantic during ACE-2. In general, the Caltech CCN data agree well with the Univeristy of Wyoming and MRF CCN instruments for periods when the instruments were measuring the same air mass. The CCN concentration data are consistent with similar measurements in clean marine conditions from previous studies.

A local CCN closure experiment was conducted. Local closure for CCN was not achieved, since a sublinear relationship between measured and derived CCN concentration, $N_{ccn} \sim N^{0.72}_{ccn,predicted}$, rather than a linear 1:1 relationship, best fits the data. This result is consistent with those of some previous studies based upon thermal diffusion cloud chamber measurements (Bigg, 1986; Raga and Jonas, 1995) but inconsistent with observations made using an isothermal haze chamber (Liu et al., 1996). Significant variability in the ratio of measured to predicted N_{ccn} was observed. This ratio lies between 0.12 and 1.2 for 95% of the data, suggesting that predictions of N_{ccn} using aerosol size distribution and chemical composition information as in the present study are accurate to within a factor of 8.3. The variability with respect to the best-fit relationship is also high, leading to the conclusion that 95% of the data lies within a factor of 3.6 of the best-fit prediction. Half of this variability is estimated to result from instrument error, with the remaining unaccounted for. If the observed sublinear behavior and large variability are real phenomena, they suggest that additional variables must be considered in order to accurately and precisely predict CCN measurements. Further studies of CCN closure are required before any definitive conclusions regarding this important issue can be made. Improvements in instrumentation, particularly those that quantitatively measure time- and size-resolved aerosol chemical composition, would be particularly helpful towards this end.

Measured relationships between N_{cd} and N_{ccn}, and N_{cd} and N_{ap}, can be reasonably reproduced by adiabatic parcel model predictions assuming typical size and chemical composition distributions measured in the northeast Atlantic and for typical marine stratus updraft velocities. While these quantitative relationships appear to be a good starting point for parameterizing cloud properties, specifically N_{cd}, model predictions show that updraft velocity and the shape of the CCN spectrum or aerosol size distribution are also important controlling variables and must be taken into account for these parameterizations to be accurate. Model predictions relating N_{cd} with N_{ap} are also consistent with the overall data set compiled from all available literature, although a large amount of variability is observed with respect to the best-fit curve $N_{cd} \sim N_{ap}^{0.48}$. This relationship predicts N_{cd} from N_{ap} to within a factor of 3.3 for 95% of the data. It is likely that some, but not all, of this variability can be accounted for by instrument error. Other factors such as chemical composition, activation kinetics, surface tension modification, and soluble gases may contribute significantly to the remaining observed variations.

The relationship between D_{eff} and N_{ccn} found for this study agrees with the only study found in the literature (Vong and Covert, 1998). The result appears to be consistent with the parameterization of D_{eff} proposed by Martin et al. (1994), and not with those proposed by Moeng and Curry (1990) and McFarlane et al. (1992).

Chapter 4 Kinetic Limitations on Droplet Formation in Clouds

(Published in *Nature*, **390** (6660), 594-596, 1997.)

Derive happiness in oneself from a good day's work,
from illuminating the fog that surrounds us.
HENRI MATISSE (1869-1954)

4.1 Article Text

Note: This section is presented in the same format as it appears in Letters to Nature. *The first paragraph is in boldface and serves as both the introduction and abstract.*

Indirect climate forcing due to the influence of anthropogenic aerosols on the droplet population and therefore the albedo of clouds has been approximately bounded by the range 0 to -1.5 W m^{-2}, averaged globally (IPCC 1996). Observed cloud droplet concentrations are empirically poorly correlated with either measured cloud condensation nuclei (CCN; Twomey and Warner, 1967), aerosol mass concentration (Hegg et al., 1993) or below-cloud aerosol populations (Pueschel et al., 1986). Because cloud radiative climate forcing is very sensitive to changes in cloud droplet number concentration (a 30% increase globally would result in a forcing of ca. -1.0 Wm^{-2}; Charlson et al., 1992), it is necessary to predict cloud droplet number concentrations to within a few percent. Here we show that the assumption that cloud droplet activation occurs as an equilibrium process described by classical Köhler theory can be invalid under certain realistic conditions. We conclude that the discrepancy between measured CCN and cloud droplet concentrations must be due in part to kinetically-limited pre-activation droplet growth. This implies that classical CCN measurements may be unsuitable for use with climate models unless droplet growth rates are considered. Neglecting this effect is estimated to lead to model miscalculations in total cloud radiative forcing that are of the same magnitude as the total greenhouse gas forcing.

Cloud droplet activation and subsequent cloud droplet growth treatments in atmospheric models generally rely on the assumption that pre-activation growth is accurately described by an equilibrium model in which the particle diameter is always at equilibrium with the local supersaturation (Schwartz et al., 1995; Ghan et al., 1993). The equilibrium relationship between supersaturation and particle size for a particle composed of highly-soluble inorganic species can be described by the well-known Köhler equation (Curve A, Figure 4.1; e.g., Seinfeld, 1986). Cloud droplet nuclei (CDN) activate when they grow larger than their critical diameter, D_{pc}, after which they can grow spontaneously, limited only by growth kinetics. The concept of CDN is distinct from that of CCN in that, while CCN are defined as those particles that activate to become cloud droplets within a cloud chamber of fixed or prescribed supersaturation, CDN are those particles that actually activate in the atmosphere under conditions of time varying supersaturation.

To evaluate the conditions under which the equilibrium activation model is valid, two timescales will be defined. One is the timescale for particle growth that would be required for that particle to remain at equilibrium as the ambient supersaturation ratio increases in a rising air parcel, τ_e. The other is the timescale for actual change in the droplet size resulting from condensational growth, τ_g. Hence, if $\tau_e >> \tau_g$ then the equilibrium model is reasonable; otherwise, CDN activation, and hence the cloud droplet size distribution, can only be accurately predicted if the kinetics of droplet growth are considered. To calculate τ_e, the rate of change of the droplet diameter that would be required for that droplet to remain at its equilibrium size, dD_{pe}/dt, is determined from the combination of two effects. First, the time rate of change of supersaturation, dS/dt, can be determined using a simple one-dimensional adiabatic parcel model (Jensen and Charlson, 1984). Next, the rate of change of D_{pe} with respect to supersaturation, dD_{pe}/dS, is determined by differentiating the Köhler relationship. Combining these two expressions yields $dD_{pe}/dt = (dD_{pe}/dS)(dS/dt)$, after which τ_e can be determined from $\tau_e = D_{pe}/(dD_{pe}/dt)$. Similarly, the time rate of change of the particle diameter due to condensational growth, dD_{pg}/dt, can be computed using established expressions (Pruppacher and Klett, 1978; Fukuta and Walter, 1970), after which τ_g can be determined from $\tau_g = D_{pg}/(dD_{pg}/dt)$.

Figure 4.2 shows the two timescales as a function of particle critical supersaturation S_c. The base case parameters given in the caption were estimated for typical marine stratiform clouds (Jensen and Charlson, 1984) which are climatically the most important cloud type (Charlson et al., 1992). The most notable feature of Figure 4.2 is that for $S_c < 0.042\%$, $\tau_g >> \tau_e$, i.e., these pre-activated droplets do not grow

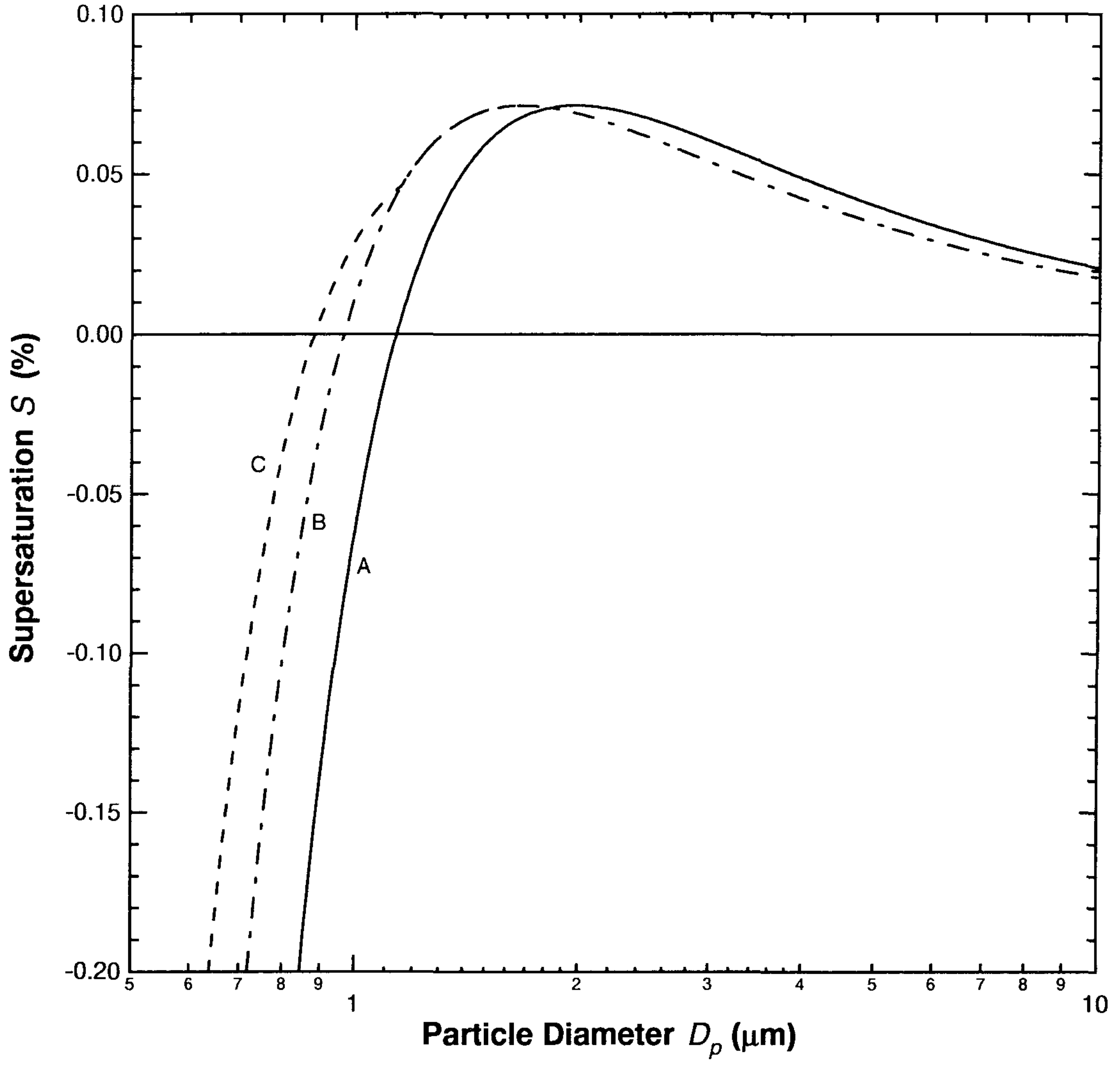

Figure 4.1: Köhler curves for three different particles. All curves are for $S_c = 0.071\%$. For curve A, $\sigma = \sigma_{water}$, and the solute is infinitely soluble. For curve B, σ is lower because of the presence of an organic species, so $\sigma = 0.85\,\sigma_{water}$, but the solute is still infinitely soluble. Curve C is the same as curve B, except the organic solubility is assumed to be 0.02 M. D_{pc} shifts from 1.97 μm in curve A to 1.67 μm in curves B and C because of the surface tension decrease. Curves B and C join together when the organic fraction of curve C fully dissolves.

sufficiently quickly to follow the changes in the equilibrium diameter, implying that for particles with $S_c < 0.042\%$ (e.g., pure NH_4HSO_4 particles of size $> 0.23\ \mu$m dry diameter), condensational growth kinetics are important. The fraction of CCN in this regime can be estimated using the common empirical parameterization of the cumulative CCN spectrum, $N = CS^k$, where N is the CCN number concentration, S is the supersaturation, and C and k are empirically determined parameters. If the peak supersaturation achieved in an air parcel is S_{max}, the fraction of CCN for which growth kinetics are important is $(S_c^*/S_{max})^k$, where S_c^* is the value of S_c at which $\tau_e = \tau_g$. When this fraction is significant, accurately predicting cloud droplet size distributions requires a kinetic description of CDN pre-activation growth. Assuming a value of S_{max} of 0.1%, this fraction is 0.76, 0.63, and 0.53 for k values of 0.3, 0.5, and 0.7, respectively, for the base case of Figure 4.2. These exponents are representative of data from observations of marine stratiform clouds (Hobbs, 1993).

The sensitivity of S_c^* to temperature, pressure, droplet diameter, updraft velocity, and thermal and mass accommodation coefficients is presented in Figure 4.3. The base case is seen actually to be a conservative estimate of S_c^*, since almost all the values in Figure 4.3 lie above $S_c^* = 0.042\%$. Changes in pressure and temperature do not greatly affect S_c^*. Changes in the updraft velocity are more significant since dS/dt is directly proportional to this quantity. S_c^* is sensitive to changes in the accommodation coefficients only if α_t or α_c is less than 0.1. Values for α_c in the range of 0.03 to 1.0 have been reported (Mozurkewich, 1986). S_c^* is most sensitive to the particle diameter (increasing by more than a factor of 2 for a 50% change in diameter) primarily because τ_g is directly proportional to D_p^2. This implies that a particle that began in the equilibrium regime may, due to condensational growth, cross over into the kinetic regime while it is still unactivated, indicating that the fraction of particles for which growth kinetics is important is even higher than estimated in the base case.

There is initial evidence that organic compounds comprise a significant fraction of CCN mass (Novakov and Penner, 1993; Rivera-Carpio et al., 1996) and can alter a particle's Köhler curve (Shulman et al., 1996). The effect of organics on τ_e and τ_g can be divided into three distinct factors: (1) changes in the droplet surface tension;

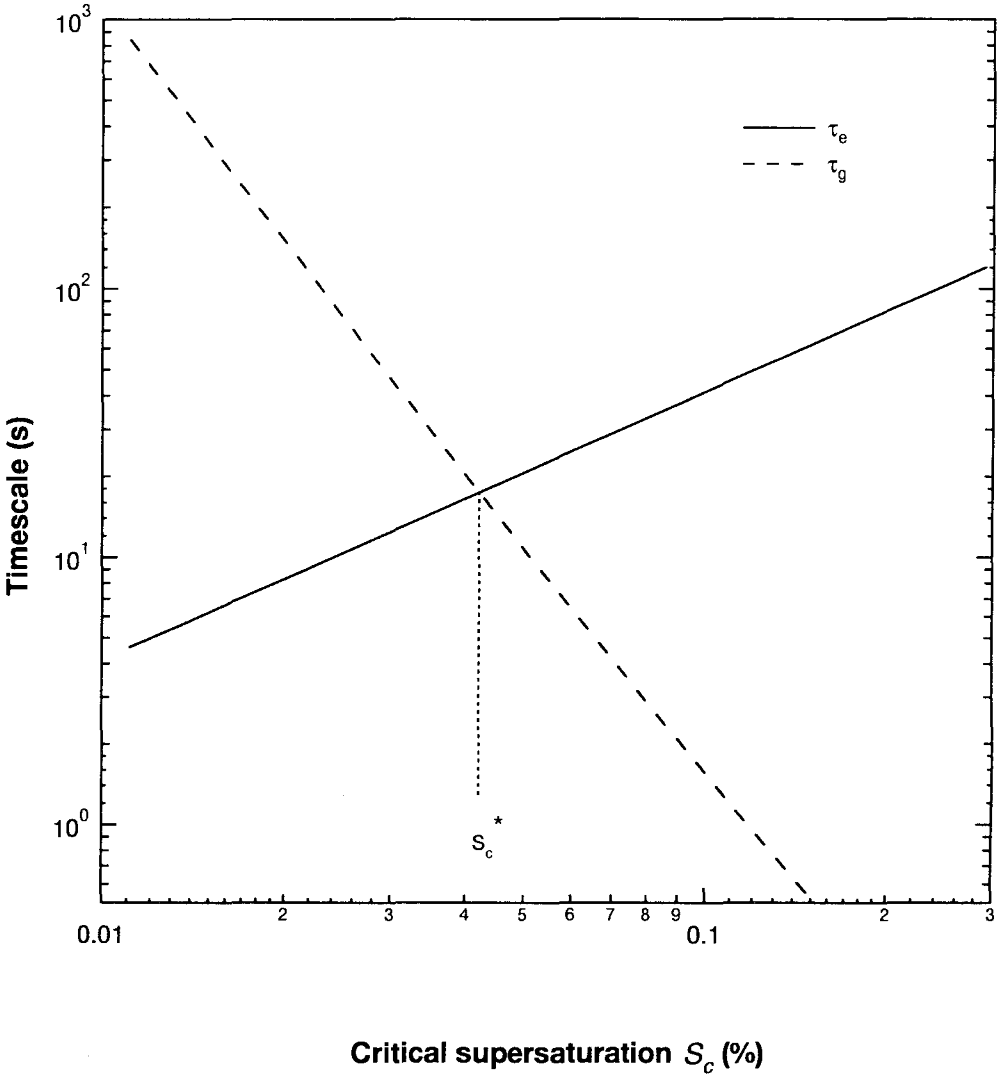

Figure 4.2: Base case comparison of the equilibrium (τ_e) and droplet growth (τ_g) timescales as a function of critical supersaturation. Base case parameters are temperature $T = 280$ K, pressure $p = 900$ mb, updraft velocity $u = 20$ cm/s, and mass (α_c) and thermal (α_t) accommodation coefficients equal to unity. To calculate the timescales, a diameter must be specified; the equilibrium diameter at 100% relative humidity was chosen for the base case. It can be seen that S_c^* is a good indicator of the transition from kinetic to equilibrium regimes because the ratio τ_e/τ_g is a strong function of critical supersaturation. Note that there is an inverse relationship between S_c and particle diameter. For example, an ammonium bisulfate particle with $S_c = 0.01\%$ has a dry diameter of 0.6 μm, and for $S_c = 0.2\%$, dry particle diameter is 0.09 μm.

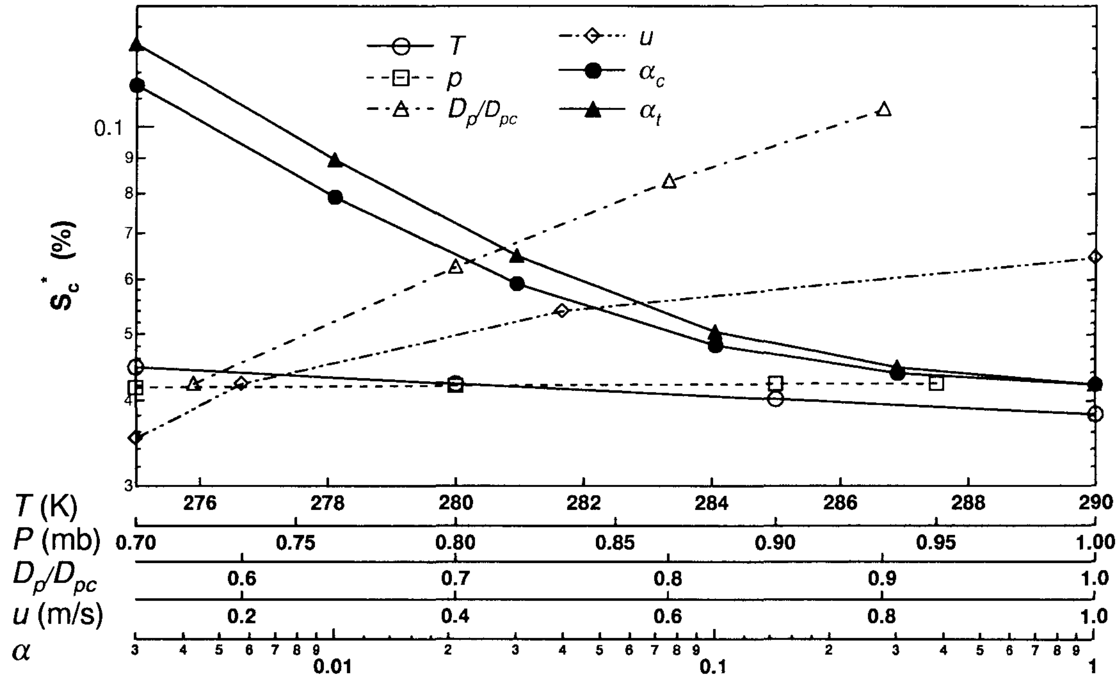

Figure 4.3: A study of the sensitivity of S_c^* to various parameters. The base case value is 0.042%, which is lower than most of the values plotted. Temperature and pressure cause the smallest changes, whereas updraft velocity and the accommodation coefficients are more important. The specified diameter D_p causes the greatest change in the value of S_c^*. D_{pc} is the critical diameter, i.e., the size at which the particle is considered to be activated. The base case, where D_p is that at 100% relative humidity, corresponds to $D_p/D_{pc} = 0.577$.

(2) gradual dissolution of solute due to limited solubility; and (3) changes in the mass accommodation coefficient.

The presence of water-soluble organics decreases in varying amounts the surface tension of these solutions (Shulman et al., 1996). In the absence of any other perturbations, a decrease in the droplet surface tension σ by $\Delta\sigma$ can be shown to decrease the critical diameter by a factor of $\Delta\sigma/\sigma$, as illustrated by curves A and B in Figure 4.1. One consequence of this decrease is to increase τ_e because at a given value of S, curve B is shifted to smaller sizes relative to curve A, which causes a decrease in dD_{pe}/dS. Another consequence is that τ_g decreases by approximately $2\Delta\sigma/\sigma$ because

τ_g is directly proportional to D_p^2. The combination of these effects shifts S_c^* to smaller values. Using the base case parameters, for $\Delta\sigma/\sigma = 15\%$, τ_g increases by about 15%, τ_g decreases by 28%, and S_c^* decreases by 11%. As a result, the fraction of particles in the kinetic regime decreases by 6%.

If the solubility limit of the organic fraction in a droplet is reached, then the amount of solute within that droplet increases as the droplet grows in order to maintain saturated conditions. Qualitatively, the gradual dissolution of organics broadens the Köhler curve as illustrated in curve C, Figure 4.1. In some cases, local maxima and minima can arise in the Köhler curve when organic components fully dissolve (Shulman et al., 1996). The overall effect of gradual dissolution on both time constants appears to be small compared to surface tension effects for realistic conditions. We do not consider here a possibly related effect, the kinetics of dissolution.

It has already been shown that S_c^* changes rapidly with changes in the condensation coefficient α_c for $\alpha_c \leq 0.1$ as a result of changes in τ_g. Many organics can be present at the solution/air interface in quantities in excess of the bulk average as a result of their partially hydrophobic nature (Stumm and Morgan, 1981). Organics can change the evaporative properties of bulk water even in minute quantities (Barnes and La Mer, 1962). Therefore, it seems plausible at least that organics could cause substantial changes in α_c, and therefore S_c^*, although no attempt at quantifying such an effect will be made here.

There does not appear to be any observations of CDN and cloud droplets where the full set of possible controlling variables has been measured. It may not in fact be presently possible to make the necessary measurements in-situ that could support or negate the above model calculations. However, there is evidence that cloud droplet growth can be delayed in cloud chambers (Bigg, 1986). Such an effect has been attributed to the presence of an organic coating (Bigg, 1986), but kinetic variations of activation could also explain these observations.

Neglecting kinetic limitations on pre-activation droplet growth has direct consequences on cloud droplet populations, and therefore cloud radiative climate forcing. First, models that use an equilibrium assumption such as $N = CS^k$ must overestimate the droplet number concentration that actually would form because some of those droplets fail to activate due to kinetically-limited growth. To estimate the error in cloud droplet concentration and hence the magnitude by which the equilibrium activation model overestimates cloud radiative forcing, results from the approximation $N = CS^k$ are compared to those from a one-dimensional adiabatic cloud model that includes explicit pre-activation growth kinetics. Using the above base case scenario, and for $k = 0.3$, 0.5, and 0.7, the equilibrium model overestimates CDN concentrations ($[CDN]$) by 69%, 29%, and 14%, respectively, as compared to the cloud model. These $\Delta[CDN]$ values can be translated into estimates of the overprediction of globally-averaged cloud forcing using a previously published relationship between global mean cloud radiative forcing and $[CDN]$ changes. Based on this calculation, the equilibrium activation model overestimates the magnitude of the total (natural plus anthropogenic) cloud radiative forcing by 3.6, 1.8, and 0.9 Wm^{-2}, respectively, which are significant compared to the total estimated greenhouse forcing of 2.4 Wm^{-2}. Although these numbers are approximate, it is clear from their magnitude that climate models must consider activation kinetics in order to accurately predict the radiative climate forcing by clouds.

Another consequence of kinetically-limited activation is that CCN chambers that have residence times that differ from the typical growth times found in real clouds will incorrectly measure the CDN concentration. Figure 4.2 shows typical activation timescales between a fraction of a second to hundreds of seconds, whereas cloud chambers tend to have residence times between a few to a few tens of seconds. The measured CCN concentration will be either too small or too large, depending on whether the CCN instrument had a growth time that was shorter or longer than that in the actual cloud. In either case, the data will not be appropriate for use with climate models unless the discrepancy is considered. CCN measurements under conditions that mimic cloud conditions would yield data more useful for cloud radiative forcing calculations.

4.2 Supporting Calculations

4.2.1 Calculation of Timescale for Equilibrium Growth

The equilibrium timescale τ_e requires the computation of two distinct terms. The first is the rate of change of particle diameter with respect to supersaturation. The second is the rate of change of supersaturation with time.

Calculating dD_p/dS

Starting with the Kohler equation:

$$\ln(\frac{p_w(D_p)}{p^o}) = \frac{4\sigma_w M_w}{RT\rho_w D_p} - \frac{6n_s M_w}{\pi\rho_w D_p^3} \tag{4.1}$$

which can be re-written as:

$$\ln(1+S) = \frac{A}{D_p} - \frac{B}{D_p^3} \tag{4.2}$$

If equation (4.2) is differentiated implicitly, the result is:

$$\frac{dD_p}{dS} = 2 \cdot \left[\frac{4M_w}{\rho_w D_p^2}\left(\frac{9f}{\pi D_p^2} - \frac{2\sigma}{RT}\right)\right]^{-1} \tag{4.3}$$

where:

$$f = \sum_i \phi_i \nu_i X_i n_i \tag{4.4}$$

describes the number of moles of solute.

In calculating dD_p/dS, it is assumed that the surface tension of the droplet is unchanged by any solution species, that the activity coefficients are all unity, and that all the salt species are dissolved at the beginning of the calculation. For the non-organic calculations, the solute was assumed to be ammonium bisulphate.

Calculating dS/dt

From [ref Jensen & Charlson], the time rate of change of supersaturation in an adiabatically rising air parcel is given by:

$$\frac{dS}{dt} = \frac{1+S}{q_v} \cdot \frac{dq_v}{dt} - (1+S)\frac{dz}{dt}\left(\frac{L}{R_d T^2}\frac{dT}{dz} + \frac{g}{R_d T}\right) \tag{4.5}$$

For an air parcel entering the cloud base, assume that dq_v/dt is negligible relative to the second term. Assuming dT/dz is the wet adiabatic lapse rate, the equation (4.5) can be re-written:

$$\frac{dS}{dt} = -8.72 \times 10^{-4} m^{-1} \cdot u \cdot (1+S) \tag{4.6}$$

where u is the updraft velocity in m/s.

Calculating τ_e

Combining equations (4.3) and (4.6) thereby yields τ_e:

$$\tau_e = \left(\frac{1}{D_p}\frac{dD_p}{dS}\frac{dS}{dt}\right)^{-1} \tag{4.7}$$

The diameter chosen to do the calculation is the diameter of the particle at 100% RH ($S = 0$).

4.2.2 Calculation of Timescale for Condensational Growth

Using an expression for the condensational growth of a droplet (ref. Seinfeld and Pandis), the timescale for condensational growth τ_G can be estimated:

$$\frac{dD_p}{dt} = \frac{1}{D_p} \cdot \frac{\Delta S}{\frac{\rho_w R T_\infty}{4 p^o(T_\infty) D_v' M_w} + \frac{\Delta H_v \rho_w}{4 k_a' T_\infty}\left(\frac{\Delta H_v M_w}{R T_\infty} - 1\right)} \tag{4.8}$$

Tthe thermal conductivity of air is given by:

$$k_a = 10^{-3}(4.39 + 0.071T) \tag{4.9}$$

where k_a is in $\mathrm{Jm^{-1}s^{-1}}$ and T is in K. The modified thermal conductivity taking into account non-continuum effects is given by:

$$3k_a' = \frac{k_a}{1 + \frac{2k_a}{\alpha_T D_p \rho \hat{c}_p}\left(\frac{2\pi M_a}{RT_a}\right)^{1/2}} \tag{4.10}$$

The diffusivity of water vapor in air corrected for non-continuum effects is given by:

$$D_v' = \frac{\frac{0.211}{p}\left(\frac{T}{273}\right)^{1.94}}{1 + \frac{2D_v}{\alpha_c D_p}\left(\frac{2\pi M_w}{RT}\right)^{1/2}} \tag{4.11}$$

The driving force ΔS needs to be estimated. The surface supersaturation is determined by Kohler theory given in equation (4.1). The ambient supersaturation is estimated by using:

$$S_\infty = \tau_e \frac{dS}{dt} \tag{4.12}$$

By using a value of dS/dt before vapor depletion is significant, equation (4.12) should overestimate S_∞ and therefore overestimate the growth rate, which is thereby a conservative estimate since it will tend to reduce the significance of activation kinetics. The desired timescale can then be calculated using:

$$\tau_G = \left(\frac{1}{D_p}\frac{dD_p}{dt}\right)^{-1} \tag{4.13}$$

Again, the diameter at 100% RH is used for this calculation.

Chapter 5 Summary and Future Work

Witch 1: When shall we three meet again
In thunder, lightning, or in rain?
Witch 2: When the hurlyburly's done,
When the battle's lost and won.
W. S. SHAKESPEARE, *Macbeth*

When this work began, the plan for future research seemed clear and straightforward: we would build a state-of-the-art CCN spectrometer, make field measurements from aircraft, and thereby contribute to the climate community's understanding of the role of CCN in cloud properties and therefore in climate-related processes. While navigating this seemingly benign and clear path, it was slowly revealed that the problem is much more complex, challenging, and interesting than a casual examination of the literature might suggest, and much remains to be explored.

Over the time that this work was performed, assumptions that were previously unchallenged were more carefully studied, not just in this study but in others as well, and often found to be insufficient for the purposes of estimating radiative climate forcing to the same level of uncertainty as, for example, greenhouse gas forcing. One such common belief was that CCN activation is accurately modelled as an equilibrium process. The relatively simple calculations performed in this study constitute the first attempt to quantitatively address this question, resulting in a picture of CCN activation where growth kinetics can be important in certain cases, generally characterized by high concentrations of large particles ($>$ 100 nm dry diameter), or low cloud updraft velocities. Subsequent modelling studies using more detailed computer simulations have brought the picture into a clearer focus, but generally support the calculations done here (Ghan et al., 1999).

The state of CCN technology also needs to be dramatically improved in order for the scientific community to obtain the needed data for climate studies. We have shown that a streamwise gradient CCN instrument similar to that of Hudson (1989), which is very attractive for aircraft operation because of its features of simultaneously measuring the entire CCN spectrum at a reasonable frequency (~1 spectrum per minute), and upon which we based our design of a new airborne CCN spectrometer, exhibits poor resolution; over the climatically important range of critical supersaturations (the inferred quantity) from 0.03 to 1%, the final droplet diameter (the measured variable) varies only by 30%. The CCN instrument constructed during the course of this study does, however, possess a number of attractive features, including minimum mass, volume, and power consumption, along with good robustness and the ability to make reasonably high frequency measurements (< 10 s per spectrum). However, the construction of a CCN instrument which makes measurements with accurate predictive capabilities for climate remains an important and as-of-yet unachieved goal.

Indeed, the concept of CCN concentration as a useful and predictive quantity is still an open question. A comparison of measured CCN concentration with that predicted from aerosol size distribution and composition measurements made during *Pelican* flights during ACE-2 deviates from the expected one-to-one relationship. This is qualitatively consistent with some previous studies. The relationship between below-cloud CCN concentration and in-cloud properties for marine stratiform clouds is also in reasonable agreement with the literature, but the high degree of variability exhibited by the data does not lead to predictions that are sufficiently accurate for climate modelling purposes. One major reason for this difficulty is the inherent variability and uncontrollability of clouds. At present, we are unable to perform in-situ closure experiments on cloud microphysics because some of the important variables are at best very difficult to measure (e.g., meteorological variables such as supersaturation ratio, 3-D velocity fields, turbulence, and chemical/microphysical variables such as particle solubility and surface active properties, and soluble gases), or perhaps even unidentified, since theoretical understanding of clouds is also an evolving field of research.

This work both contributes to the pool of knowledge relating aerosols to clouds, and perhaps just as importantly, raises more questions than it answers, or more optimistically, opens more doorways than it closes. Given that much work remains before we can confidently and quantitatively relate aerosols to their ultimate climatic effects, it appears that both types of contributions are needed for future progress.

Appendix A CCN Instrument Details

A.1 Introduction

This appendix contains a parts list, drawings, circuit diagrams, and other information required for the construction of the CCN instrument. For each instrument component, a discussion about the design and assembly is also provided.

A.2 Parts List

Table A.1 is a list of purchased components associated with the CCN instrument, with description, part number, and vendor information.

A.3 Component Descriptions

The following are descriptions and mechanical drawings for different components of the CCN instrument. An overall picture of the assembled CCN column plus OPC is presented in the assembly drawing Figure A.1.

A.3.1 Column Inlet

The inlet (Figures A.2 to A.5) serves to introduce aerosol and sheath air into the column. It also provides liquid water to the filter paper lining the column tube by use of an external peristaltic pump. The shape of the inlet was called out such that the sheath flow is smoothly and monotonically reduced from the diameter at the top of the inlet to the 0.75" diameter to match the CCN column tube. The diameter of the aerosol inlet tubing should be chosen such that the diameter of the streamline that theoretically separates the sheath from the aerosol flow (based on the ratio of sheath to aerosol flow) is the diameter of the aerosol inlet tube. Also, the aerosol inlet tube should be machined such that it has a knife edge at the end in order to minimize any secondary flow problems. It has been speculated that despite all these precautions, secondary or recirculating flow resulting from the merging of two laminar flows causes some of the particles to be transferred to the sheath flow region which

Part Description	Part Number	Vendor
Fiber-coupled laser (670 nm, 18 mW)	FBC-011	Blue Sky
Avalanche photodetector	C5460-01	Hamamatsu
Fiber optic patch cord (1 mm core diameter)	Custom	ThorLabs
Apherical lens	01 LAG 003/078	Melles Griot
Multichannel analyzer card	Trump 2K	EG&G Ortec
Temperature controllers	RHM 4000	Wavelength Electronics
Thermistors (20 kΩ)	TCS 620	Wavelength Electronics
Thermoelectric coolers	66195 1	Melcor
Resistive heaters	2HK5163R44.0L12B	Minco
CCN column insulation	93015 K66	McMaster
Tubing (0.75" OD, 0.010" wall)	-	TubeSales
Data acquisition card (AT-MIO 64E)	776911 01	National Instruments
Data acquisition card cable	182762 0R5	National Instruments
Data acquistion terminal block	776164 90	National Instruments
PC/104 computer (386SX)	PCA 6135 00B1	Advantech
Solid state memory (16 MB)	PCM 3810A	Advantech
Backplane for PC/104 computer	MBPC 641	Advantech
Enclosure for PC/104 computer	296 232A 80	Zero Enclosures
28 to 12 V DC/DC converter (150 W)	uV28 12	RO Associates
28 to 5 V DC/DC converter	VI 2W0 CY	Vicor
28 to ±12 V DC/DC converter	VI JW1 CZ	Vicor
Absolute pressure transducer (0 to 1000 torr)	P155-15A-D1A	Kavilco
Differential pressure transducer	RXLDP 1.0%	Ashcroft
Humidity transmitter	Humitter 50A	Vaisala
Crfitical Orifices	various	O'Keefe Controls
Volumetric flow controller	HC12-2LPM-D-0	Alicat Scientific
OPC amplifier op-amp	CLC426	National Semiconductor
Amplifier circuit board	CLC730013	National Semiconductor

Table A.1: Parts list for CCN instrument construction.

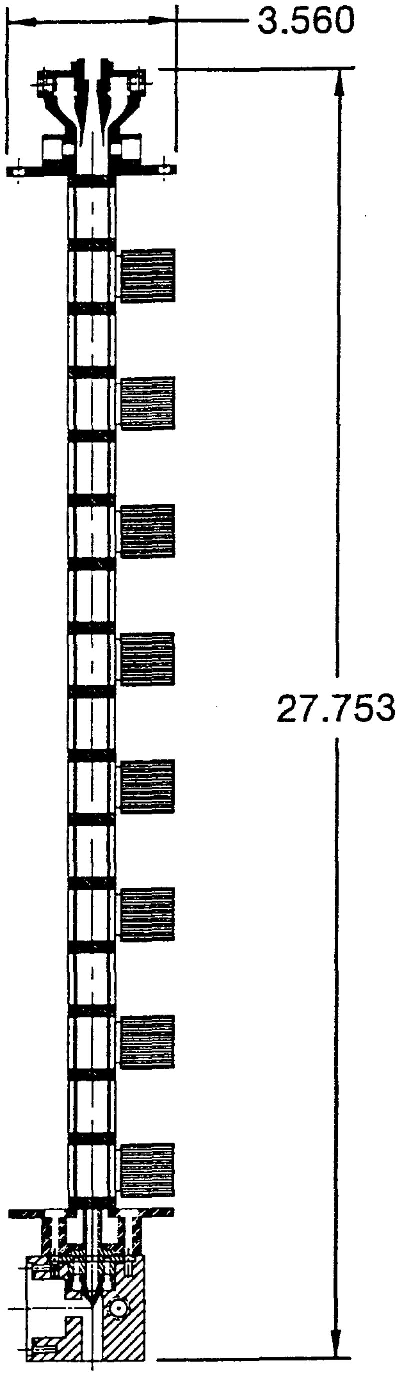

PART NAME CCNS: ASSEMBLY		DRAWN BY: Patrick Chuang Caltech
MATERIAL: N/A	DRAWING # 1 of 1	DATE 10 14 1998

Figure A.1: Assembly drawing of CCN column.

is ideally particle free. This hypothesis has not been tested, although, if true, could limit the resolution of the instrument by governing the ability of the inlet to constrain the aerosol close to the centerline of the CCN growth column.

In order to minimize secondary flow caused by the introduction of the sheath air perpendicular to the eventual direction of motion, a series of screens, attached to the inlet using the screen nut, is used. The flow straightening properties of the screen are controlled in large part by the pressure drop associated with the screens. Again, swirling caused by insufficient pressure drop in the sheath flow inlet section could cause problems further along the tube, but no attempt has been made to test this possibility.

Eight small (approx. 0.050" diameter) holes are drilled into the column tube, which exposes the lining filter paper directly to liquid water introduced via the inlet water reservoir. The choice of size and number of these holes was not based on any constraints, but rather on what seemed to be reasonable; either of these parameters could be changed if necessary and would not affect anything else.

A.3.2 CCN Column

Figures A.6 through A.8 are the drawings related to the CCN column itself. The 0.126" diameter holes reamed into the hot and cold segments are for 0.125" OD thermistor probes. The probes are made by potting the purchased thermistors (see Parts List, Table A.1) into precision thin-walled copper tubing 0.125" OD using thermally conductive epoxy (Delta Bond, available from Newark Electronics). These probes are then inserted into the reamed holes using a small amount of thermal compound for maximum thermal conductivity. The reamed holes are placed in close proximity to the resistive heaters and thermoelectric coolers (TECs) in order to simplify temperature control. It was found that if the temperature sensor was placed opposite to the heater or cooler, thermal lag resulted in oscillations in the convergence of the controller to the set point temperature.

Hot and cold segments are insulated from one another using a 0.25" thick insulat-

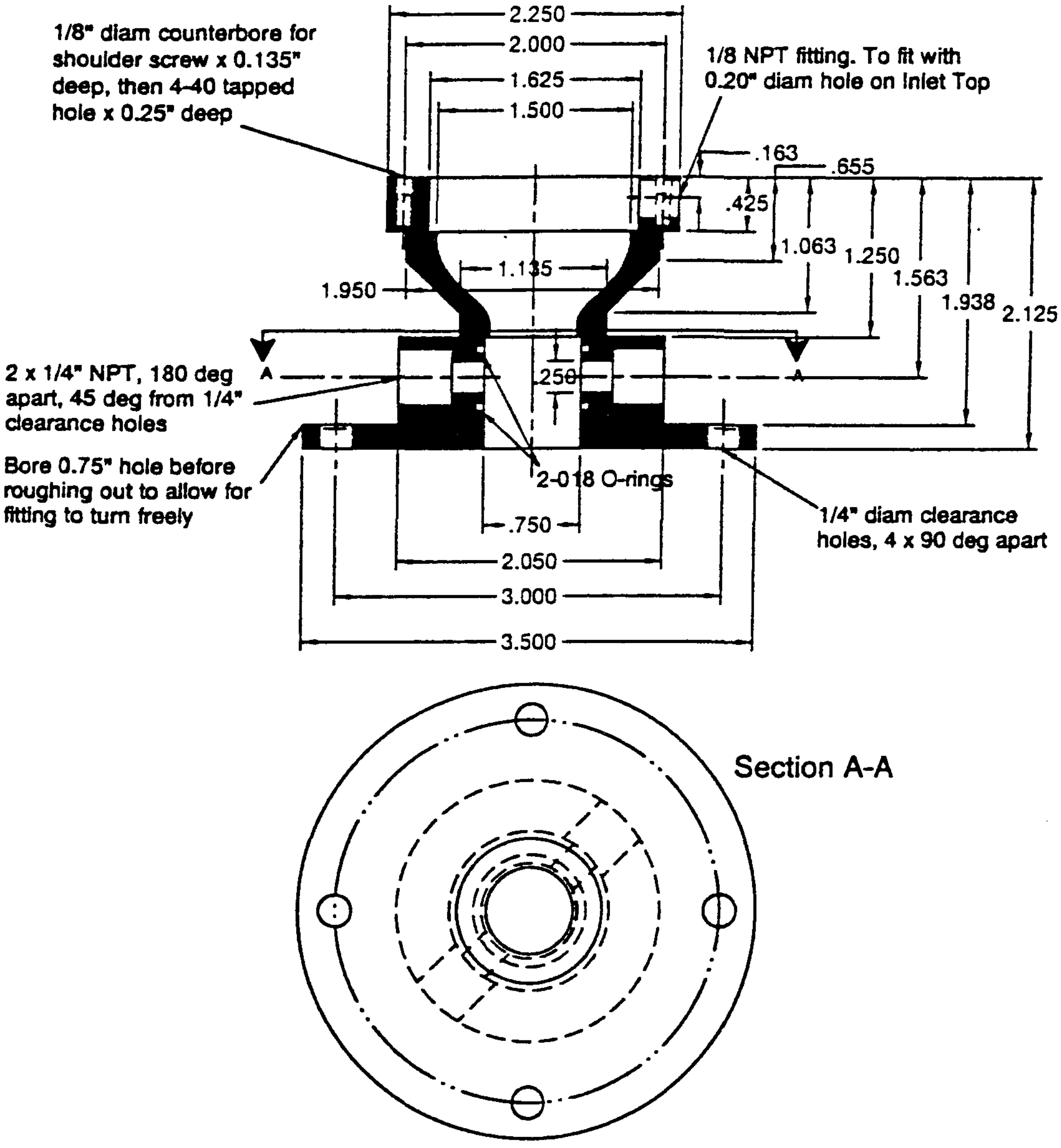

PART NAME INLET: MAIN HOUSING		DRAWN BY: Patrick Chuang Caltech
MATERIAL: AL 6061	DRAWING # 1 of 4	DATE 10 14 1998

Figure A.2: Mechanical drawing of inlet main housing.

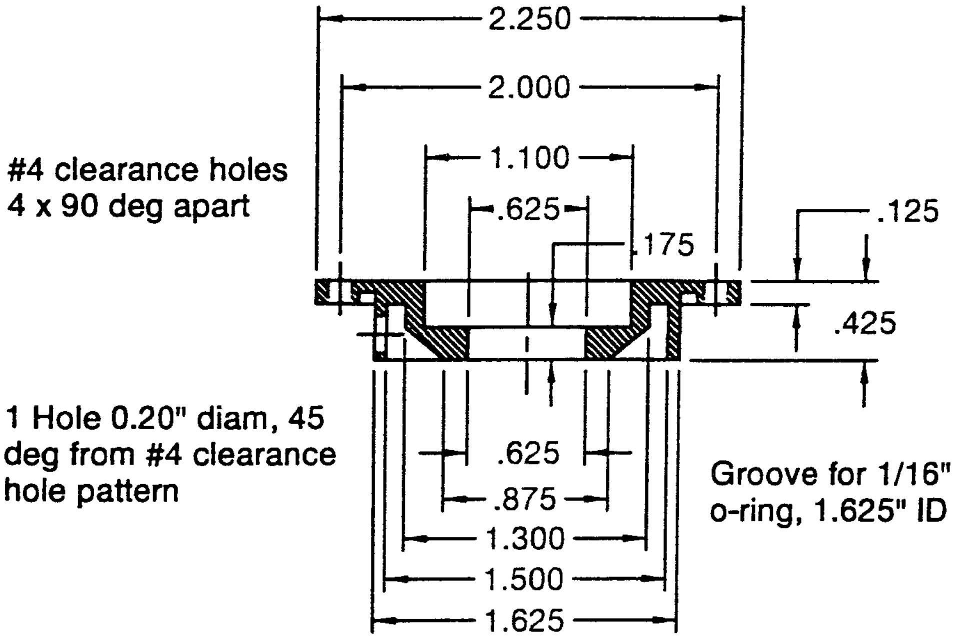

PART NAME INLET: TOP		DRAWN BY: Patrick Chuang Caltech
MATERIAL: AL 6061	DRAWING # 2 of 4	DATE 10 14 1998

Figure A.3: Mechanical drawing of inlet top.

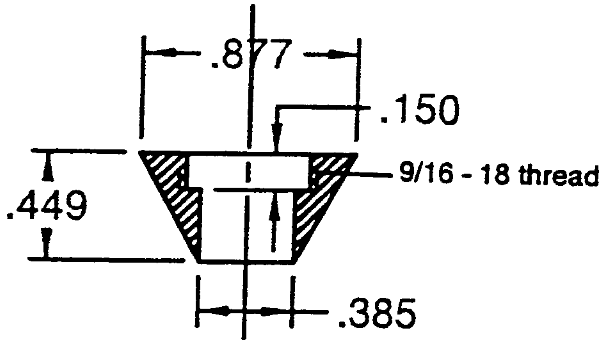

PART NAME INLET: SCREEN NUT		DRAWN BY: Patrick Chuang Caltech
MATERIAL: AL 6061	DRAWING # 3 of 4	DATE 10 14 1998

Figure A.4: Mechanical drawing of inlet screen nut.

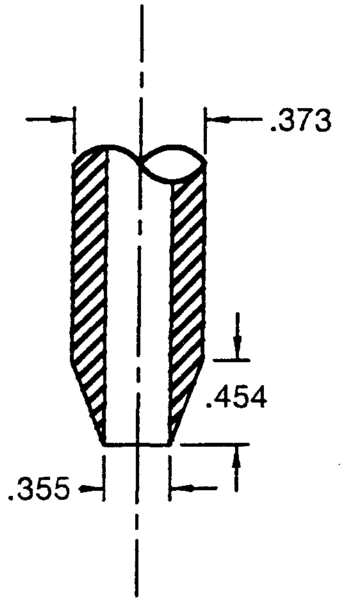

PART NAME INLET: TUBING MODIFICATION		DRAWN BY: Tim Vanreken Caltech
MATERIAL: 3/8 OD SS TUBE	DRAWING # 4 of 4	DATE 10 14 1998

Figure A.5: Mechanical drawing of inlet tube modification.

ing material (Pyropel, available from McMaster, Part #93015K76). The insulation is cut into 1.125" squares, and then holes 0.75" diameter are punched into them. The resistive heaters are fastened to the hot segment blocks using self-adhering tape (available from Minco or McMaster). For the cold segments, the heat sinks were used because it was found that without them, the TECs went into thermal runaway. This occurs when the hot side of the TEC is not sufficiently cooled, resulting in conduction of heat back to the cold side, increasing its thermal load, leading to more current being supplied to the TEC, causing more heating on the hot side, etc. In order to further dissipate heat from the TECs, a small fan is mounted at the bottom of the column blowing upwards, and a shimstock duct is used to constrain this air flow over the heat sinks. This cooling results in the TECs running more efficiently.

To assemble the column elements, the thermistor probes are inserted into the reamed holes, and the heaters and TECs (with heat sinks) are attached to each segment block. Thermal compound is used on both sides of the TECs, although no thermal compound was deemed necessary for the resistive heaters. Alternating hot and cold segment blocks slide onto the CCN column tube, again using a thin layer of thermal compound to maximize thermal conductivity, with an insulating square used between each one. Once all the segment blocks are in place, the entire column is insulated using strips of Pyropel along the three sides without heat sinks, and using small squares of insulation for the hot segments in between heat sinks. The insulation is then fixed in place using cable ties.

Lining the CCN column tube with filter paper can be a little tricky. The filter paper used is Whatman 3Chr. Thicker filter paper was tried, but it did not have enough flexibility to fit into the tubing without folding. Thinner paper would result in an increased frequency of regenerating the water in the column because the paper would dry out more quickly. To properly line the column, a strip of filter paper much longer than necessary (approximately 6 to 12" more), and with a width somewhat larger than one circumference of the ID of the tube, is cut. A solid, clean rod (typically 0.5" OD) is used to slowly work the filter paper into a circular shape. The paper is then inserted slowly into the tubing without wrinkling. It is likely necessary to twist the paper into a smaller diameter to get it to fit. Once the paper lines the entire tube length, it must be uncoiled such that the seams of the paper are straight. Finally, the paper should be manipulated such that it tightly lines the inside of the tube. Wetting of the tubing will also help bring the paper in contact with the tube wall. The paper should be inspected on a frequent basis because it has a tendency to come off of the tubing wall. If this occurs, and cannot be fixed by gently rolling a rod over that section, the paper should be replaced. Finally, a small aluminum split ring is used to hold the paper in place at the bottom of the column. It holds the paper after the air flow has entered the outlet skimmer and therefore does not affect the growth of CCN in the column. It is roughly 3/8" high, thin (0.020" wall thickness), and around 0.70" diameter before it is split and a small amount of material removed.

A.3.3 CCN Outlet

The CCN instrument outlet (Figures A.9 to A.12) focuses the combined aerosol and sheath flows through a small nozzle in order to size and count grown droplets in the OPC. It also has a water reservoir to catch any liquid water running down the CCN column tube. The skimmer has a sharp edge to minimize flow disturbances. It sits off the wall, however, in order to prevent any large beads of water from entering the OPC, which can cause serious problems, typically by dripping on to the front receiving lens. The nozzle was designed with a 15° half angle. It was found that nozzle diameters much smaller than 0.040" seemed to cause droplet impaction, so 0.040" seems to be close to the lower limit for the nozzle diameter. It might be possible to reduce the nozzle size (which would narrow the spread of aerosol in the view volume of the OPC) by reducing the nozzle converging angle. If the angle is reduced by too much, however, the time lag between the end of the column and sizing at the OPC might result in a shift in droplet size due to evaporation, although this shouldn't be a problem as the surrounding air should be close to saturation. The nozzle was designed such that it can be easily replaced without substantial additional machining.

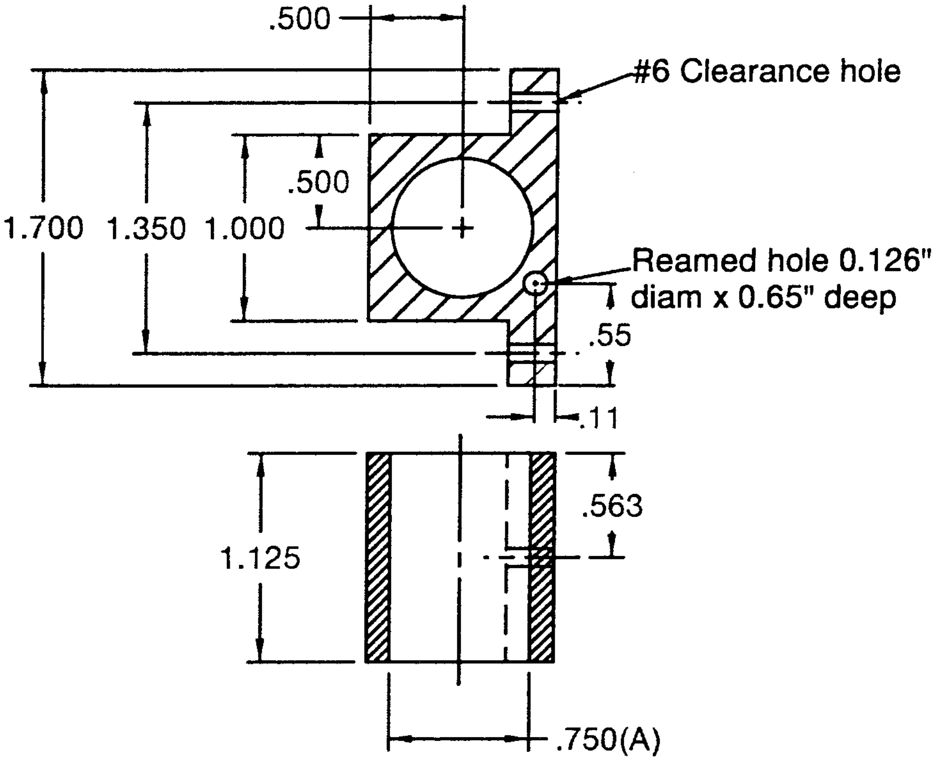

(A) For close sliding fit of 3/4" OD tubing (provided)

PART NAME CCNS COLUMN: COLD SEGMENT		DRAWN BY: Patrick Chuang Caltech
MATERIAL: AL 6061	DRAWING # 1 of 3	DATE 10 14 1998

Figure A.6: Mechanical drawing of CCN column cold segment.

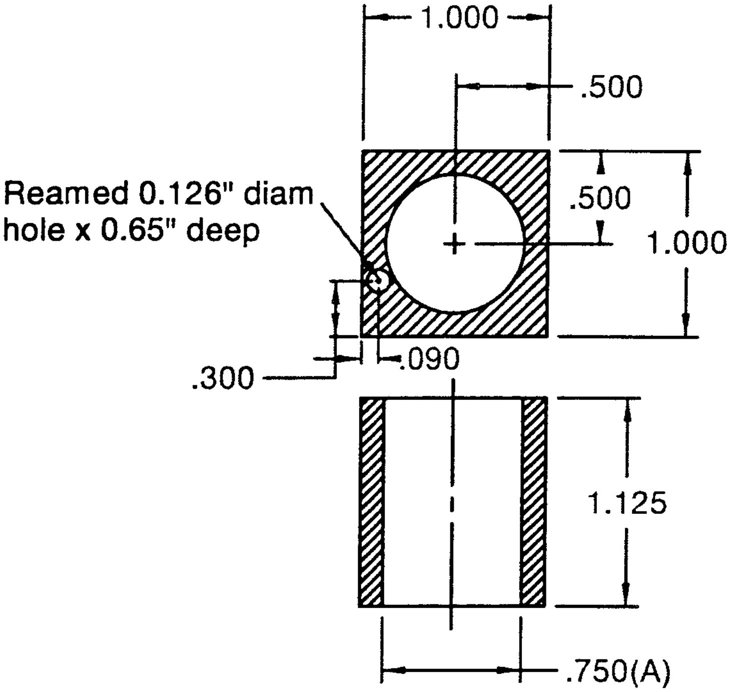

(A) For close sliding fit of
0.75" OD tubing (provided)

PART NAME CCNS COLUMN: HOT SEGMENT		DRAWN BY: Patrick Chuang Caltech
MATERIAL: AL 6061	DRAWING # 2 of 3	DATE 10 14 1998

Figure A.7: Mechanical drawing of CCN column hot segment.

1. Cut heat sink so dimension along fins is approx. 1.15" (A).
2. Cut heat sink symetrically so dimension perpendicular to fins terminates on the outer edge of a fin and is larger than 1.70" (B).
3. Mill bottom side of heat sinks flat to within 0.002"
4. Drill and tap 6-32 holes 1.350" apart (to fit already made Cold Segments) as deep as possible.

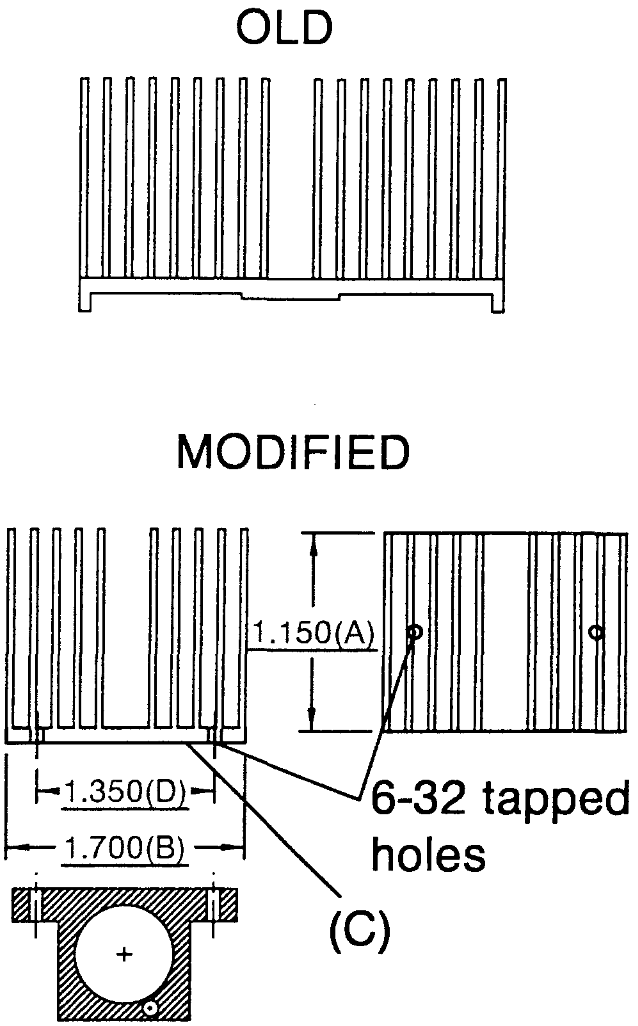

PART NAME CCNS COLUMN: HEAT SINK MODIFICATION		DRAWN BY: Patrick Chuang Caltech
MATERIAL: AL 6061	DRAWING # 3 of 3	DATE 10 14 1998

Figure A.8: Mechanical drawing of CCN column heat sink modification.

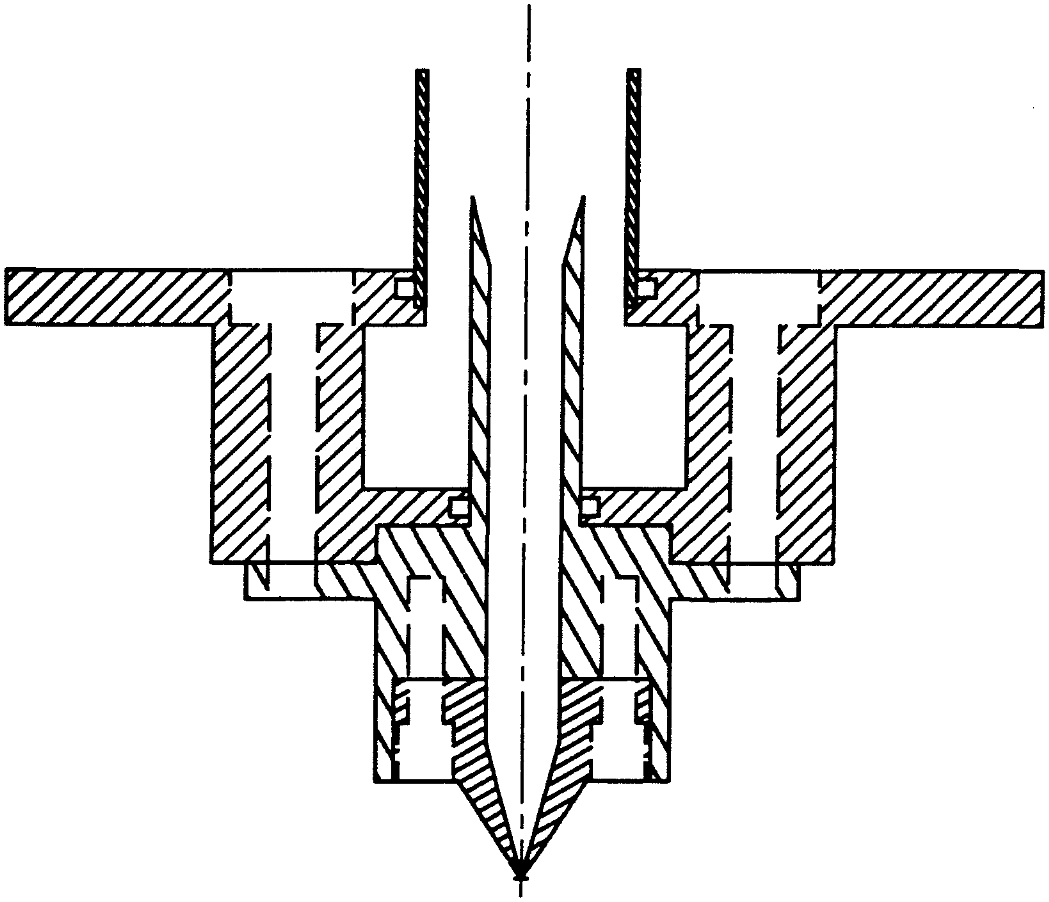

PART NAME OUTLET: ASSEMBLY		DRAWN BY: Patrick Chuang Caltech
	DRAWING # 1 of 4	DATE 10 14 1998

Figure A.9: Assembly drawing of outlet.

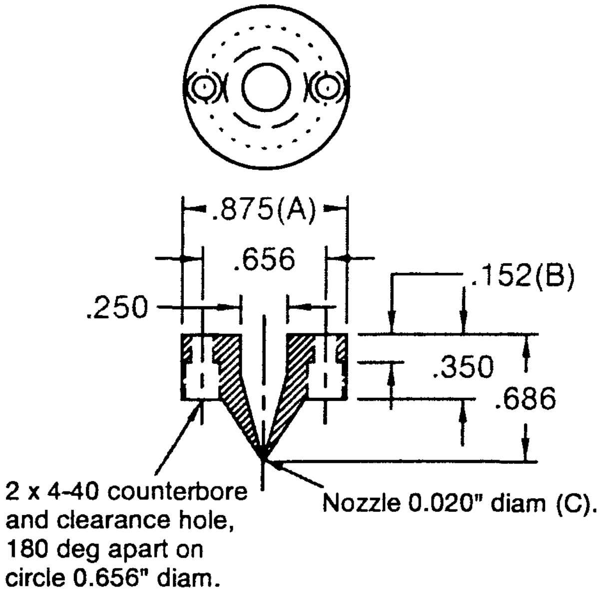

(A) For smooth sliding fit into Outlet Skimmer. Centering of the nozzle on the axis is critical, so a tight fit is important, but not so tight that the piece can't be removed.

(B) This dimension is somewhat arbitrary. If it needs to be smaller to accommodate the 4-40 counterbore that is fine.

(C) Nozzle should be machined to a fairly sharp finish, but dull enough to withstand small accidental bumps without being damaged. Would like the inner surface to be as smooth as reasonably possible, i.e. no sudden steps.

PART NAME OUTLET: NOZZLE		DRAWN BY: Patrick Chuang Caltech
MATERIAL: SS 316	DRAWING # 2 of 4	DATE 10 14 1998

Figure A.10: Mechanical drawing of outlet nozzle.

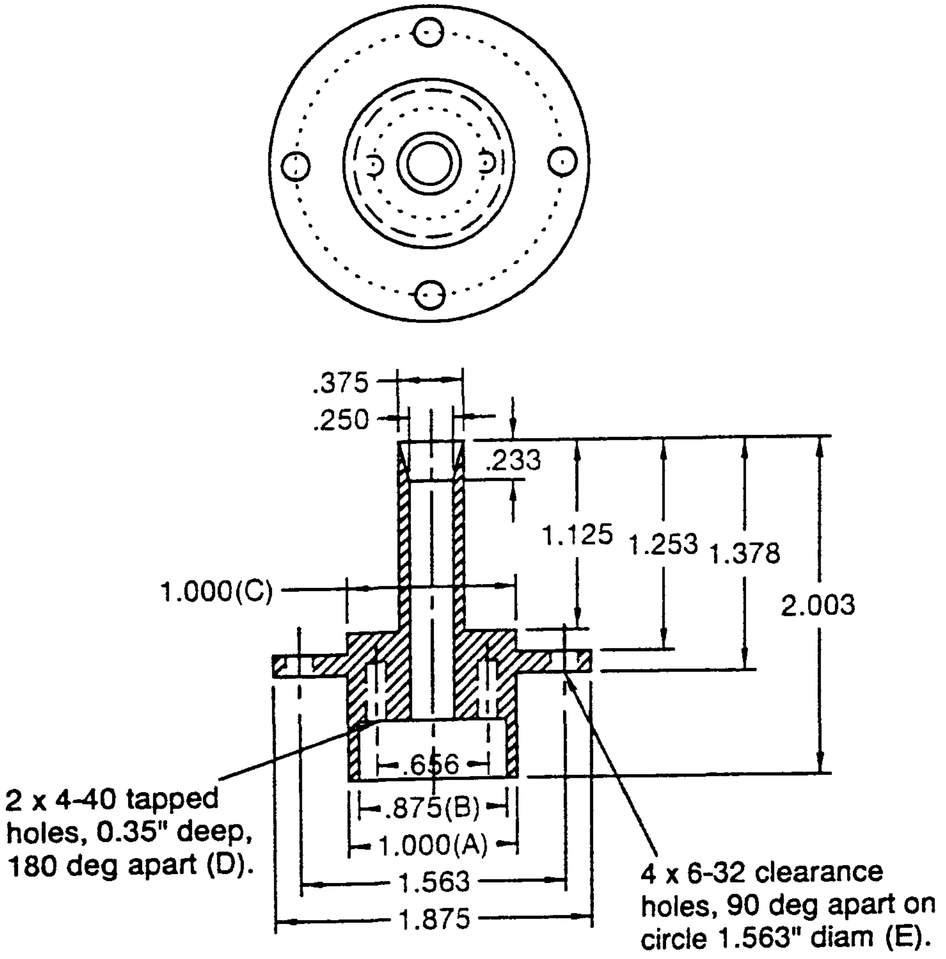

(A) For smooth sliding fit into OPC Mounting Block (provided). See Note (B) of Outlet Nozzle.

(B) For smooth sliding fit of Outlet Orifice. See Note (B) of Outlet Nozzle.

(C) For smooth sliding fit of Outlet Flange

(D) To fit with Outlet Nozzle

(E) To fit with OPC Mounting Block (will be provided).

PART NAME OUTLET: SKIMMER		DRAWN BY: Patrick Chuang Caltech
MATERIAL: SS 316	DRAWING # 3 of 4	DATE 10 14 1998

Figure A.11: Mechanical drawing of outlet skimmer.

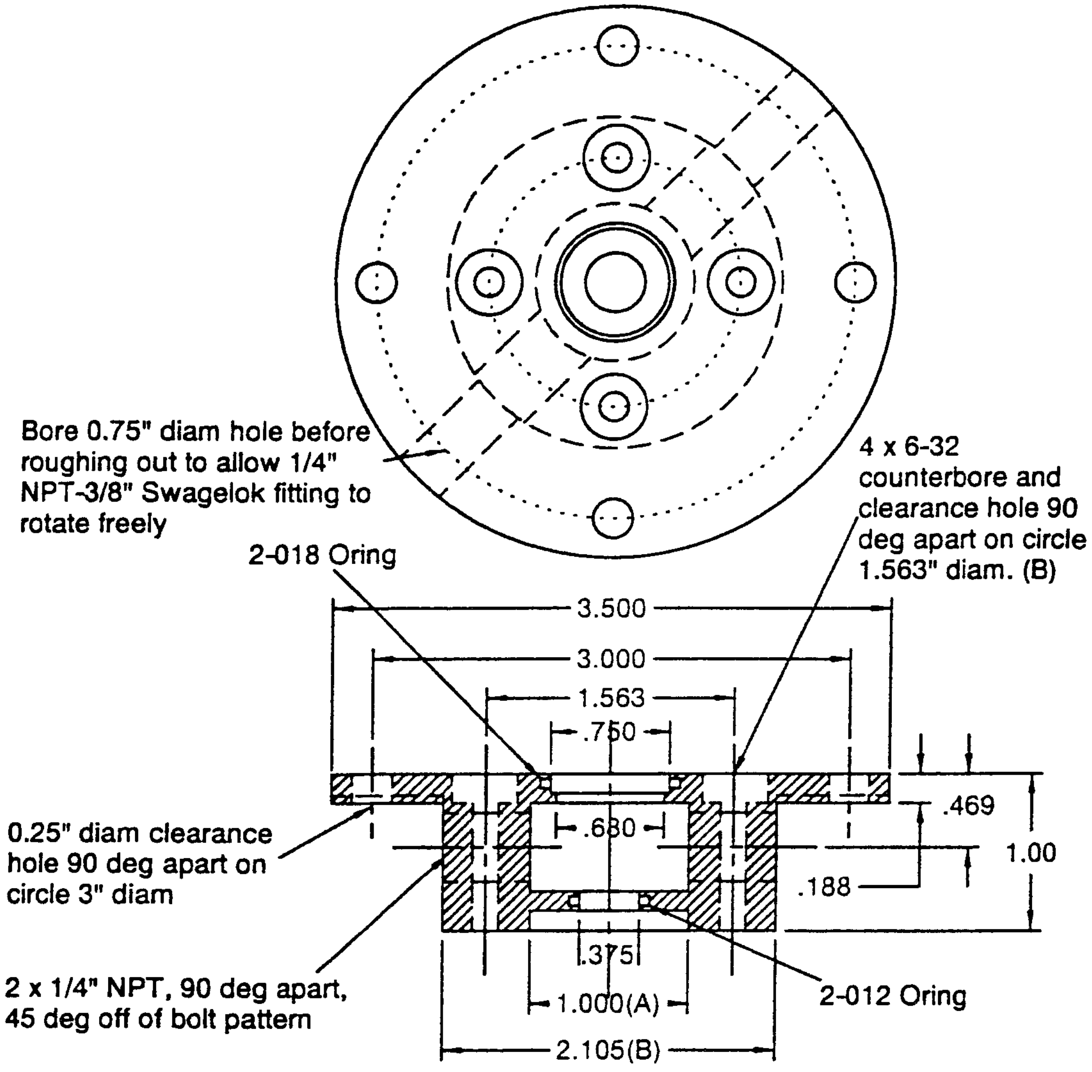

(A) For smooth sliding fit with Outlet Skimmer

(B) To fit into OPC Mounting Block, provided.

PART NAME OUTLET: FLANGE		DRAWN BY: Patrick Chuang Caltech
MATERIAL: AL 6061	DRAWING # 4 of 4	DATE 10 14 1998

Figure A.12: Mechanical drawing of outlet flange.

A.3.4 OPC Mounting Block

The OPC mounting block (Figures A.13 to A.17) was designed for minimum volume and weight, while robustly mounting all the components (transmitter, receiver, beam dump, nozzle) with high precision and repeatability. All OPC parts should be carefully machined such that their mating is smooth but without slop. Such tight precision means that parts can easily get jammed if they are not put in or pulled out straight, especially before they are anodized. A very thin coating of vacuum grease should be used in order to help prevent this from occurring. All pieces should be provided in order to properly fit them to the mounting block. The inside surface of the OPC mounting block in the vicinity of the scattering volume is roughened slightly before anodizing in order to minimize spurious light entering the receiver.

A.3.5 OPC Transmitter

The newly designed transmitter (Figures A.18 to A.22) incorporates a new laser (Blue Sky FBC-011) which provides more power (18 mW), and a cleaner beam (due to the fact that it is fiber-coupled) than the previous laser. With the old laser, spurious light resulted in significant DC noise in the detector, which necessitated the addition of a spatial filter (one focusing lens, a pinhole positioned at the beam waist, and a second recollimating lens), which was very difficult to machine and align properly. The new transmitter is much simpler. The laser emerges from the laser collimated (0.7 mm spot size) with little spurious light. The beam is then transformed using a cylindrical optic such that it is wider (4 mm) in the dimension perpendicular to the aerosol stream, but no thicker (remains 0.7 mm in the direction of the flow) at the view volume point, with a low divergence (approx. 2°). This minimizes coincidence errors, i.e. the chance that two droplets are present in the view volume simultaneously while maximizing the homogeneity of the beam with respect to droplets passing through the beam along slightly different streamlines. Spurious light caused by the cylindrical optic is reduced by the use of baffles. Note that there no adjustment in the machined pieces; all the pieces are aligned by carefully machining the parts so that they have

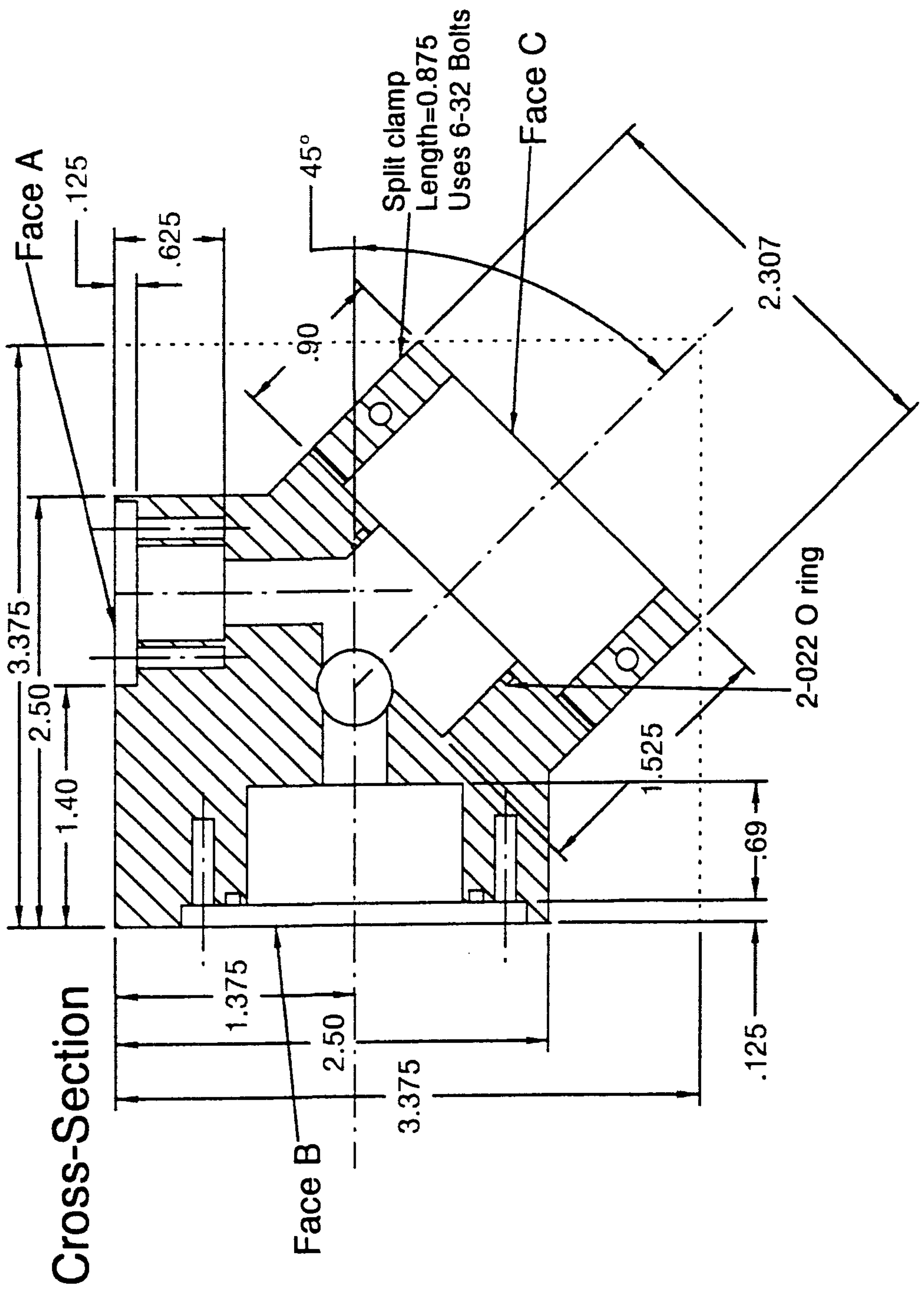

PART NAME OPC MOUNTING BLOCK: CROSS SECTION		DRAWN BY: Patrick Chuang and Tim Vanreken
MATERIAL: AL 6061	DRAWING # 1 of 5	DATE 12 02 1998

Figure A.13: Mechanical drawing of OPC mounting block, cross-section view.

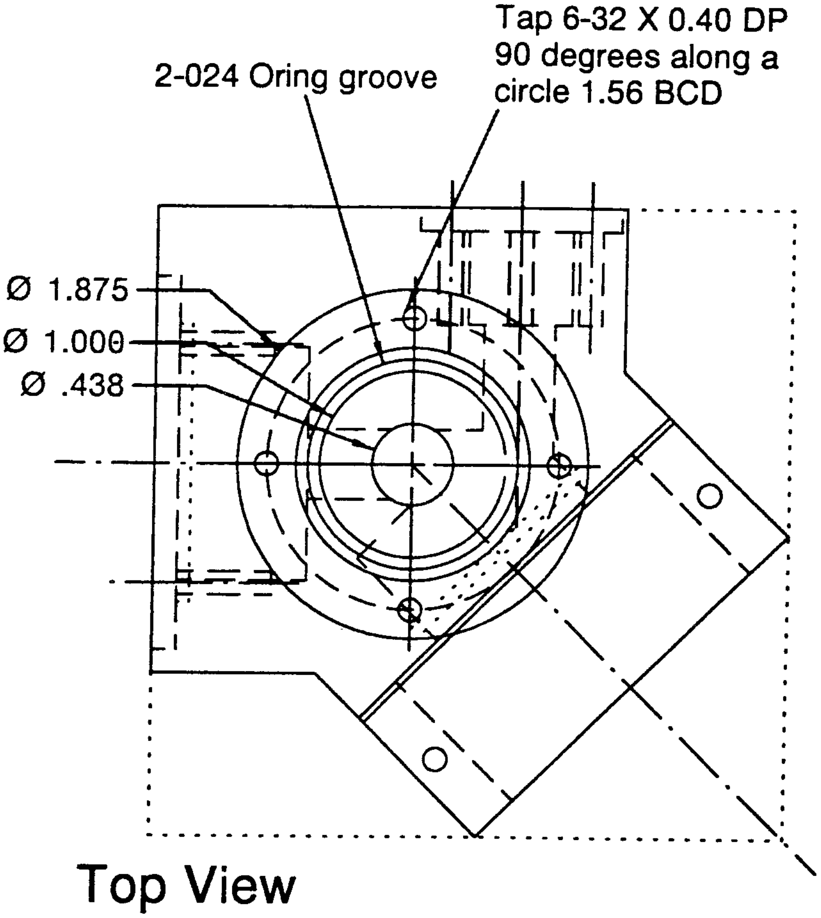

PART NAME OPC MOUNTING BLOCK: TOP VIEW		DRAWN BY: Patrick Chuang and Tim Vanreken
MATERIAL: AL 6061	DRAWING # 2 of 5	DATE 12 02 1998

Figure A.14: Mechanical drawing of OPC mounting block, top view.

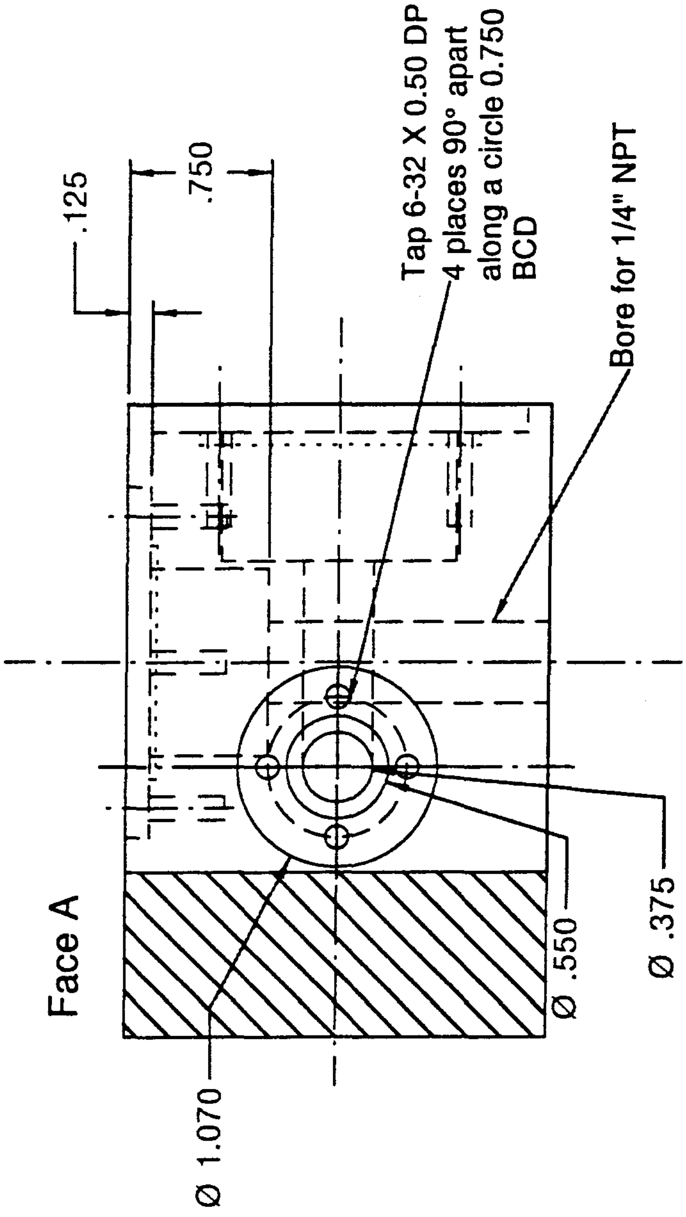

PART NAME OPC MOUNTING BLOCK: FACE A		DRAWN BY: Patrick Chuang and Tim Vanreken
MATERIAL: AL 6061	DRAWING # 3 of 5	DATE 12 02 1998

Figure A.15: Mechanical drawing of OPC mounting block, Face A (beam dump view).

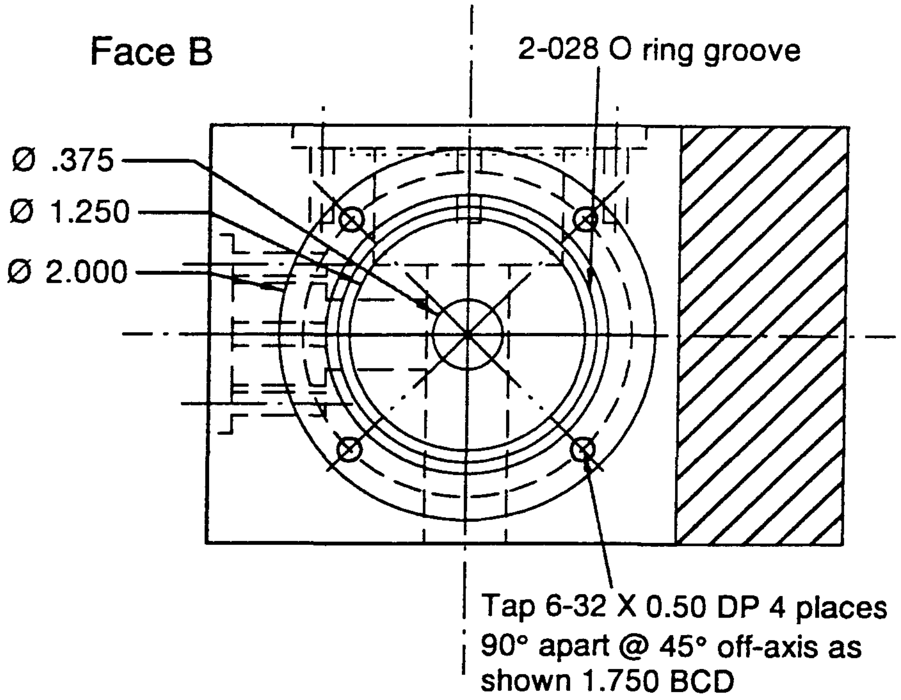

PART NAME OPC MOUNTING BLOCK: FACE B		DRAWN BY: Patrick Chuang and Tim Vanreken
MATERIAL: AL 6061	DRAWING # 4 of 5	DATE 12 02 1998

Figure A.16: Mechanical drawing of OPC mounting block, Face B (transmitter view).

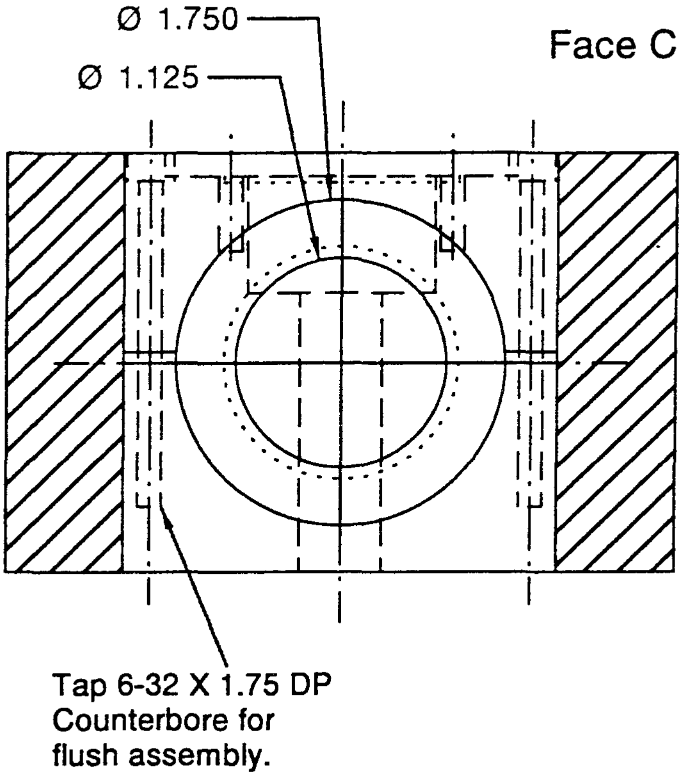

PART NAME OPC MOUNTING BLOCK: FACE C		DRAWN BY: Patrick Chuang and Tim Vanreken
MATERIAL: AL 6061	DRAWING # 5 of 5	DATE 12 02 1998

Figure A.17: Mechanical drawing of OPC mounting block, Face C (receiver view).

nearly identical axes of symmetry and close sliding fits.

The laser head is held in place in the cylindrical optic holder using a crush fit; a 45° angle notch is cut into the ring which, when tightened, squeezes the O-ring tightly against the laser barrel. Axial location of the laser head is not critical, as the output is collimated. This assembly (laser head, crush fit ring, cylindrical optic housing) is then inserted in to the transmitter housing. Alignment is achieved by use of a pin which slides into the pin alignment holes in all three pieces, and is then removed once the assembly is fastened together properly. The pin is positioned such that it is at the top of the transmitter when the transmitter is mounted into the OPC mounting block.

In order to equalize pressure in the transmitter, holes are drilled into it. This prevents a case where the transmitter was assembled at atmospheric pressure, and low pressures achieved during flight result in a large force on the cylindrical optic because of an imbalance in pressure. These holes fix both sides of the optic at ambient pressure. The window at the end of the transmitter is used to isolate the optics from the possibly harsh high-humidity environment of the OPC, and also to provide a high quality seal for the CCN instrument. In event that the CCN instrument is operated at a low, constant pressure, the window is forced onto the O-ring by the (larger) ambient pressure, tending to make an improved seal. The teflon retaining ring is used to prevent scratching of the window by the retaining ring. A long thread (0.85") was provided in the transmitter housing so that optical components could be added in the future to further condition the beam, if desired.

A.3.6 OPC Receiver

The OPC Receiver (Figures A.23 to A.29) uses two identical aspherical lenses to collect, collimate, and re-focus the light onto a fiber optical cable (1 mm core diameter), which then transmits the light to the APD photodetector. It is held onto the mounting block using a split clamp arrangement. The front asphere is held in place using a black anodized nut. Similarly to the OPC mounting block cavity, this nut is rough-

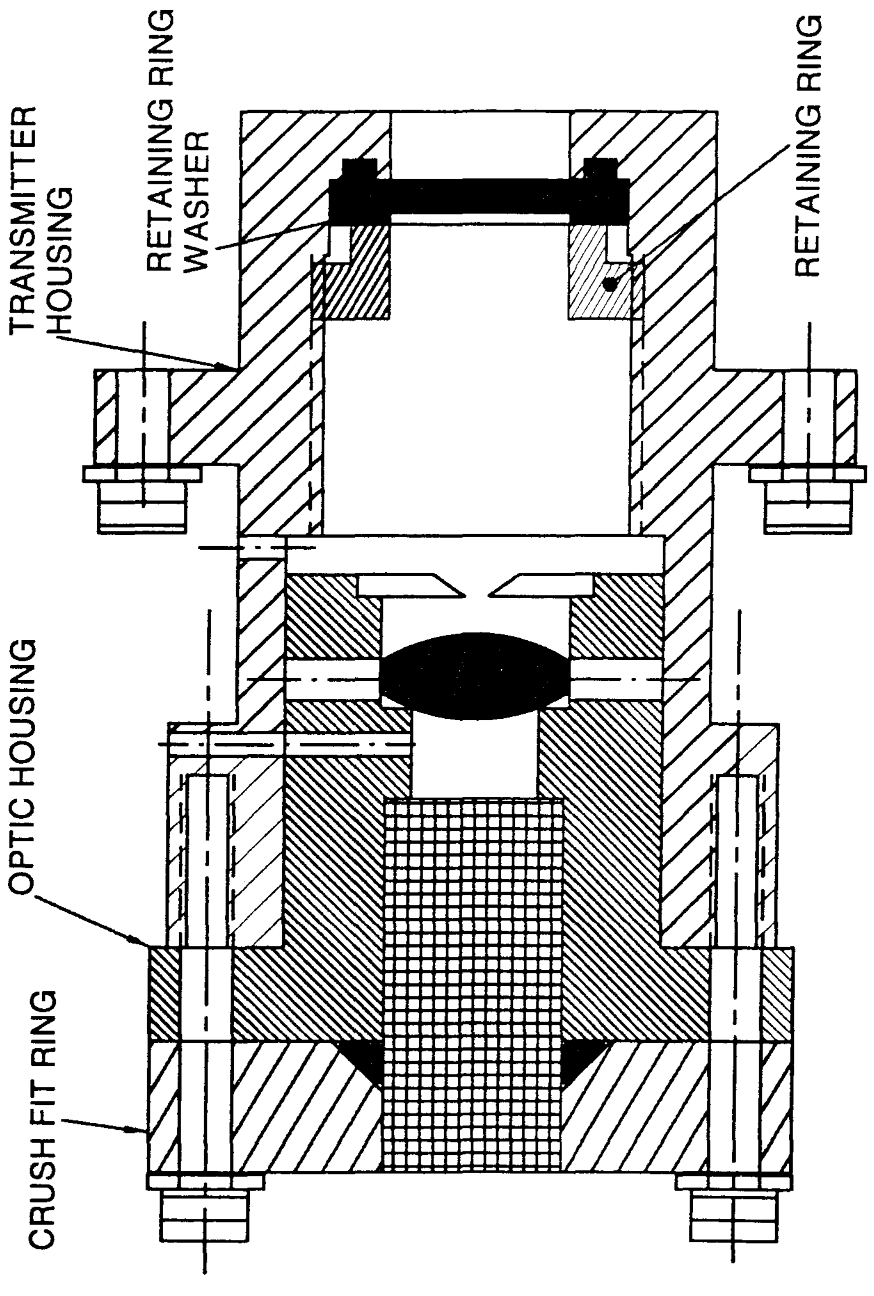

PART NAME OPC TRANSMITTER: ASSEMBLY		DRAWN BY: Patrick Chuang Caltech
	DRAWING # 1 of 5	DATE 11 24 1998

Figure A.18: Assembly drawing of OPC transmitter.

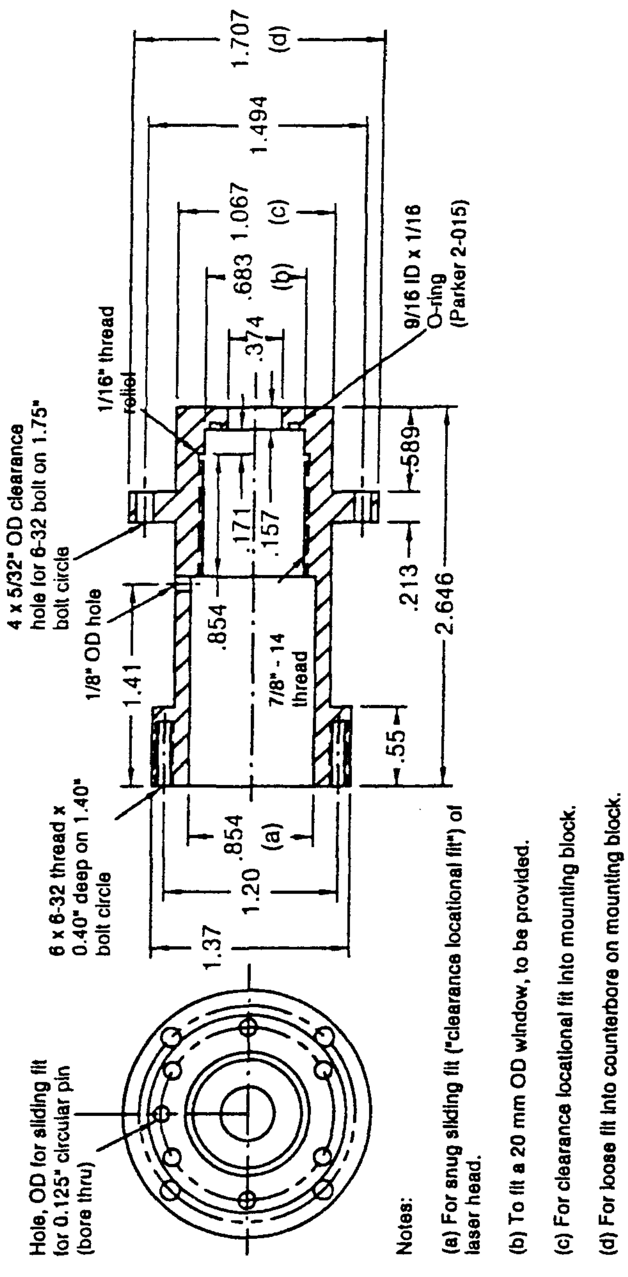

Notes:

(a) For snug sliding fit ("clearance locational fit") of laser head.

(b) To fit a 20 mm OD window, to be provided.

(c) For clearance locational fit into mounting block.

(d) For loose fit into counterbore on mounting block.

PART NAME TRANSMITTER: HOUSING		DRAWN BY: Patrick Chuang Caltech
MATERIAL: AL 6061	DRAWING # 2 of 5	DATE 11 24 1998

Figure A.19: Mechanical drawing of OPC transmitter housing.

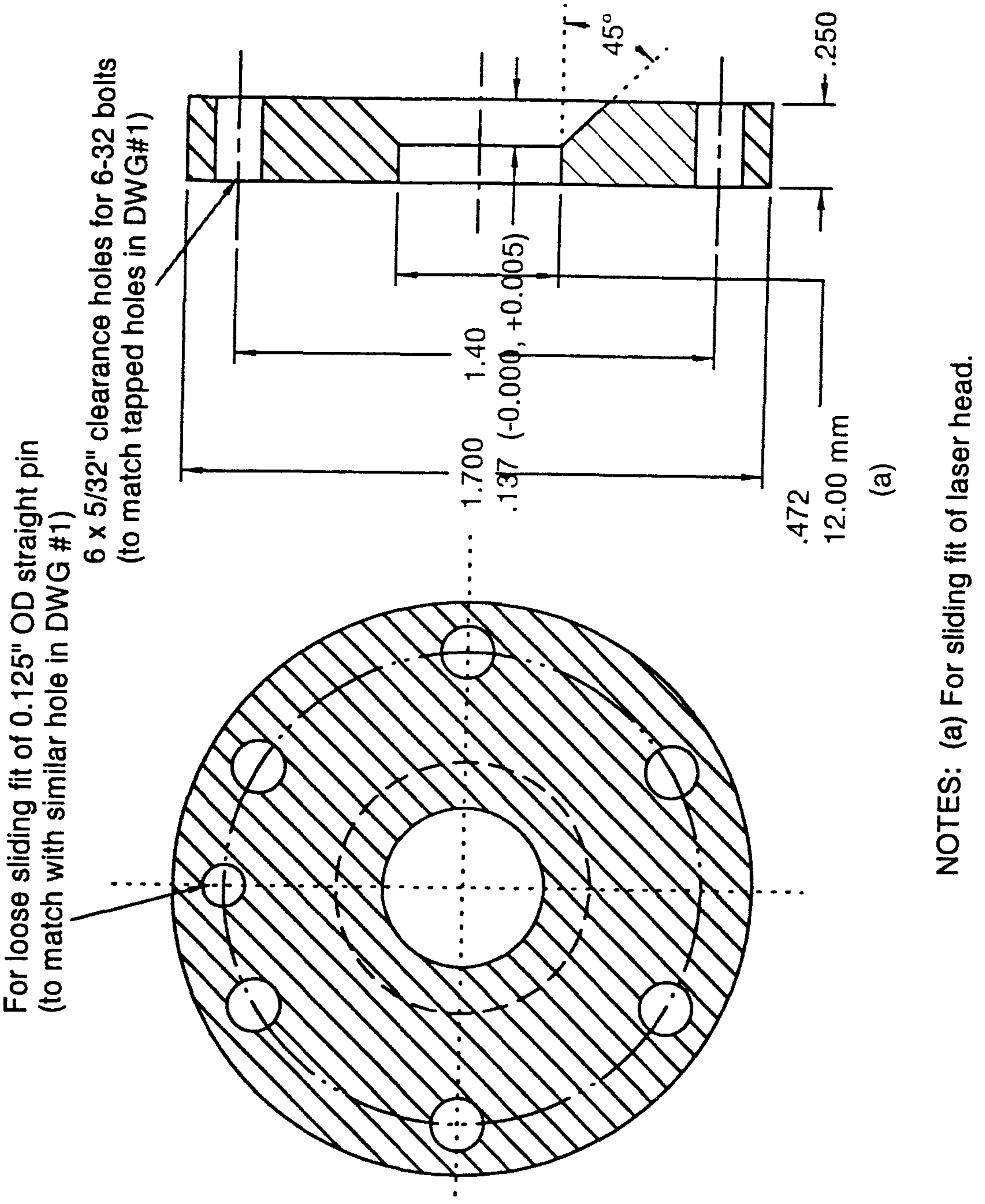

PART NAME TRANSMITTER: CRUSH FIT RING		DRAWN BY: Patrick Chuang Caltech
MATERIAL: AL 6061	DRAWING # 3 of 5	DATE 11 24 1998

Figure A.20: Mechanical drawing of OPC transmitter crush fit ring.

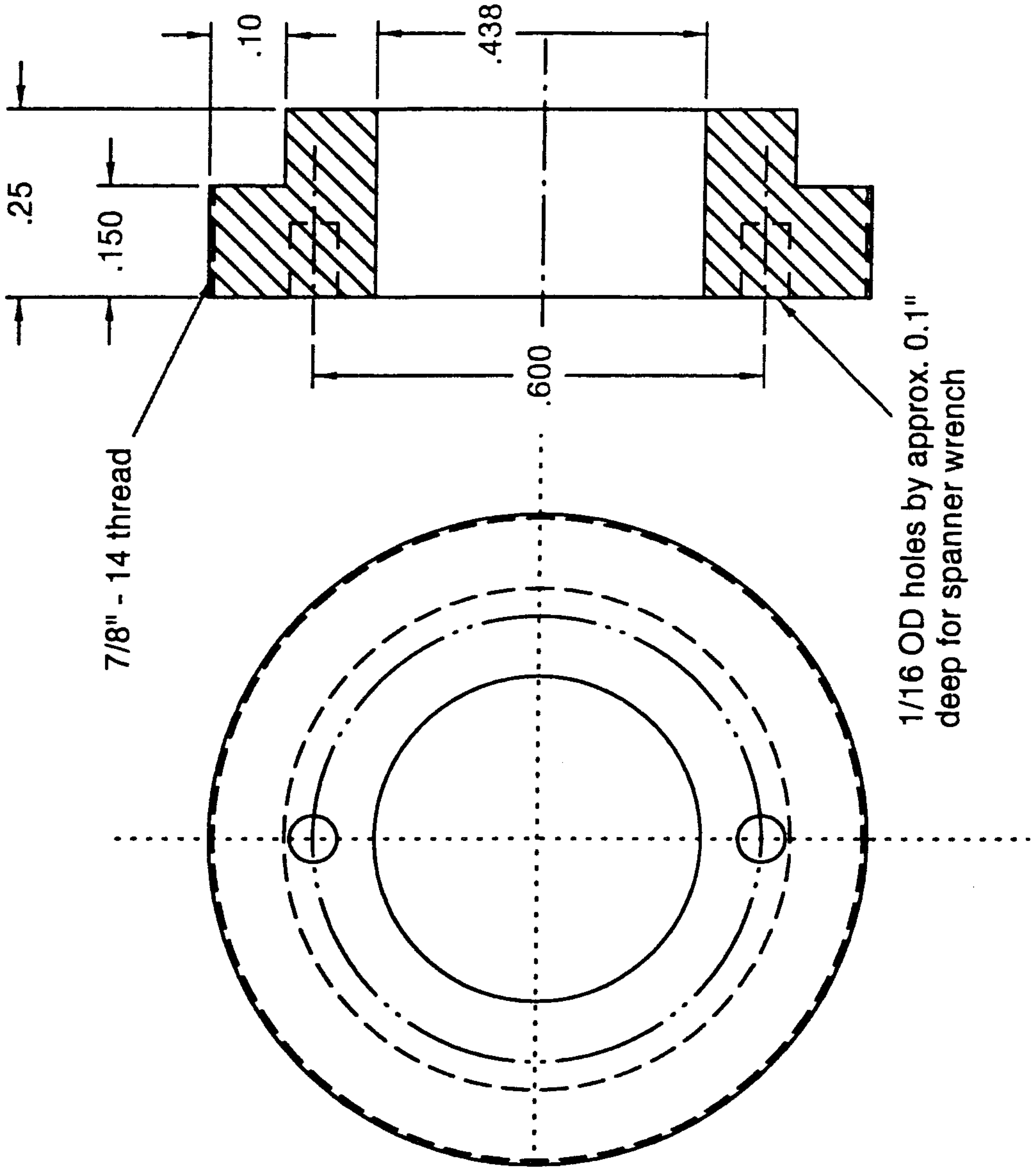

PART NAME TRANSMITTER: WINDOW RETAINING RING		DRAWN BY: Patrick Chuang Caltech
MATERIAL: AL 6061	DRAWING # 4 of 5	DATE 11 24 1998

Figure A.21: Mechanical drawing of transmitter window retaining ring.

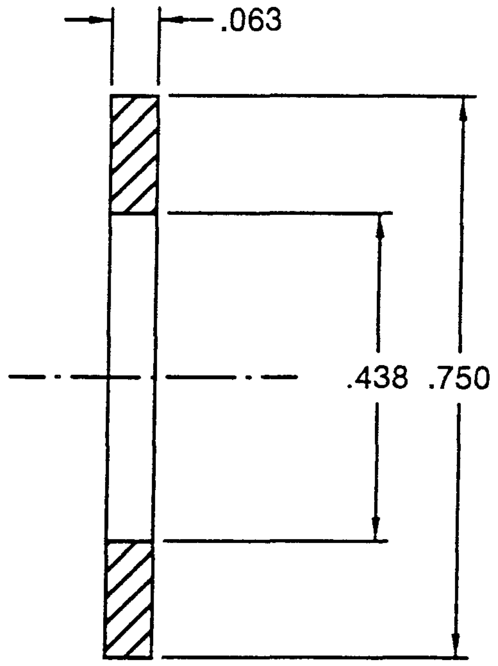

PART NAME TRANSMITTER: WINDOW WASHER		DRAWN BY: Patrick Chuang Caltech
MATERIAL: TEFLON	DRAWING # 5 of 5	DATE 11 24 1998

Figure A.22: Mechanical drawing of transmitter window washer.

ened slightly before anodizing to minimize spurious light in the cavity. The receiver rear housing holds the receiver re-focusing lens, which has axial adjustment. The lens must be adjusted in order to maximize the amount of light that is transmitted to the fiber optic cable, which attaches to the receiver using an SMA style fitting. The SMA receptacle can be purchased from Newark, and machined such that it is press-fit into the SMA flange. Once the lens is in place, it should be fixed using (removable) epoxy, preferably one that will break cleanly from the threads when sufficient force is applied.

The receiver also needs to be properly positioned axially when inserted into the OPC mounting block. This is found by changing the distance of the receiver from the view volume until the signal for monodisperse droplets is maximum. It has been my experience that the signal is not very sensitive to changes in the receiver position.

A.3.7 Beam Dump

The beam dump (Figures A.30 and A.31) is used to capture the unscattered beam. This is accomplished by reflecting the beam using a mirror mounted at the end of the Wood's Horn beam dump at a 45° angle. The reflected beam then enters the beam dump which is curved, painted black, and tapered to a seal at the end. This is a very effective way to eliminate the unwanted light. The Wood's Horn is attached to the OPC mounting block using a split clamp arrangement. Once in place (aligned such that the mirror is rotated to properly reflect the unscattered beam), the Wood's Horn does not need to be re-aligned as removing the beam dump requires removing only those bolts that fasten the split clamp to the mounting block. The mirror is attached to the end of the tubing using RTV.

A.4 Electrical Drawings

A.4.1 Wiring Diagram

Figure A.32 is a wiring diagram for the CCN instrument.

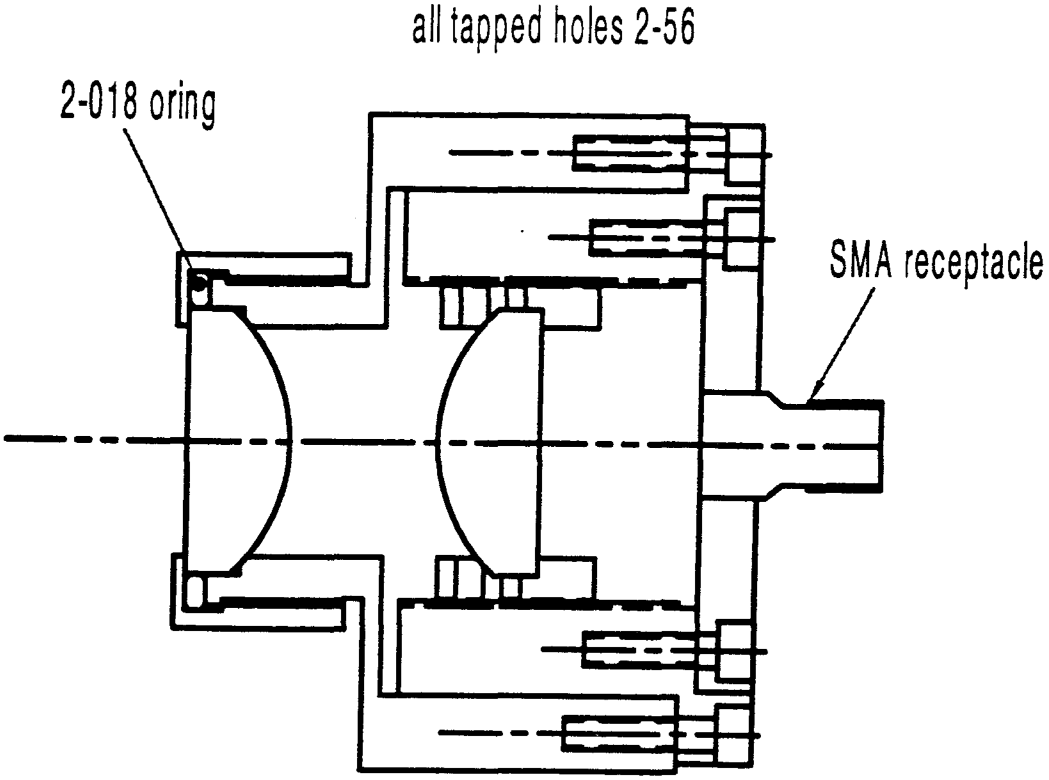

PART NAME RECEIVER: ASSEMBLY		DRAWN BY: Jim Smith Caltech
MATERIAL: AL 6061	DRAWING # 1 of 7	DATE SEP 1996

Figure A.23: Assembly drawing of OPC receiver.

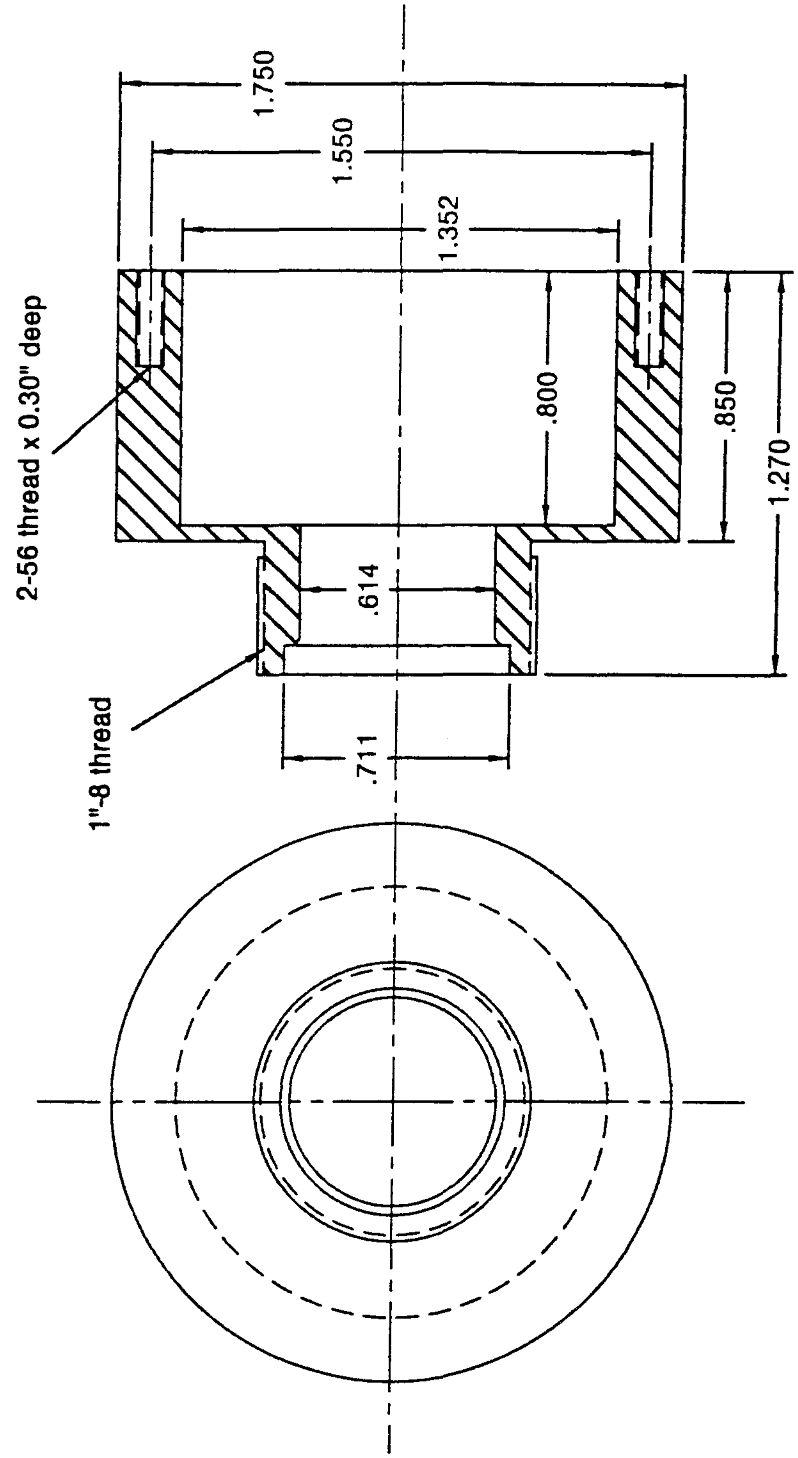

PART NAME RECEIVER: FRONT HOUSING		DRAWN BY: Jim Smith Caltech
MATERIAL: AL 6061	DRAWING # 2 of 7	DATE SEP 1996

Figure A.24: Mechanical drawing of receiver front housing.

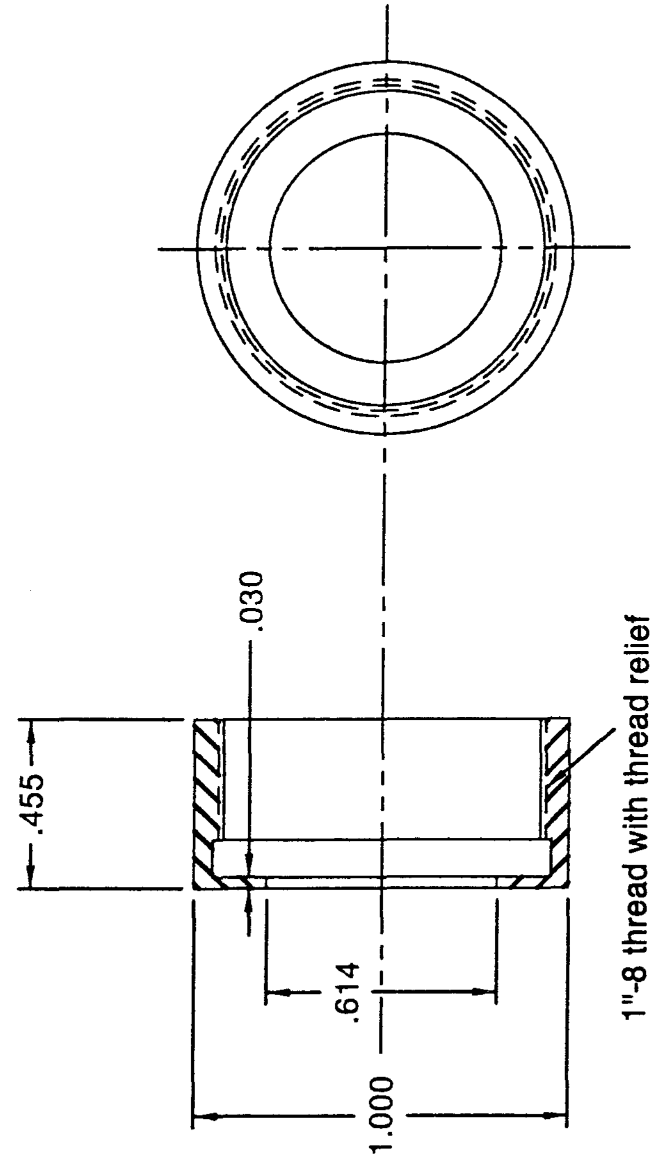

PART NAME RECEIVER: FRONT LENS NUT		DRAWN BY: Jim Smith Caltech
MATERIAL: AL 6061	DRAWING # 3 of 7	DATE SEP 1998

Figure A.25: Mechanical drawing of receiver front lens nut.

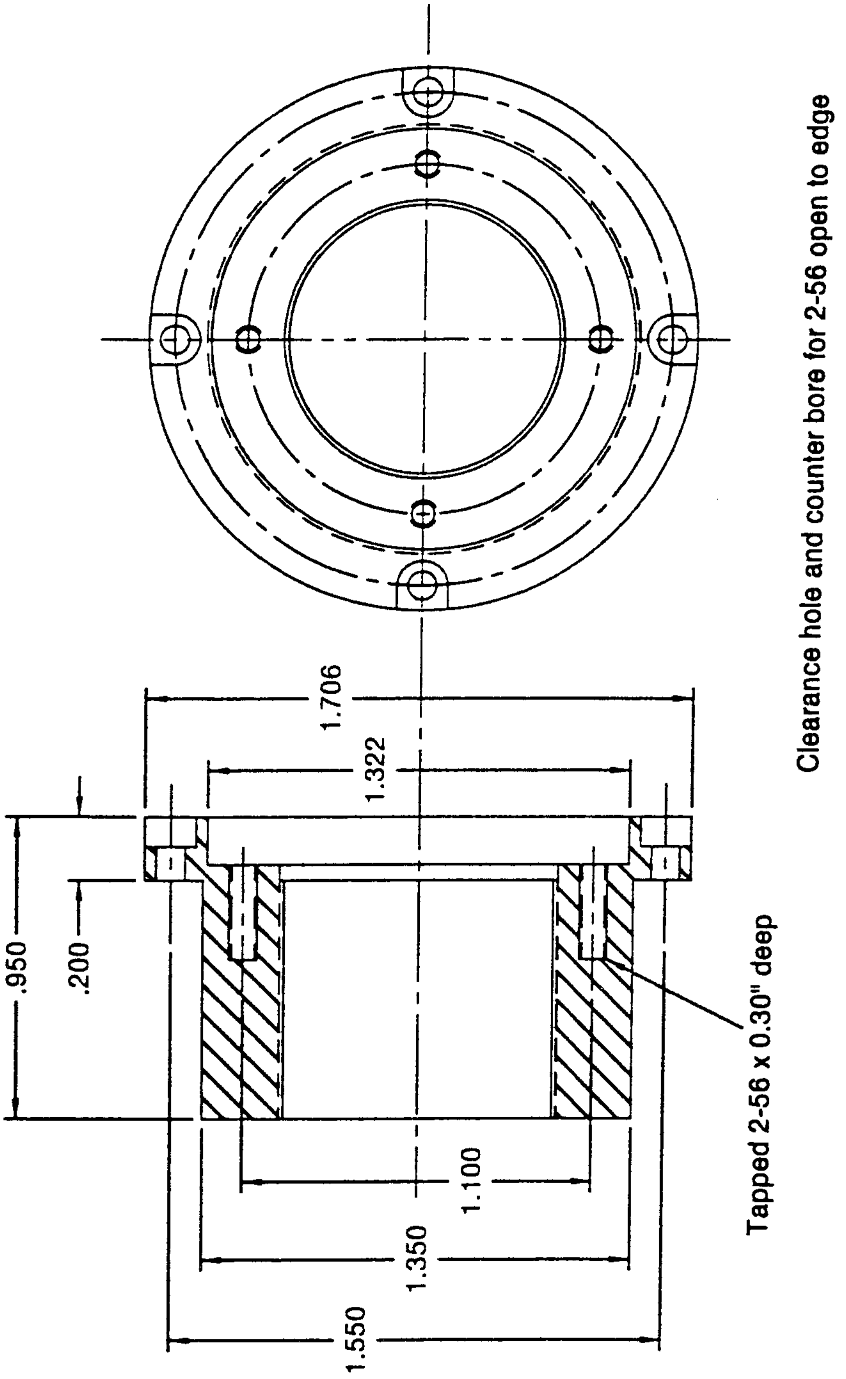

PART NAME RECEIVER: REAR HOUSING		DRAWN BY: Jim Smith Caltech
MATERIAL: AL 6061	DRAWING # 4 of 7	DATE SEP 1996

Figure A.26: Mechanical drawing of receiver rear housing.

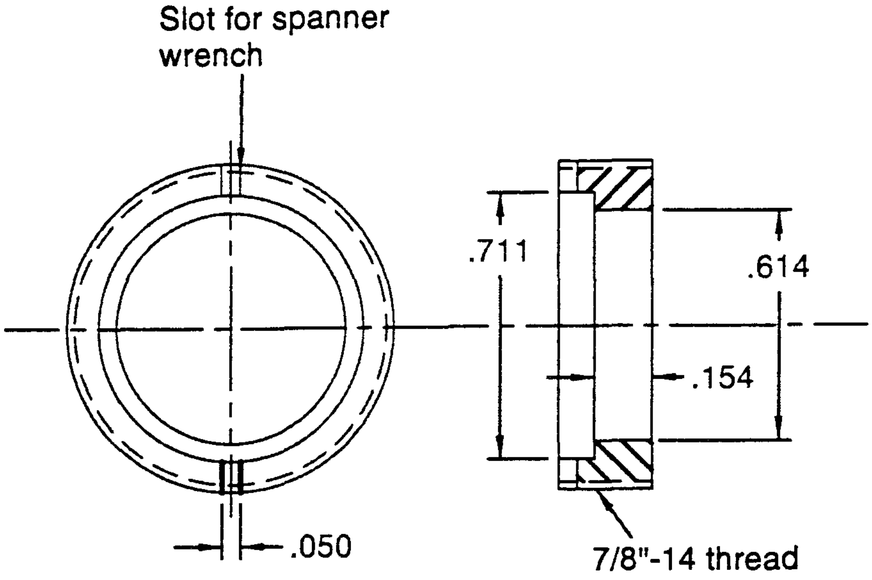

PART NAME RECEIVER: REAR LENS HOLDER		DRAWN BY: Jim Smith Caltech
MATERIAL: AL 6061	DRAWING # 5 of 7	DATE SEP 1996

Figure A.27: Mechanical drawing of receiver rear lens holder.

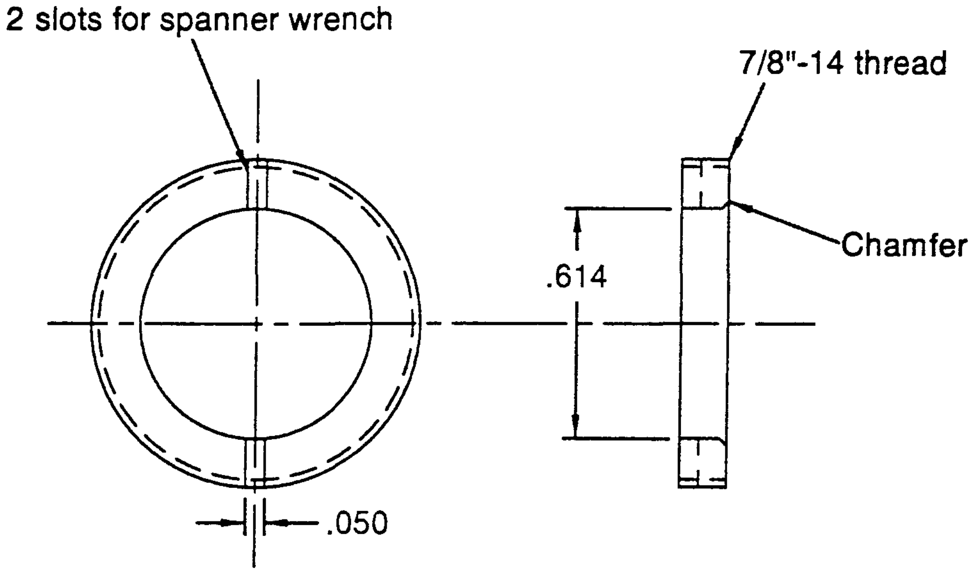

PART NAME RECEIVER: REAR RETAINING RING		DRAWN BY: Jim Smith Caltech
MATERIAL: AL 6061	DRAWING # 6 of 7	DATE SEP 1996

Figure A.28: Mechanical drawing of receiver rear lens retaining ring.

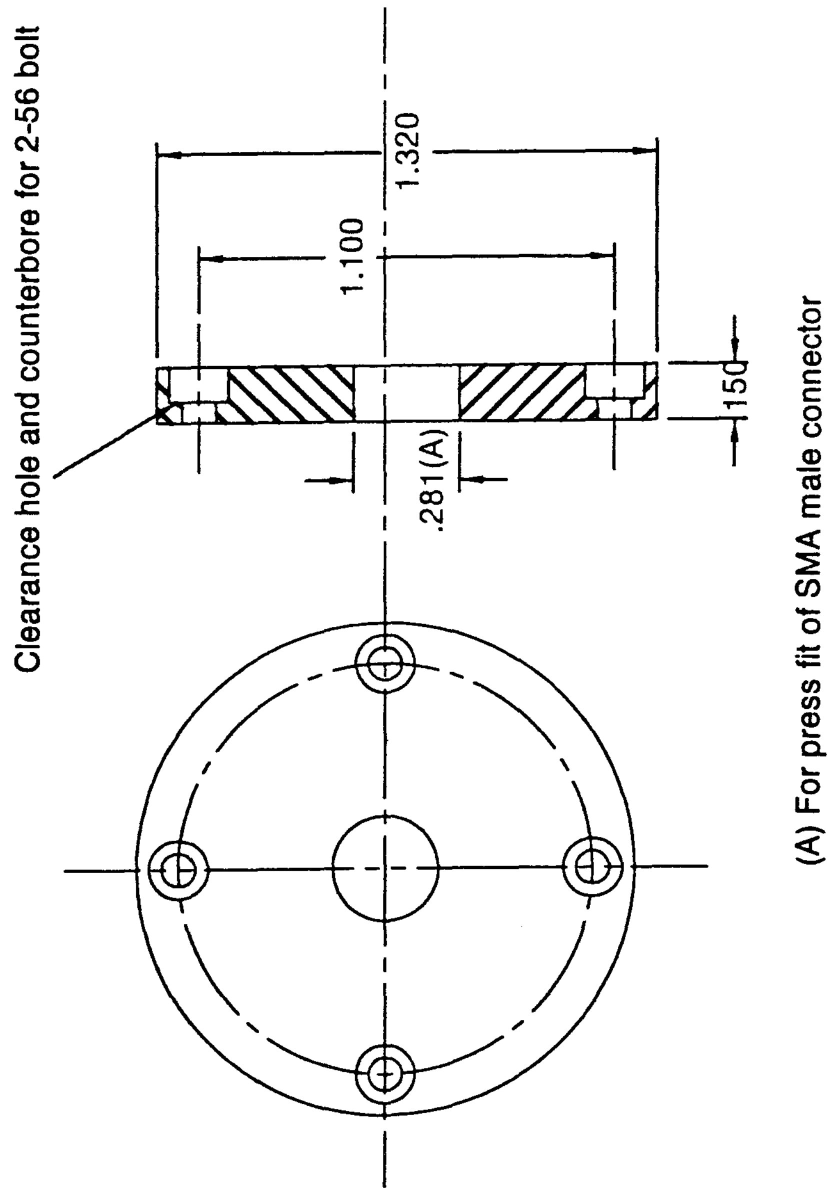

PART NAME RECEIVER: SMA FLANGE		DRAWN BY: Jim Smith Caltech
MATERIAL: AL 6061	DRAWING # 7 of 7	DATE SEP 1996

Figure A.29: Mechanical drawing of receiver SMA flange.

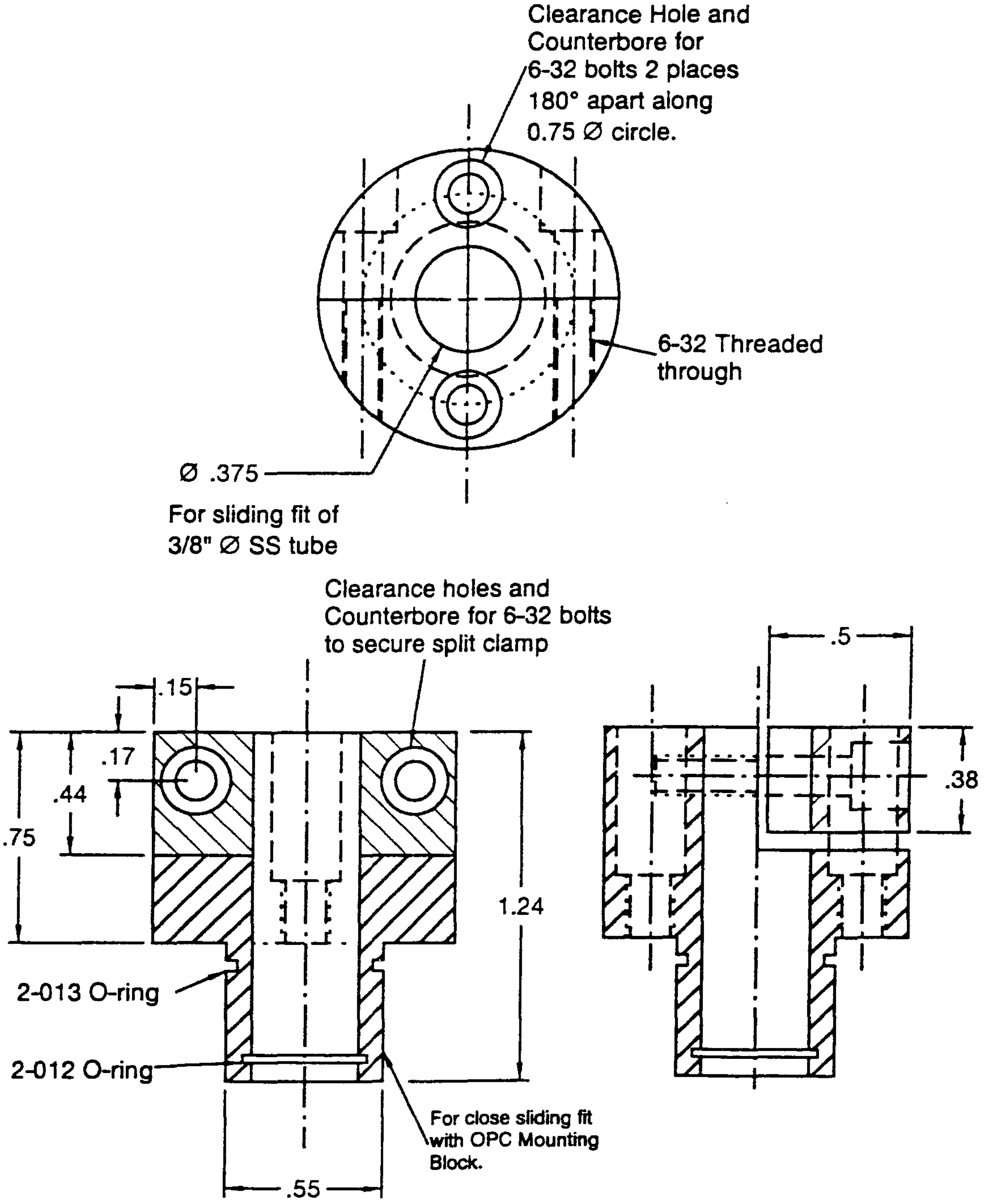

PART NAME BEAM DUMP CLAMP		DRAWN BY: Patrick Chuang and Tim Vanreken
MATERIAL: AL 6061	DRAWING # 1 of 1	DATE 12 02 1998

Figure A.30: Mechanical drawing of OPC beam dump clamp.

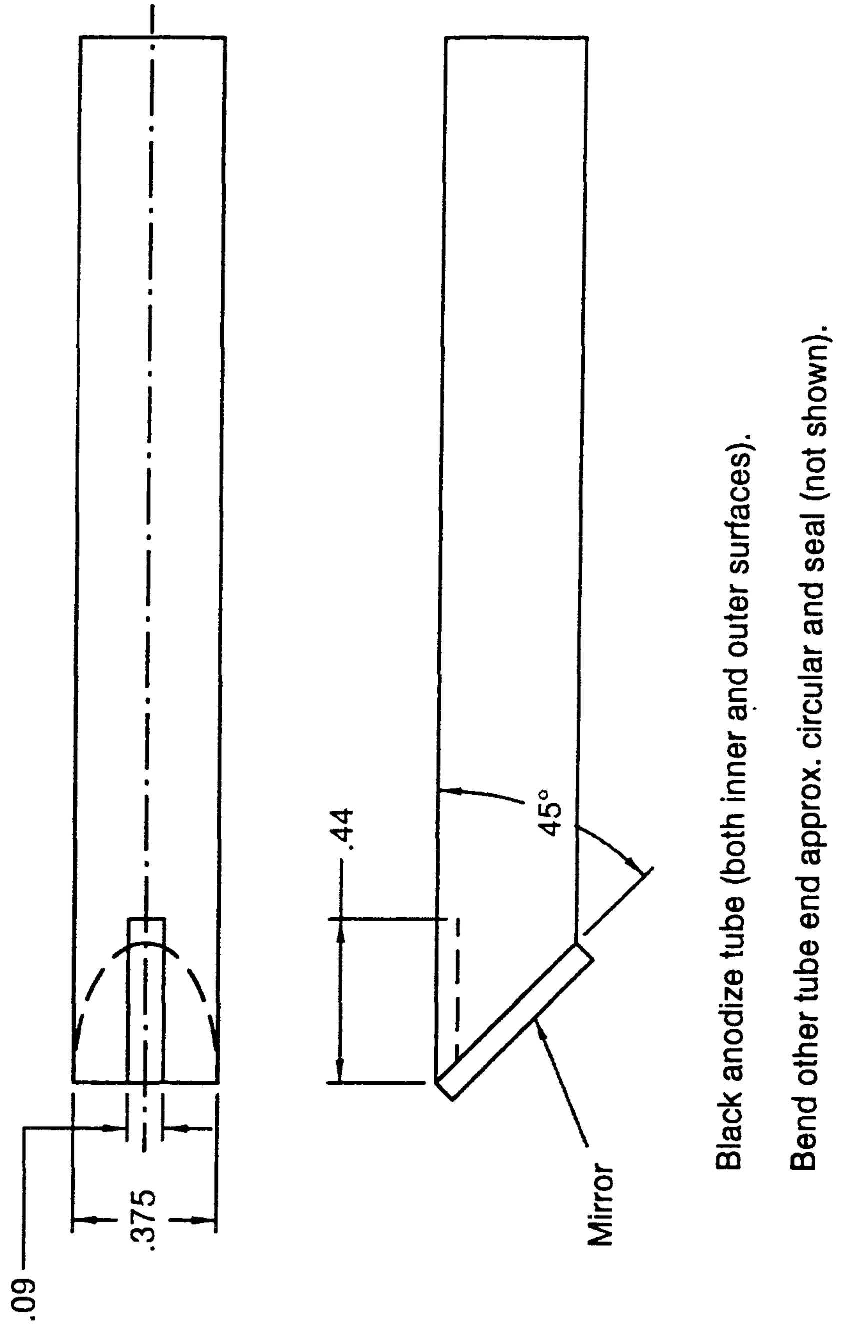

PART NAME BEAM DUMP TUBE MODIFICATION		DRAWN BY: Patrick Chuang Caltech
MATERIAL: AL 6061	DRAWING # 1 of 1	DATE 12 02 1998

Figure A.31: Mechanical drawing of OPC beam dump tubing modification.

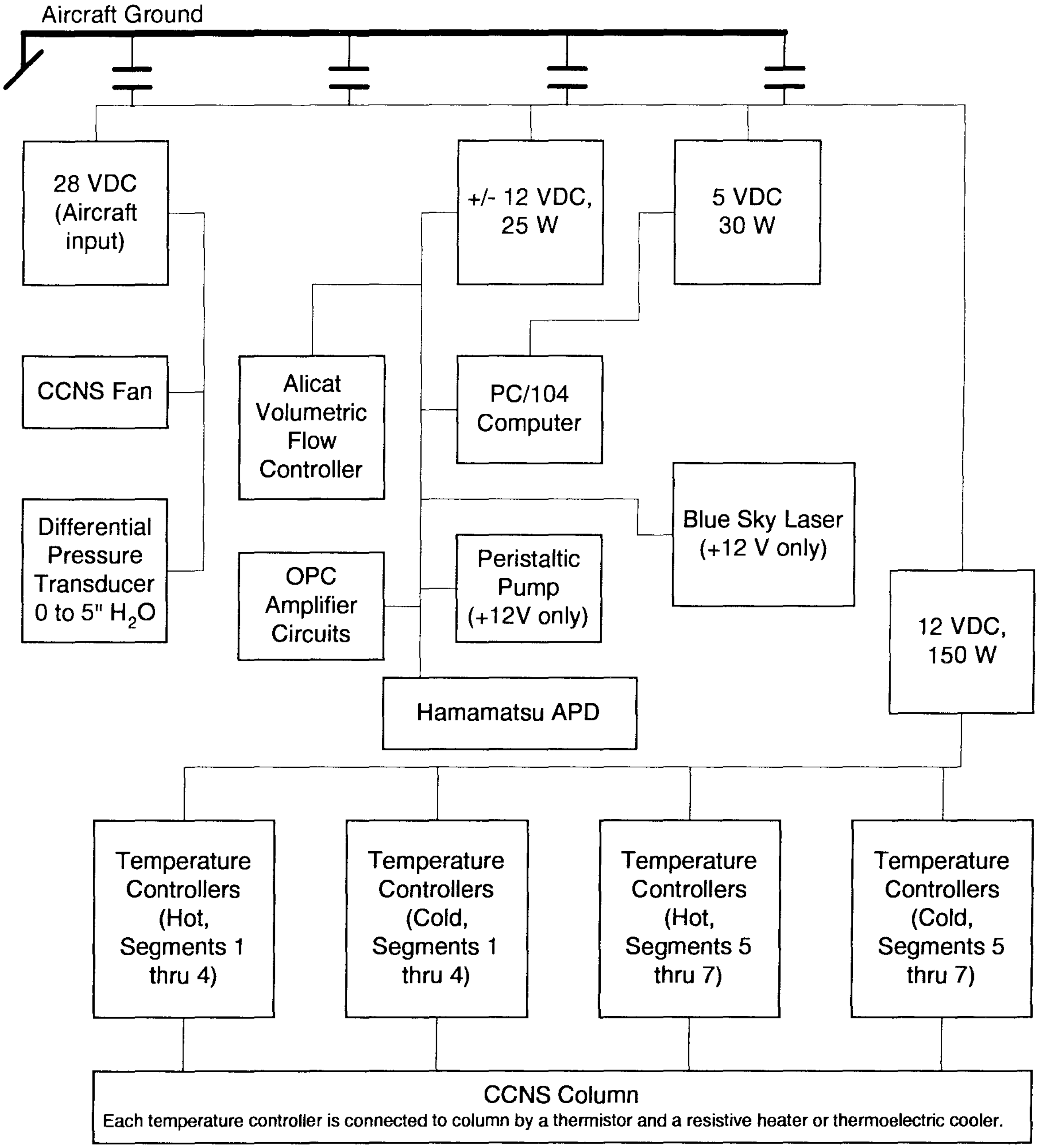

Figure A.32: Wiring diagram of CCN instrument.

Component	Non-Inverting Amp Value	Inverting Amp Value
R_f	1 kΩ	200 Ω
R_g	1 kΩ	1 kΩ
R_{in}	100 kΩ	25 Ω
R_{out}	50 Ω	50 Ω
R_t	N/A	2 kΩ
C1 and C2	0.1 μF ceramic	0.1 μF ceramic
C3 and C4	6.8 μF tantalum	6.8 μF tantalum

Table A.2: Component values for OPC amplifier inverting and non-inverting circuits.

A.4.2 Circuit Diagrams

Figures A.33 and A.34 are the circuit diagrams for the amplifiers used to increase the signal of the output of the Hamamatsu APD. The op-amp in both cases is the CLC426 by National Semiconductor. Note that two amplifiers in series are used in order to provide a high (100 kΩ) input impedance to the amplifier, and to also invert the signal. The first amplifier is used in the non-inverting configuration where the high input impedance can be achieved, followed by the inverting amplifier. Use of the inverting amplifier alone would have resulted in a very low (approx. 1 kohm) input impedance, much too low for the APD circuit to drive.

A.5 Instrument Operation

This section describes operational procedures for testing and running the CCN instrument.

A.5.1 Normal Field Operation

The instrument is designed such that upon turning the power switches on, the instrument begins running automatically. There are currently two power switches, one for only the temperature controllers, and one for all the other electronics. Before turning on the instrument, one must wet the column manually. This is accomplished as follows:

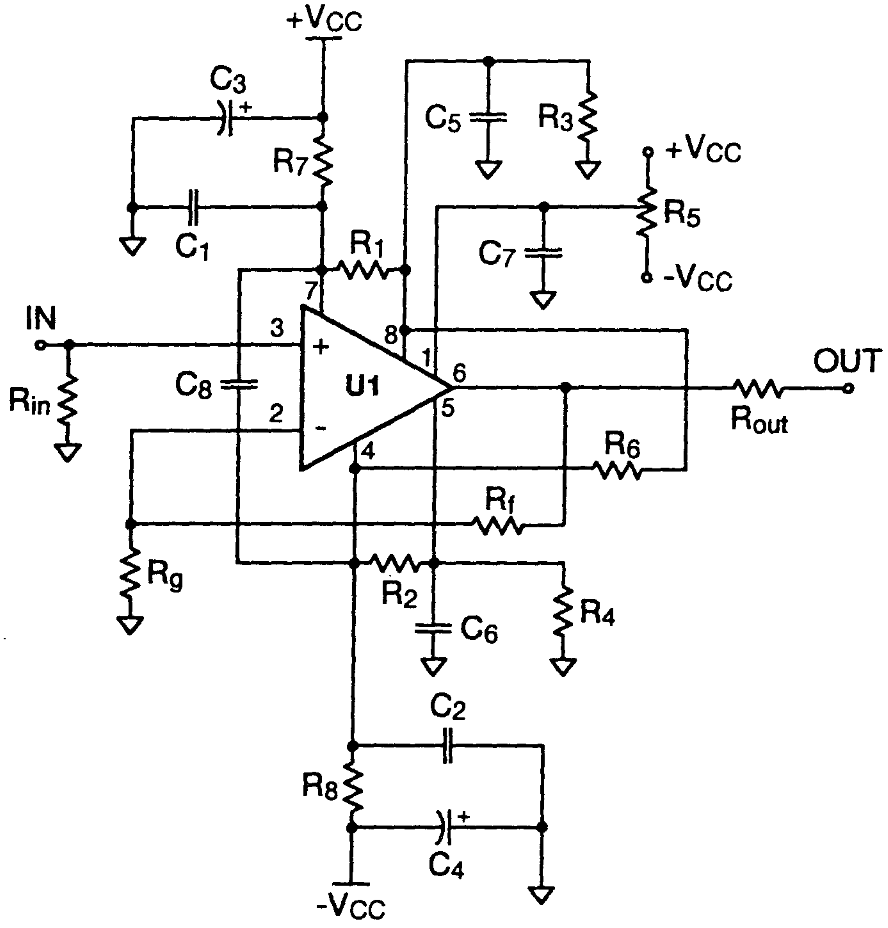

Figure A.33: Non-inverting amplifier circuit diagram.

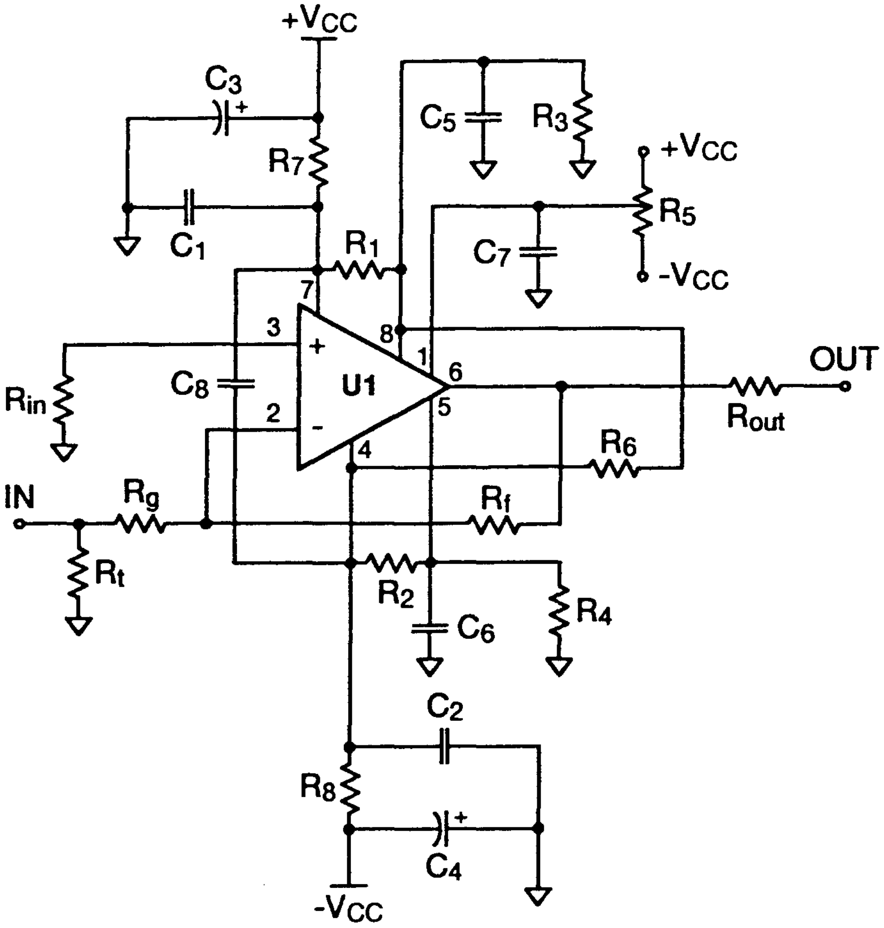

Figure A.34: Inverting amplifier circuit diagram.

1. Remove the inlet top.

2. Plug the nozzle inlet to the OPC using a small (approx. 1/2" diameter) rubber sphere that is attached to a long string. To ensure a good seal, a very thin layer of vacuum grease can be applied to the sphere. This sphere is then dropped down into the column such that it rests on the nozzle inlet, ensuring that no water gets into the nozzle. The string is used to pull the sphere out after the column is wetted.

3. Spray water into the column to completely wet the filter paper using a misting spray bottle that can be purchased from hardware/gardening stores for misting plants. It is recommended that the bottle be modified so that a long tube (Tygon, preferably) connects the bottle with the end that produces the mist. This allows the bottle to be positioned such that if water spills out of the bottle accidentally, it does not harm any instrumentation. It is also more convenient to manipulate the misting end when it is attached to the flexible tubing.

4. Allow any excess water to drain into the outlet flange reservoir. Remove the rubber sphere, inspect the column to make sure that it is wet (and that the filter paper is smoothly adhering to the walls), and replace the inlet top.

A.5.2 Test Procedures

The following are procedures used to test the CCN instrument.

OPC noise test

With no flow in the instrument, turn on the laser and the detection electronics (APD, amplifiers, MCA). If this is the first time that the system is turned on, adjust the Lower Level Detection screw on the MCA card (located on the front panel) until the MCA dead time is at most 5%. The lowest channel that registers counts should be less than channel #100, preferably less than channel #50. If it is too high, try cleaning the receiver lenses (probably the front lens), or perhaps the amplifier gain is too high, in which case the gain should be reduced by using different resistors. Once the MCA is set properly, it shouldn't require subsequent adjustment.

If, at any future times, the dead time with no flow in the instrument is much larger than 5%, it is likely that some water has gotten into the OPC. Remove the receiver and check the front receiver lens. Clean any water droplets or water marks that have accumulated on it. Also inspect the OPC cavity for any other residual water drops. In the case of a large amount of water getting into the system, the beam dump mirror and the transmitter front window may also require cleaning. To clean optical components, first blow off any loosely adhering particles using a can of optical/electronic component air, and then clean with a cotton swab dipped in a small amount of spectrophotometer grade acetone.

OPC and detector check

To check that the OPC, photodetector electronics, and MCA are working properly, turn the instrument on (all electronics, with wetted column). Flow particles (large, monodisperse particles are preferable but not necessary) through the instrument. Hook up an oscilloscope to both the input and output of the amplifier circuit (which correspond to the output of the APD and the input to the MCA). The APD output should negative pulses that are Gaussian in appearance. Each pulse width should be roughly 5 μs. The output of the amplifier circuit should be positive pulses with no baseline offset (because the amplifier circuit is ac-coupled to the APD circuit), and the ratio of the negative to positive pulse heights should correspond to that of the overall amplifier circuit gain. If large (> 100 μm diameter), monodisperse aerosol is used, the MCA should produce a distribution that is well offset from the lower cutoff channel, and has a distribution similar to that of a DMA transfer function. Multiple peaks may be indicative of a problem with the DMA neutralizer. If the Caltech design neutralizer is being used, replace the polonium strips if they are old.

Column temperature check

The column temperatures can be checked two ways. They can be manually checked using the terminal block located near the front of the instrument beside the temperature controllers. The orange wires are the temperature monitors, and the gray wires the corresponding grounds. A multimeter can be used to quickly check if the temperatures are at setpoint. The temperatures can also be checked by running the field software, which logs the temperatures.

Other checks

If mysterious electronic problems occur, the first thing to check is to see if any fuses have blown at the power input. External 28 VDC power runs into the instrument, through the switches, and then through a number of fuses in parallel with a set of resistors designed to buffer any power transients. It's possible that one or more fuses have blown and need to be replaced.

Flowrates should be checked periodically to make sure there are no leaks and that the critical orifice is not partially clogged. Besides using a hand vacuum pump for leak testing, the instrument can be leak tested by running clean filtered air through the instrument, which should naturally not give any counts. Checking that the differential pressure transducer for the aerosol flow is at setpoint is an easy and accurate way to determine if the flows are correct. Another simple test is to use a Gillibrator to measure the total inlet flowrate.

Bibliography

[Alofs, 1978] Alofs, D. J. 1978. Performance of a dual-range cloud nucleus counter. *J. Appl. Meteor.*, 17, 1286–1297.

[Alofs & Carstens, 1976] Alofs, D. J. and Carstens, J. C. 1976. Numerical simulation of a widely used cloud nucleus counter. *J. Appl. Meteor.*, 15, 350–354.

[Berglund & Liu, 1973] Berglund, R. N. and Liu, B. Y. H. 1973. Generation of monodisperse aerosol standards. *Environ. Sci. Technol.*, 7, 147–153.

[Bigg, 1986] Bigg, E. K. 1986. Discrepancy between observation and prediction of concentrations of cloud condensation nuclei. *Atmos. Res.*, 20, 81–86.

[Bluth et al., 1996] Bluth, R. T., Durkee, P. A., Seinfeld, J. H., Flagan, R. C., Russell, L. M., Crowley, P. A., and Finn, P. 1996. Center for Interdisciplinary Remotely-Piloted Aircraft Studies (CIRPAS). *Bull. Am. Meteorol. Soc.*, 77, 2691–2699.

[Bohren & Huffman, 1983] Bohren, C. F. and Huffman, D. R. 1983. *Absorption and Scattering of Light by Small Particles.* Wiley and Sons, 530 pp.

[Brenguier et al., 1998] Brenguier, J. L., Bourrianne, T., Coelho, A. D., Isbert, J., Peytavi, R., Trevarin, D., and Weschler, P. 1998. Improvements of droplet size distribution measurements with the Fast-FSSP (Forward Scattering Spectrometer Probe). *J. Atmos. Ocean Technol.*, 15, 1077–1090.

[Cachier et al., 1986] Cachier, H., Buat-Ménard, P., Fontugne, M., and Chesselet, R. 1986. Long-range transport of continentally-derived particulate carbon in the marine atmosphere: Evidence from stable carbon isotope studies. *Tellus*, 38B, 161–177.

[Charlson et al., 1992] Charlson, R. J., Schwartz, S. E., Hales, J. M., Cess, R. D., Coakley, J. A., Hansen, J. E., and Hofmann, D. J. 1992. Climate forcing by anthropogenic aerosols. *Science*, 255, 423–430.

[Chuang et al., 1997] Chuang, P. Y., Charlson, R. J., and Seinfeld, J. H. 1997. Kinetic limitations on droplet formation in clouds. *Nature*, 390, 594–596.

[Chuang et al., 1999] Chuang, P. Y., Collins, D. R., Pawlowska, H., Snider, J. R., Jonsson, H. H., Brenguier, J.-L., Flagan, R. C., and Seinfeld, J. H. 1999. CCN measurements during ACE-2 and their relationship to cloud microphysical properties. *Tellus (submitted).*

[Clarke et al., 1996] Clarke, A. D., Porter, J. N., Valero, F. P. J., and Pilewskie, P. 1996. Vertical profiles, aerosol microphysics, and optical closure during the Atlantic Stratocumulus Transition Experiment - measured and modeled column optical-properties. *J. Geophys. Res.*, 101, 4443–4453.

[Coakley et al., 1987] Coakley, J. A., Bernstein, R. L., and Durkee, P. A. 1987. Effect of ship-stack effluents on cloud reflectivity. *Science*, 237, 1020–1022.

[Collins et al., 1999] Collins, D. R., Jonsson, H. H., Seinfeld, J. H., Flagan, R. C., Gassó, S., Hegg, D. A., Russell, P. B., Schmid, B., Livingston, J. M., Öström, E., Noone, K. J., Russell, L. M., and Putaud, J. 1999. In-situ aerosol size distributions and CLEARCOLUMN radiative closure during ACE-2. *Tellus (submitted).*

[Covert et al., 1998] Covert, D. S., Gras, J. L., Wiedensohler, A., and Stratmann, F. 1998. Comparison of directly measured CCN with CCN modeled from the number-size distribution in the marine boundary layer during ACE 1 at Cape Grim, Tasmania. *J. Geophys. Res.*, 103, 16597–16608.

[Delene et al., 1998] Delene, D. J., Deshler, T., Wechsler, P., and Vali, G. A. 1998. A balloon-borne cloud condensation nuclei counter. *J. Geophys. Res.*, 103, 8927–8934.

[Dingenen, 1999] Dingenen, R. V. 1999. Local closure during ACE-2: Chemical composition and size distributions of marine boundary layer aerosol at Punta del Hidalgo, Tenerife. *Tellus (submitted).*

[Fukuta & Saxena, 1979] Fukuta, N. and Saxena, V. K. 1979. A horizontal thermal gradient cloud condensation nucleus spectrometer. *J. Appl. Meteor.*, 18, 1352–1362.

[Ghan et al., 1999] Ghan, S., Abdul-Razzak, H., Nenes, A., Chuang, P. Y., and Seinfeld, J. H. 1999. Kinetic limitations on droplet formation. *J. Geophys. Res. (submitted).*

[Gosman & Ideriah, 1976] Gosman, A. D. and Ideriah, A. 1976. *TEACH-2E.* Technical Report FM-83-2, Univ. California Berkeley.

[Hegg et al., 1993] Hegg, D. A., Ferek, R. J., and Hobbs, P. V. 1993. Light-scattering and cloud condensation nucleus activity of sulfate aerosol measured over the northeast atlantic-ocean. *J. Geophys. Res.*, 98, 14887–14894.

[Hegg et al., 1996] Hegg, D. A., Hobbs, P. V., Gassó, S., Nance, J. D., and Rangno, A. L. 1996. Aerosol measurements in the Arctic relevant to direct and indirect radiative forcing. *J. Geophys. Res.*, 101, 23349–23363.

[Hegg et al., 1991] Hegg, D. A., Radke, L. F., and Hobbs, P. V. 1991. Measurements of Aitken nuclei and cloud condensation nuclei in the marine atmosphere and their relation to the DMS-cloud-climate hypothesis. *J. Geophys. Res.*, 96, 18727–18733.

[Hindmarsh, 1963] Hindmarsh, A. C. 1963. *ODEPACK: A Systemized Collection of ODE Solvers.* North-Holland, 00 pp.

[Hoppel et al., 1979] Hoppel, W. A., Twomey, S., and Wojciechowski, T. A. 1979. A segmented thermal diffusion chamber for continuous measurements of CN. *J. Aerosol Sci.*, 10, 369–373.

[Hudson, 1989] Hudson, J. G. 1989. An instantaneous CCN spectrometer. *J. Atmos. Ocean Technol.*, 6, 1055–1065.

[Hudson & Clarke, 1992] Hudson, J. G. and Clarke, A. D. 1992. Aerosol and cloud condensation nuclei measurements in the kuwait plume. *J. Geophys. Res.*, 97, 14533–14536.

[Hudson & Squires, 1976] Hudson, J. G. and Squires, P. 1976. An improved continuous flow diffusion cloud chamber. *J. Appl. Meteor.*, 15, 776–782.

[Hudson & Svensson, 1995] Hudson, J. G. and Svensson, G. 1995. Cloud microphysical relationships in California marine stratus. *J. Appl. Meteorol.*, 34, 2655–2666.

[Hudson et al., 1998] Hudson, J. G., Xie, Y., and Yum, S. S. 1998. Vertical distributions of cloud condensation nuclei spectra over the summertime Southern Ocean. *J. Geophys. Res.*, 103, 16609–16624.

[IPCC, 1996] IPCC 1996. *Climate Change 1995: The Science of Climate Change.* Cambridge University Press, 572 pp.

[Kandlikar & Ramachandran, 1999] Kandlikar, M. and Ramachandran, G. 1999. Inverse methods for analysing aerosol spectrometer measurements: A critical review. *J. Aerosol Sci.*, 30, 413–437.

[Laaksonen et al., 1998] Laaksonen, A., Korhonen, P., Kulmala, M., and Charlson, R. J. 1998. Modification of the Köhler equation to include soluble trace gases and silghtly soluble substances. *J. Atmos. Sci.*, 55, 853–862.

[Laktionov, 1972] Laktionov, A. G. 1972. A constant-temperature method of determining the concentrations of cloud condensation nuclei. *Atmos. and Oceanic Phys.*, 8, 672–677.

[Lala & Jiusto, 1977] Lala, G. G. and Jiusto, J. E. 1977. An automatic light scattering CCN counter. *J. Appl. Meteor.*, 16, 413–418.

[Leaitch & Megaw, 1982] Leaitch, R. and Megaw, W. J. 1982. The diffusion tube: a cloud condensation nucleus counter for use below 0.3*J. Aerosol Sci.*, 13, 297–319.

[Liu et al., 1996] Liu, P. S. K., Leaitch, W. R., Banic, C. M., Li, S. M., Ngo, D., and Megaw, W. J. 1996. Aerosol observations at Chebogue Point during the 1993 North Atlantic Regional Experiment: Relationships among cloud condensation nuclei, size distribution, and chemistry. *J. Geophys. Res.*, 101, 28971–28990.

[Martin et al., 1994] Martin, G. M., Johnson, D. W., and Spice, A. 1994. The measurement and parameterization of effective radius of droplets in warm stratocumulus clouds. *J. Atmos. Sci.*, 51, 1823–1842.

[McFarlane et al., 1992] McFarlane, N. A., Boer, G. J., Blanchet, J.-P., and Lazare, M. 1992. The Canadian Climate Centre second-generation general circulation model and its equilibrium climate. *J. Climate*, 5, 1013–1044.

[Moeng & Curry, 1990] Moeng, C.-H. and Curry, J. 1990. The sensitivity of large eddy simulations of a stratus topped boundary layer to cloud microphysics. In *Proc. Conf. on Cloud Physics* (pp. 115–121).: San Francisco, Amer. Meteor. Soc.

[Novakov & Penner, 1993] Novakov, T. and Penner, J. E. 1993. Large contribution of organic aerosols to cloud-condensation-nuclei concentrations. *Nature*, 365, 823–826.

[O'Dowd et al., 1997] O'Dowd, C. D., Smith, M. H., Consterdine, I. E., and Lowe, J. A. 1997. Marine aerosol, sea-salt and the marine sulphur cycle: A short review. *Atmos. Env.*, 31, 73–80.

[Patankar, 1980] Patankar, S. V. 1980. *Numerical Heat Transfer and Fluid Flow.* McGraw-Hill, 197 pp.

[Pruppacher & Klett, 1997] Pruppacher, H. R. and Klett, J. D. 1997. *Microphysics of Clouds and Precipitation.* Reidel.

[Pueschel et al., 1986] Pueschel, R. F., Vanvalin, C. C., Castillo, R. C., Kadlecek, J. A., and Ganor, E. 1986. Aerosols in polluted versus nonpolluted air masses - long-range transport and effects on clouds. *J. Clim. Appl. Meteorol.*, 25, 1908–1917.

[Radke & Turner, 1972] Radke, L. F. and Turner, F. M. 1972. An improved automatic cloud condensation nucleus counter. *J. Appl. Meteor.*, 11, 407–409.

[Raes et al., 1999] Raes, F., Bates, T., Verver, G., Vogelenzang, D., and Liedekerke, M. V. 1999. The Second Aerosol Characterization Experiment ACE-2: Introduction, meteorological overview and main results. *Tellus (submitted).*

[Raga & Jonas, 1993] Raga, G. B. and Jonas, P. R. 1993. On the link between cloud-top radiative properties and sub-cloud aerosol concentrations. *Q. J. R. Meteorol. Soc.*, 119, 1419–1425.

[Raga & Jonas, 1995] Raga, G. B. and Jonas, P. R. 1995. Vertical distribution of aerosol particles and CCN in clear air around the British Isles. *Atmos. Env.*, 29, 673–684.

[Riveracarpio et al., 1996] Riveracarpio, C. A., Corrigan, C. E., Novakov, T., Penner, J. E., Rogers, C. F., and Chow, J. C. 1996. Derivation of contributions of sulfate and carbonaceous aerosols to cloud condensation nuclei from mass size distributions. *J. Geophys. Res.*, 101, 19483–19493.

[Russell et al., 1996] Russell, L. M., Zhang, S. H., Flagan, R. C., Seinfeld, J. H., Stolzenburg, M. R., and Caldow, R. 1996. Radially classified aerosol detector for aircraft-based submicron aerosol measurements. *J. Atmos. Ocean Technol.*, 13, 598–609.

[Seinfeld & Pandis, 1998] Seinfeld, J. H. and Pandis, S. N. 1998. *Atmospheric Chemistry and Physics: From Air Pollution to Climate Change.* Wiley and Sons, 1326 pp.

[Shulman et al., 1996] Shulman, M. L., Jacobson, M. C., Charlson, R. J., Synovec, R. E., and Young, T. E. 1996. Dissolution behavior and surface tension effects of organic compounds in nucleating cloud droplets. *Geophys. Res. Lett.*, 23, 277–280.

[Sinnarwalla & Alofs, 1973] Sinnarwalla, A. M. and Alofs, D. J. 1973. A cloud nucleus counter with long available growth time. *J. Appl. Meteor.*, 12, 831–835.

[Slingo & Schwartz, 1996] Slingo, A. and Schwartz, S. E. 1996. Enhanced shortwave cloud radiative forcing due to anthropogenic aerosols. In P. J. Crutzen & V. Ramanathan (Eds.), *Clouds, Chemistry and Climate* (pp. 191–236). Springer-Verlag.

[Stumm & Morgan, 1981] Stumm, W. and Morgan, J. J. 1981. *Aquatic Chemistry.* John Wiley and Sons, Inc.

[Twomey, 1963] Twomey, S. 1963. Measurements of natural cloud nuclei. *J. Rech. Atmos.*, 1, 101–105.

[Vong & Covert, 1998] Vong, R. J. and Covert, D. S. 1998. Simultaneous observations of aerosol and cloud droplet size spectra in marine stratocumulus. *J. Atmos. Sci.*, 55, 2180–2192.

[Yum et al., 1998] Yum, S. S., Hudson, J. G., and Xie, Y. H. 1998. Comparisons of cloud microphysics with cloud condensation nuclei spectra over the summertime Southern Ocean. *J. Geophys. Res.*, 103, 16625–16636.

[Zhang et al., 1995] Zhang, S. H., Akutsu, Y., Russell, L. M., Flagan, R. C., and Seinfeld, J. H. 1995. Radial differential mobility analyzer. *Aerosol Sci. Technol.*, 23, 357–372.